Title

IMAGING STRUCTURE AND IMPURITIES IN THE CORE OF SILICON DISLOCATIONS AND GRAIN BOUNDARIES: A HIGH-RESOLUTION TRANSMISSION ELECTRON MICROSCOPY AND COMPUTER IMAGE SIMULATION STUDY

Author

Rose, J.H.

Publication Date

1985-09-01

Lawrence Berkeley Laboratory
UNIVERSITY OF CALIFORNIA

Materials & Molecular Research Division

IMAGING STRUCTURE AND IMPURITIES IN THE CORE OF SILICON DISLOCATIONS AND GRAIN BOUNDARIES: A HIGH-RESOLUTION TRANSMISSION ELECTRON MICROSCOPY AND COMPUTER IMAGE SIMULATION STUDY

J.H. Rose
(Ph.D. Thesis)

September 1985

Prepared for the U.S. Department of Energy under Contract DE-AC03-76SF00098

DISCLAIMER

Imaging Structure and Impurities in the Core of Silicon Dislocations and Grain Boundaries: A High-Resolution Transmission Electron Microscopy and Computer Image Simulation Study

Jamie H. Rose

Ph.D. Thesis
September 1985

Materials and Molecular Research Division
Lawrence Berkeley Laboratory

and

Department of Materials Science and Mineral Engineering
University of California

Berkeley, California 94720

table of contents

The finest qualities of our nature, like the bloom on fruits, can be preserved only by the most delicate handling. Yet we do not treat ourselves nor one another thus tenderly.

Henry David Thoreau

"When you wake up in the morning, Pooh," said Piglet at last,"what's the first thing you say to yourself?"

"What's for breakfast?" said Pooh. "What do *you* say, Piglet?"

"I say, I wonder what's going to happen exciting *to-day*?" said Piglet.

Pooh nodded thoughtfully.

"It's the same thing," he said.

A. A. Milne

Acknowledgements

In expressing thanks, it is impossible to avoid the cliches employed countless times before. Please know that you're all truely appreciated.

Ron Gronsky, my research advisor, has been endlessly encouraging and enthusiastic. Professors Jeffery Reimer and Eugene Haller reviewed the thesis. Dr. Haller was also helpful a number of times beyond the call of duty.

The image simulation work would have been impossible without the computer programs provided by Roar Kilaas, not to mention the many conversations on their application and image interpretation. Mike O'Keefe helped to clarify some of the mysteries of the inner workings of these programs, while providing the latest version of his image simulation programs in the latter stages of the thesis.

Eduardo Kamenetzky taught me a lot about grain boundaries.

Roseann Csencsits taught me a little about chemistry.

Thanks Mike, Roseann, Ed, Roar and Char, for the important things in life.

Eileen, some day you'll realize how good you are.

This work was supported by the Director, Office of Energy Research, Office of Basic Energy Sciences, Materials Science Division of the United States Department of Energy under Contract No. DE-AC03-76SF00098.

Thank you, taxpayers, for keeping me off the streets.

Abstract

The core structure of silicon grain boundaries has been studied with high-resolution transmission electron microscopy (HRTEM). The atomistic nature of segregation sites in the diamond structure and potential HRTEM methods for their study have been evaluated.

Insight into these defects is important in light of applications of polycrystalline silicon in integrated circuits. More generally, as device dimensions decrease, interfacial phenomena grow ever more important. In addition, knowledge gained from semiconductor studies may shed light on general grain boundary phenomena.

Specifically, plastic models with "bond" lengths selected to mimic the covalent bonds in silicon were constructed for silicon dislocations lying along <110> and <100> directions and <110> and <100> tilt grain boundaries. These models then assisted in prediction of potential defect core interstitial and substitutional segregation sites. Computer simulation of HRTEM images was applied to these models to assess the potential of HRTEM for imaging impurities at defects. In addition, HRTEM has been applied to the structural analysis of <110> and <100> tilt grain boundaries in silicon.

The dislocations and grain boundaries examined can be described in terms of a small set of basic structural elements. These include perfect diamond structure 6-membered rings, boat-shaped rings, 5- and 7-membered rings, and elements possessing unpaired or reconstructed valence electrons. In addition, silicon grain boundaries seem well suited to a structural unit description based on dislocation cores plus units unique

to grain boundaries.

It is proposed that donor atoms segregate to defect cores where geometry and the existence of potentially unpaired valence electrons allow formation of five bonds. Such a site probably exists in the 30° partial dislocation core. Interstitial impurities can reside in the large tunnels found in dislocations and grain boundaries. These tunnel sites are associated with the presence of 7-membered rings.

From image simulation calculations, diffuse imaging is found to hold substantial promise for detection of impurities. Impurity atoms of Z greater than silicon have diffuse images analogous to those of isolated atoms while species of lower Z give inverted intensity features. Optimum impurity contrast with sufficient intensity for feasible exposure times is found for thicknesses in the neighborhood of the extinction distance (200Å to 400Å for <110> oriented silicon.) For arsenic and boron in silicon, the detection limit is approximately 2 or 3 atoms lying parallel to the beam direction (out of a column of ~75 potential core segregation sites) while a single antimony atom is, in principle, observable. In lattice images, these impurities yield about half as much contrast, requiring twice the line concentration for detection. Since defect strain fields were found to produce contrast at a comparable level to segregated impurities, deconvolution of impurity contrast from defect strain field contrast in experimental images will require careful matching with simulated images.

From observations of HRTEM experimental images, a silicon Σ9 grain boundary was found to have a Coincidence Site Lattice fundamental translation state of $\frac{a}{4}$<111> plus a small dilation of .4±.2Å. It has a zigzagging Lomer dislocation core structure with an as yet unexplained asymmetry in the alternating units. No rigid body translation was detected for the the Σ13 grain boundary. It appears to contain

two 45° dislocations plus a stabilizing 45° dislocation dipole, per period. These conclusions were supported by concurrent simulated image matching.

CHAPTER 1

Introduction

The following text describes a study of the atomic structure and segregation behavior of some silicon grain boundaries and dislocations. Grain boundary and dislocation atomic models are evaluated and segregation models proposed. With this background, emphasis is then placed on a computer image simulation based analysis of the potential of high-resolution transmission electron microscopy (HRTEM) for imaging impurities in these defects. Lastly, HRTEM is applied to the core structure analysis of <110> and <100> tilt boundaries in silicon. The focus is on distinguishing between distinctly different defect models as opposed to determining the exact spatial coordinates of the atoms.

Interest in this subject was stimulated by the author's previous work on phosphorus segregation at grain boundaries in thin-film silicon as observed by X-ray spectroscopy in a scanning transmission electron microscope.[1] Phosphorus was observed to segregate at various levels in a given specimen suggesting a correlation with grain boundary structure. However, only qualitative conclusions were possible due to detection limits of the technique and the difficulty in analyzing grain boundaries in the fine-grained material studied. High-resolution TEM was chosen for continuing studies in the hope it would clarify the structural features of grain boundaries, yielding insight into the nature of segregation sites at these defects. The potential of this technique for new findings was particularly enhanced by the recent aquisition of the "Atomic Resolution Microscope" (JEOL ARM-1000) at the Lawrence Berkeley Laboratory with

a point to point resolution of about 1.6Å when operating at 1000 KeV.

With HRTEM, one obtains information about projections of the crystal structure, essentially limiting study to samples aligned along low index poles and defects which are uniform in this direction. This allows observation of straight dislocations and end-on tilt grain boundaries. However, these particular defects provide much insight into the structure and properties of general dislocations and grain boundaries in silicon and other semiconductors.

High-resolution TEM also holds some promise for distinguishing atoms of different chemical species, particularly in the case of large differences in atomic number (and hence scattering factors). Given the periodicity along the beam of defects studied via HRTEM, segregation sites characteristic of the defect core (*not* the continuum type strain field) will reflect this periodicity. If suitable heat treatments can fill these sites with impurities of relatively high or low Z, one might then expect to detect the presence of an impurity column with HRTEM. Computer image simulations are applied in the analysis of the feasibility of using HRTEM for the particular problem of dopant and metallic impurity segregation at dislocations and grain boundaries.

In the final chapter, HRTEM is applied to the analysis of core structure in the $\Sigma 9$ <110> tilt and $\Sigma 13$ <100> tilt grain boundaries. The ARM provides the required resolution for the latter boundary.

CHAPTER 2

Dislocation Structure

The theoretical basis for the description of dislocations in a continuous medium was developed in 1907, years before their discovery[2]. This theory works well for dislocations in real, crystalline materials so long as the strains are small. Thus, the theory breaks down as the dislocation line is approached and is particularly poor in the core. Atomic calculations have attempted to evaluate the core configuration.[3] However, these calculations are not theoretically fundamental and are limited by required assumptions and the approximate atomic potentials employed in the calculations. For this reason, any information concerning core atomic configuration obtained by HRTEM is valuable.

Research on semiconductor dislocations over the past three decades has usually been concerned, at least partially, with electrical properties. Though perhaps not apparent, the present research has indirect application here. Solid state physicists have developed means of calculating the electronic structure of semiconductor dislocations and grain boundaries.[4],[5],[6] These theories require atomic spatial coordinates as input. Results of this research will hopefully support these endeavors and lead to better understanding of experimentally measured electronic properties.

2.1. Perfect Dislocation Structure

First insight into the nature of dislocations (and grain boundaries) in silicon arises from a consideration of the diamond crystal structure. This structure consists

of two interpenetrating FCC lattices displaced by $\frac{1}{4}$ the cube diagonal, i.e. it is FCC with a two atom basis. The other prominent feature is its covalent, tetrahedral bonding. Intuitively, the structure may be viewed as silicon atoms joined by "rods" (covalent bonds) to their four nearest neighbors (fig. 2-1a). In the following, attention will be particularly given to the (100) and (110) projections.

In 1958, employing such geometrical notions, Hornstra discussed most of the essential features of silicon and germanium dislocations.[7] As for other FCC materials, perfect dislocations exhibit a Burgers vector of $\frac{a}{2}<110>$ (a $<100>$ Burgers vector is marginally stable.) Also they are simplest in form when lying along $<110>$ directions. There are three of these; the screw, the 60° (Burgers vector at 60° to the dislocation line), and the Lomer dislocation, an edge dislocation with {100} glide plane. All other perfect dislocations may be considered as consisting of steps of these dislocations. The screw and the 60° are of particular interest since they dominate during plastic deformation. In addition, two possible dislocations along $<100>$ are especially significant due to their possible role in grain boundary structure; a pure edge dislocation and a 45° dislocation (see Sec. 2.2). The dislocations mentioned above are listed in Table 2-1.

There are a few additional straight dislocations in silicon, these along $<112>$, which correspond to jogs or kinks.

In diamond there exists an added complication over simple FCC materials due to the two atom basis. In fig. 2-1b, a {110} projection of the diamond structure is depicted with {111} planes normal to the page labeled according to their stacking sequence. While an FCC lattice has the stacking sequence:

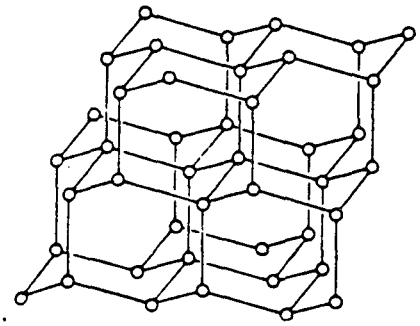

a

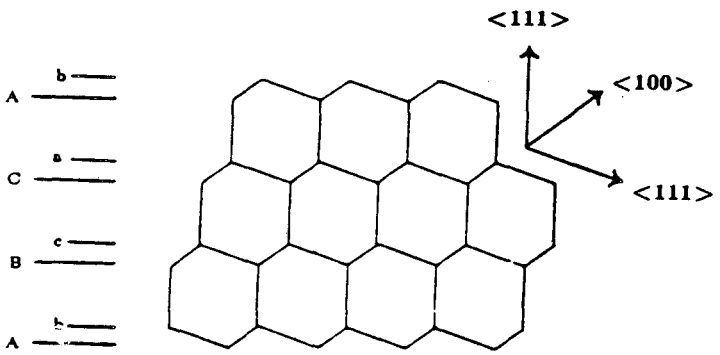

b

Diamond Structure

Fig. 2-1 (**a**) Perfect crystal diamond structure viewed at angle to <110>. (**b**) Projection of diamond structure on {110}. Letters indicate pairs of planes in FCC <111> stacking. Upper case denotes planes from one FCC lattice, lower case from the other. These two perspectives are the basis for the following depictions of defects lying along the <110> direction. XBL 855-2558

a/2 <110> Dislocations		
Type	Line Direction	Glide Plane
Screw (0°)	<110>	{111}
60°	<110>	{111}
Lomer (90°)	<110>	{100}
---	---	---
45°	<100>	{100}
Edge (90°)	<100>	{110}

Table 2-1: The fundamental, perfect Burgers vectors of the FCC lattice.

.....A B C A B C A B C.....

in diamond it is:

.....A a B b C c A a B b C c A a B b C c.....

In other words, there are *pairs* of planes derived from the two FCC lattices which have been displaced along <111>. The extra half-plane of a dislocation may, in principle, end on either of these plane types (A or a) giving dislocation cores of distinctly different structure. These two general dislocation types have been labeled the *glide* set and the *shuffle* set by Hirth and Lothe.[8] Glide set dislocations glide on narrowly spaced planes while the shuffle set glide on the widely spaced planes. Historically, glide was assumed to occur on widely spaced planes since this requires breaking of one bond per atom rather than three for glide dislocations. Thus, Hornstra only considered shuffle dislocations. However, experimental observations during the past ten years indicate that dislocations are generally of the glide set (Sec.2.2). The intent in

the remainder of this section is to demonstrate the geometrically possible core structures of the dislocations of interest.

Model core structures are developed by performing the required displacement on the perfect crystal structure, then reforming bonds in an attempt to avoid "broken" bonds by allowing small atomic displacements and bond bending. Bond bending and length changes induce an increase in energy so that at some angle unpaired electrons are favored. As a guide, one notes that amorphous semiconductors have bond angles distorted by up to $\sim$15% and bond lengths which vary by $\sim$1%.[9]

For this thesis, models were fabricated from plastic tubing and metallic joints such as those found in molecular model kits employed in organic chemistry instruction. The tubing was cut to 2.25 inches, approximating the allowed bending discussed above. Though these models yield only qualitative notions about structure and properties, they remain a powerful tool to outline reasonable possibilities which may then be tested via experiment.

Perspective views of the **60° glide and shuffle dislocations** are found in fig. 2-2 (top). Note that though the two models have distinctly different atomic core configurations - distinguished by the presence or absence of a column of silicon atoms - their continuum theory based strain fields are identical. For this reason, conventional transmission electron microscopical techniques, which rely on strain field contrast, are expected to give identical images for different core structures.

Atoms along the edge of the dislocation half-plane have broken bonds (geometrically speaking) or what is often referred to in the literature as "dangling bonds" after Shockley's original description in 1953.[10] The exact nature of these unpaired electrons

60 ° Dislocation

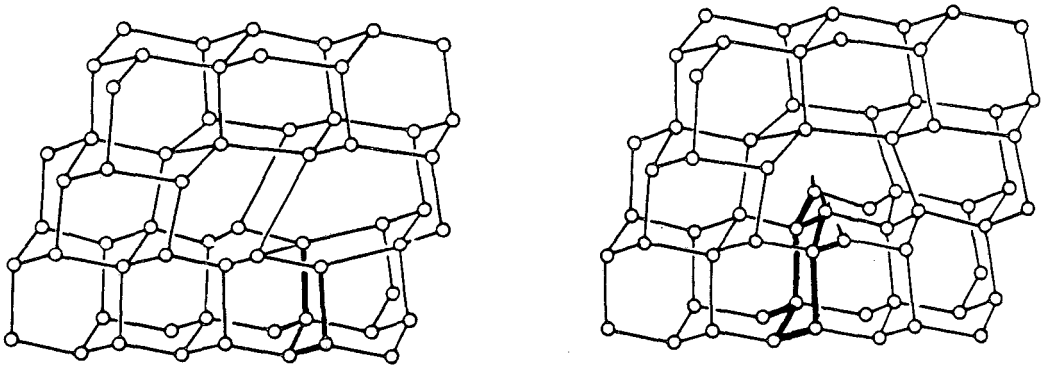

Glide Shuffle

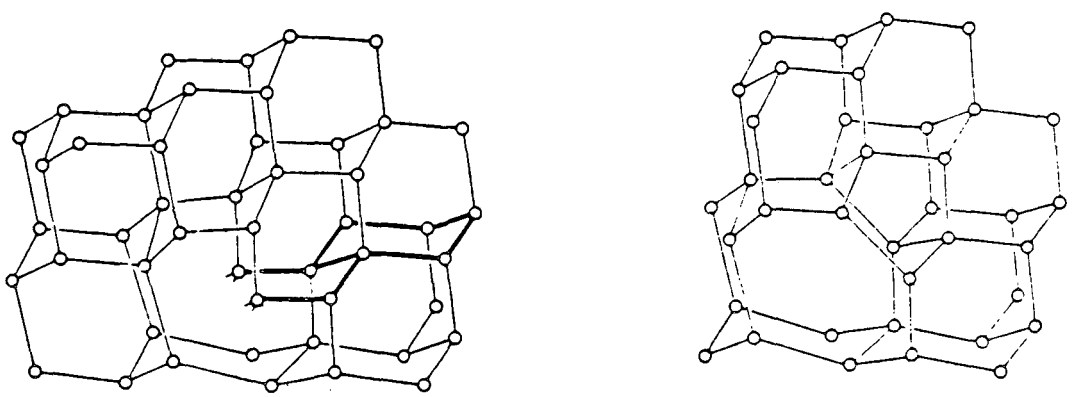

Lomer

Fig. 2-2 The top figures give the two possible forms of the 60° mixed dislocation (after Hirth and Lothe[8]). The extra half-plane is indicated with bold lines. In the glide configuration, the half-plane ends between narrowly spaced planes while in the shuffle configuration, it ends between widely spaced planes. The pure edge Lomer dislocation also has glide and shuffle forms (below, after Hornstra[7]). In its shuffle configuration, it can be depicted without unpaired electrons. XBL 855-2559

and possible reconstruction is currently of great interest. However, HRTEM is presently limited to investigating the location of the atomic nucleus rather than outer shell and bonding electrons. Additional comments on this subject are given in Appendix A.

No figure is given for the **screw dislocation** since it is invisible in projection. Also, definitions of glide and shuffle are irrelevant for this dislocation since shearing on either plane yields the same core structure. More conceptually, one notes that a screw dislocation has no terminating half-plane.

Hornstra gave two forms of the **Lomer dislocation** (fig. 2-2, bottom). With its {100} glide plane, this dislocation is not found in the early stages of deformation. It does appear though in grain boundaries, such as may be fabricated by crystal growth. Though not so obvious, the shuffle/glide definition applies to these models. This edge dislocation may be viewed as consisting of a {111} half-plane ending on a {111} plane at an angle of 71.53°, these being the two {111} planes normal to the {110} plane of the figure. As for the 60° dislocation, the half-plane may then end on widely spaced or narrowly spaced planes. Since the dislocation is not mobile, the glide/shuffle question is less important here, essentially providing a starting point for consideration of possible core structures for this defect. The glide model is free of unpaired electrons and will appear again in discussions of grain boundary structure.

Like the Lomer dislocation, the **45° and edge dislocations** are not found in deformed samples, but may be found in grain boundaries. Here though, the dislocations do not lie in a {111} plane, leaving the glide/shuffle description inapplicable. In any case, the two atom basis still leads to two different models. The extra "half-plane" of the edge dislocation clearly manifests itself as a pair of planes from each

FCC lattice (fig. 2-3, top). The two atom basis manifests itself by allowing the half-plane to end at a single column of atoms or a pair of columns. The former has no broken bonds, while the latter appears physically unlikely.

The 45° dislocation is probably most difficult to visualize without a three dimensional model. Hornstra originally gave two models for this dislocation. Examination of three-dimensional models lends support to a version of one of these possessing no broken bonds, given in fig. 2-3, bottom. The edge component of the Burgers vector (in the plane of the paper) is $\frac{a}{2}$ <100>. This may be interpreted as two non-parallel {110} half-planes ending at the dislocation core. These are indicated with bold lines.

These last two dislocations will be encountered again in Sec. 3 due to their role in <100> tilt grain boundaries.

2.2. Partial Dislocation Structure

Dislocations commonly dissociate in low stacking fault energy materials. In this process, a perfect dislocation splits into two partial dislocations joined by a stacking fault, the total Burgers vector remaining equal to that of the original dislocation. This reaction is possible when the strain energy of the resulting dislocations is less than the perfect dislocation. As the partials move apart on the dislocation glide plane, a stacking fault is left behind due to the non-lattice Burgers vector of the partials. The stacking fault has an interfacial energy associatied with it, i.e. a surface tension, which balances against the repulsion between the two partial dislocations. This leads to an equilibrium separation between the two partials. Naturally, when the stacking fault energy is too high, a dislocation will not dissociate even if dislocation strain energy would be reduced.

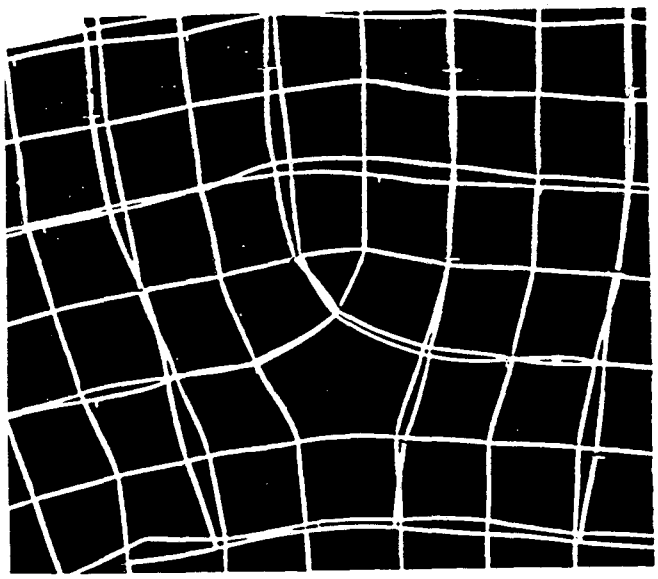

Edge Dislocation

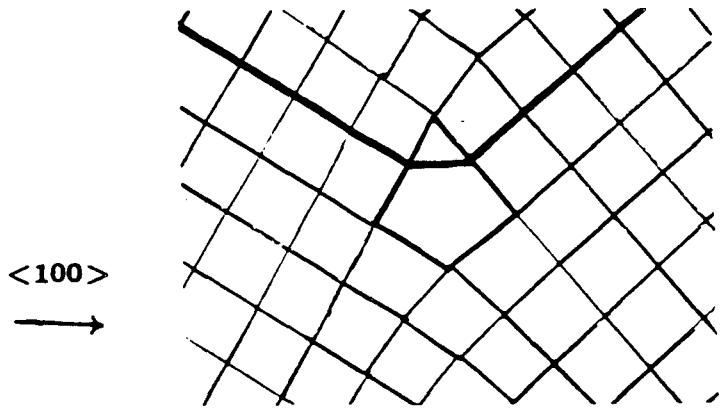

45 ° Dislocation

Fig. 2-3 The two perfect dislocations lying along the <100> direction (from three dimensional model constructions). The edge dislocation is distinguished by a triangle and pentagon sharing a vertex while in the 45 ° dislocation these same polygons share a side. There is no glide/shuffle distinction in this projection. The edge dislocation may readily be viewed as a pair of FCC {110} half-planes ending at a shared site. The screw component of the 45 ° dislocation is invisible in projection. Here, it may be viewed as possessing two non-parallel <110> half-planes (emboldened). XBL 855-2555

Stacking faults in silicon are common on the {111} glide plane due to its low stacking fault energy. This is so because first and second nearest neighbor relationships are not disturbed by the fault (fig. 2-4). For this reason, dislocations lying in {111} planes are expected to dissociate if the resulting partials will have lower strain energy. Of the dislocations discussed in the previous section, only the screw and 60° dislocations may dissociate on their glide plane.

In FCC materials, the partials bounding the stacking fault either have Burgers vector of type $\frac{a}{6}<112>$ (Shockley partials) or of type $\frac{a}{3}<111>$ (Frank partials). Shockley partials are glissile and the type encountered in dislocation dissociation while Frank partials may only move via climb, forming usually by the precipitation of vacancies or interstitials. Attention is therefore limited to Shockley partials.

Referring to the Thompson tetrahedron (fig. 2-4,bottom), one finds three possible Burgers vectors for a Shockley partial in its {111} glide plane. For a partial dislocation lying along a <110> direction, two of these are 30° partial dislocations while the other is a 90° (edge) partial. The 60° dislocation may dissociate into a 30° and a 90° partial while the screw dislocation splits into two 30° dislocations, in each case bordering an intrinsic stacking fault (schematically depicted in fig. 2-5). A three-dimensional model of a split 60° dislocation is pictured in fig. 2-6 with a <110> projection in fig. 2-7.

The relative direction in which the partials dissociate is not arbitrary. One choice gives the intrinsic fault mentioned above while the other gives a high energy fault of type:

-----ABCABCA|ABCABC-----

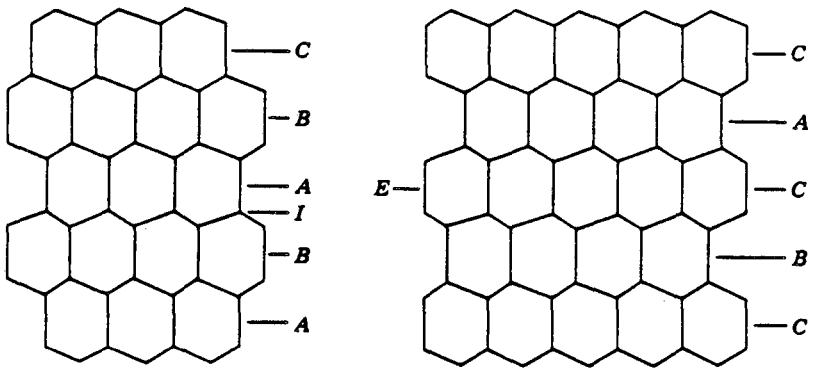

Stacking Faults

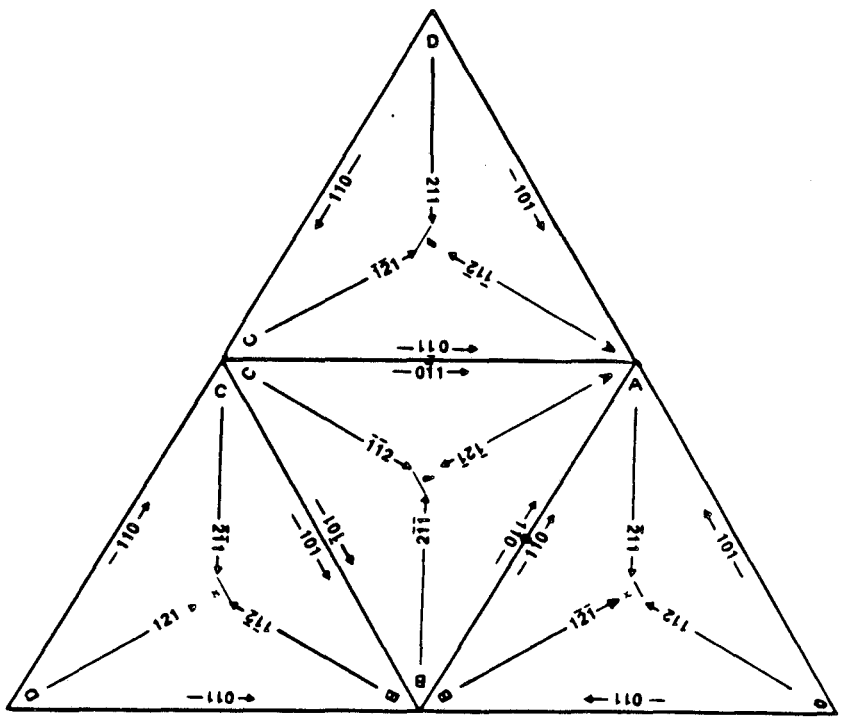

Thompson Tetrahedron

Fig. 2-4 (**top**) Intrinsic (left) and extrinsic (right) diamond structure stacking faults. Pairs of planes are labeled. (**bottom**) The Thompson tetrahedron aids interpretation of dislocation reactions. XBL 855-2560

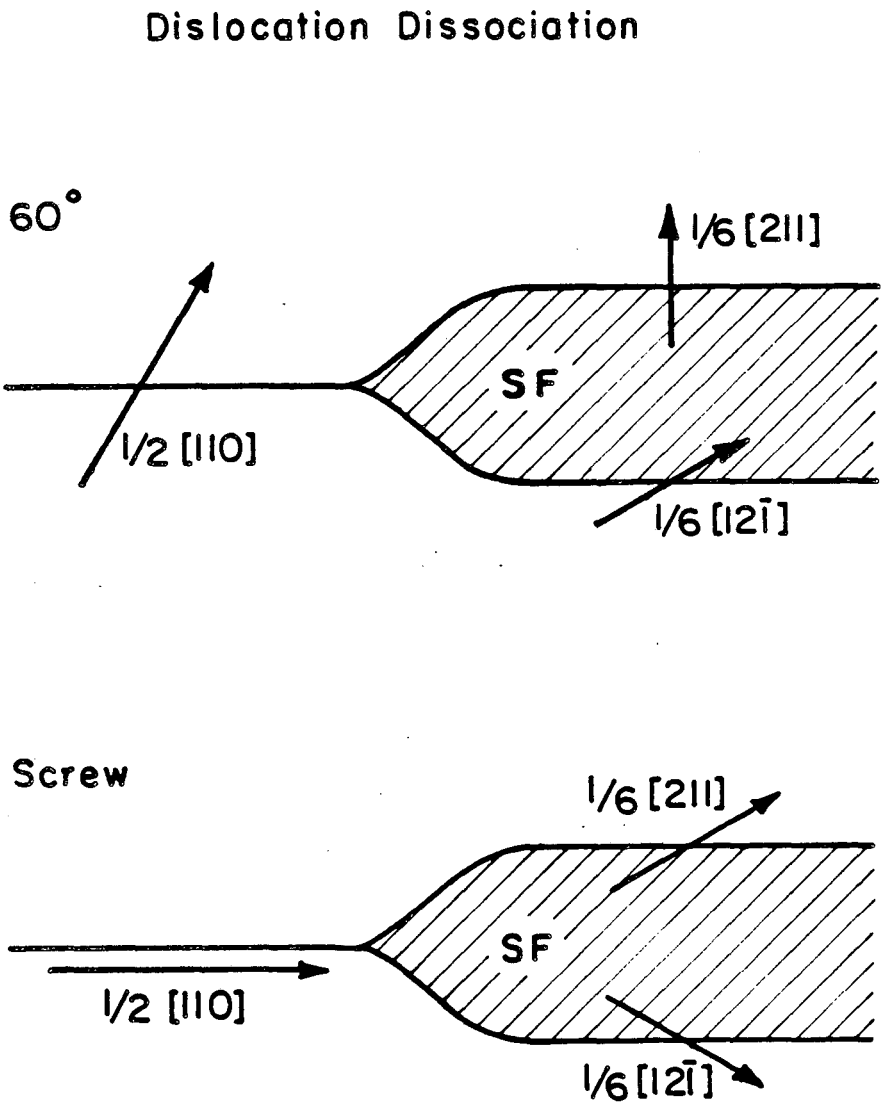

Fig. 2-5 Schematic illustrations of the dissociation of the common perfect silicon dislocations. A dislocation with Burgers vector $\frac{a}{2}<110>$ splits into two Shockley partial dislocations (Burgers vectors of type $\frac{a}{6}<211>$), bounding an intrinsic stacking fault. XBL 855-6287

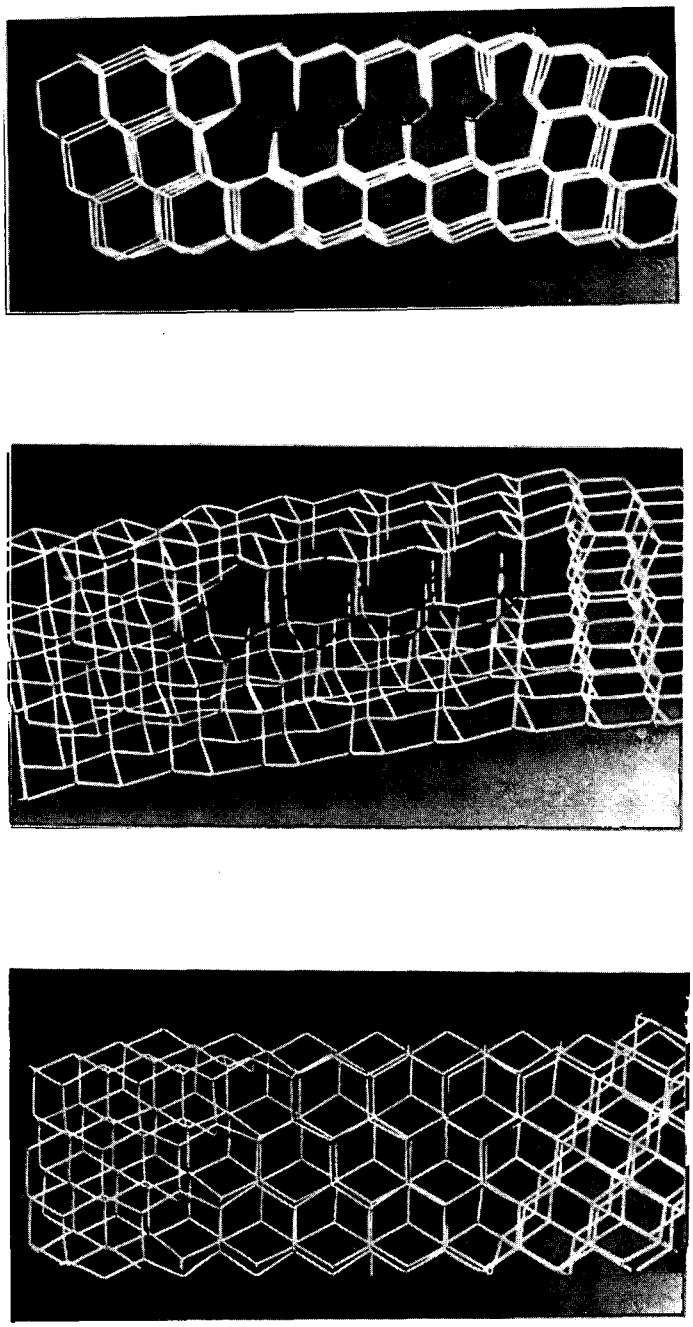

Fig. 2-6 Three views of a model of a split 60° dislocation; top- along the dislocation line direction, middle- angled view, bottom- looking down on the stacking fault. The unpaired "bonds" of the 30° partial (left) are most visible in the bottom figure. CBB 851-499

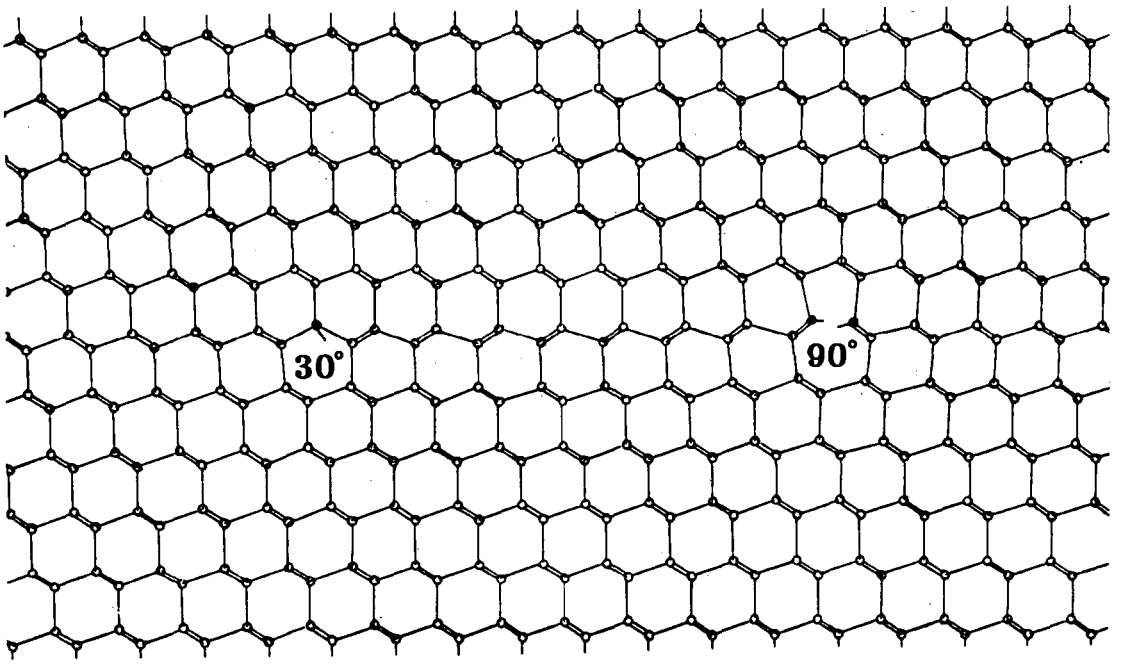

a

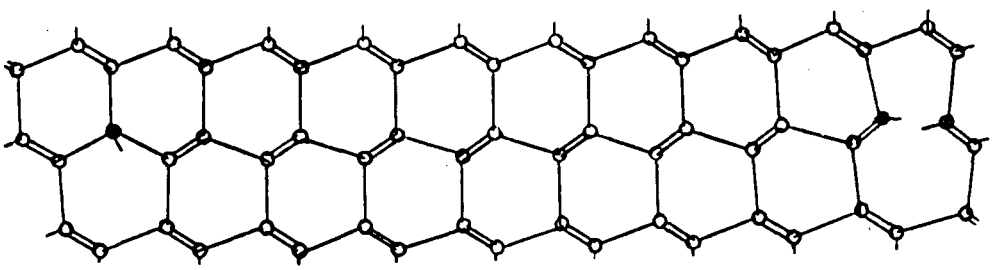

b

Dissociated 60 ° Dislocation

Fig. 2-7 Projected view of a dissociated 30 ° dislocation along the dislocation line. A closeup view of the partial dislocation cores and stacking fault is given in (b). The single unpaired electron in the 30 ° dislocation core and two in the 90 ° core per {110} plane pairs (normal to the dislocation) are indicated. XBL 855-2561

which is unacceptable. In principle, this may transform to a faulted dipole and an extrinsic fault bound by Shockley partials, providing a mechanism for the production of extrinsically faulted dissociated dislocations. Fairly recently, such extrinsic faults have been observed in silicon and are assumed to require high temperature deformation.[11] In the remainder of this thesis, attention is limited to the 60° and screw dislocations commonly found in silicon deformed at relatively low temperatures (750°C and below).

The two atom basis again complicates structural considerations. If a glide dislocation dissociates (shearing between narrowly spaced planes) an intrinsic stacking fault is produced. A shuffle dislocation dissociating directly on widely spaced planes would produce a high energy fault of type:

-----AaBbCcAaB|aBbCcAaBbCc-----

It is generally assumed that such a fault cannot be produced. However, a shuffle dislocation may in principle dissociate *indirectly* by producing a stacking fault on a neighboring plane to that of the dislocation glide plane, i.e. on narrowly spaced planes again yielding an intrinsic stacking fault. This process may be described as occuring by the nucleation of a dislocation dipole on a {111} plane adjacent to the shuffle dislocation. The partials in the dipole bound an intrinsic stacking fault with one of them neighboring the original dislocation. This latter association of dislocations takes on a new character, no longer appearing physically as two distinct dislocations, but having a single core with the Burgers vector of a partial dislocation. This dislocation's glide plane is that of a glide dislocation, while its appearance is that of a shuffle dislocation since its half plane still ends on the same widely spaced planes of the original perfect

shuffle dislocation. Hirth and Lothe's description is most physically appropriate: it is a glide partial associated with a row of vacancies or interstitials.[8] The reactions are schematically given in fig. 2-8.

The curious observation here, which leads to some confusion in the literature, is that the shuffle dislocation, upon dissociating, contains glide partial dislocations. To simplify the remaining discussion, glide partials associated with vacancy or interstitial rows will be called "shuffle partials".

In principle, there are several potential configurations for the **split 60° dislocation**. A glide type is one possibility while the shuffle type may dissociate in four different ways; a vacancy or interstitial row appearing in either the 30° or 90° partial. In addition, if one does not require the split dislocation to have its origin in a perfect dislocation, additional options arise. Since each of the two partials has three possible configurations - glide type, glide plus a row of vacancies (the half-plane ends "above" the stacking fault), or glide plus a row of interstitials (ending below the stacking fault) - there must then be *nine* different total dislocation configurational possibilities. Allowing that diffusion may permit any of these structures to occur, all should be taken into account since the dislocation will approach the core configuration of lowest energy.

Models were made of all these leading to the conclusion that excessive strain in the dislocation core may safely eliminate all but two possibilities. These are the dissociated glide and a shuffle type with a vacancy column in the 30° partial. Models of these are given in fig. 2-9. Geometrically, the former has one unpaired electron per atom along the edge of the half-plane while the latter has three. This suggests that the glide type dislocation is energetically preferred. These are also the two potential

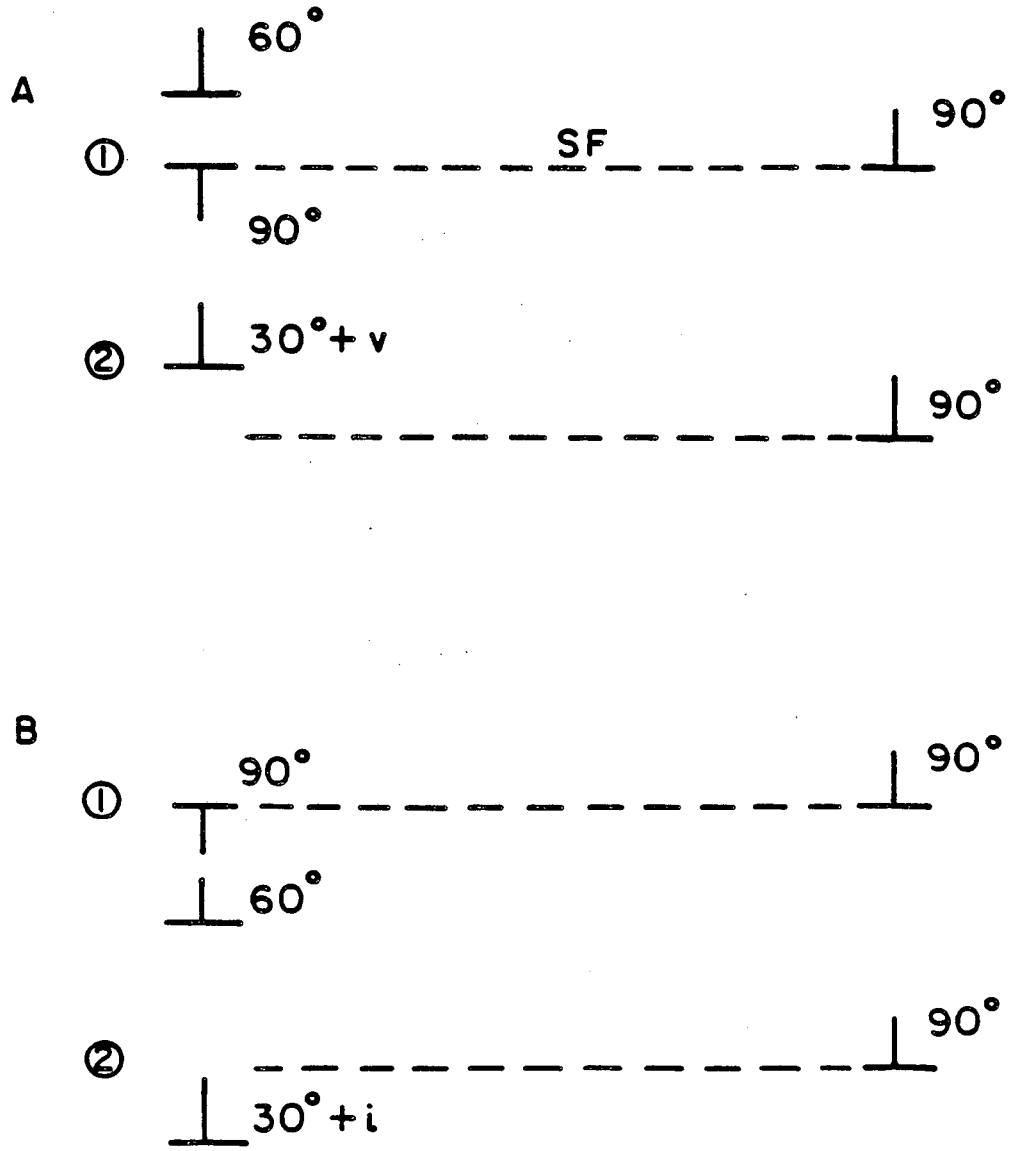

Fig. 2-8 60° dislocation dissociation reactions. (**A**) A 60° dislocation associated with a 90° dislocation dipole lying one plane below the end of the half-plane [1] is equivalent to a split 60° dislocation in which the 30° partial possesses a row of vacancies [2]. (**B**) Similarly, a dipole lying one plane above the 60° dislocation half-plane [1] leads to a 30° partial containing a row of "interstitials" [2]. XBL 857-6404

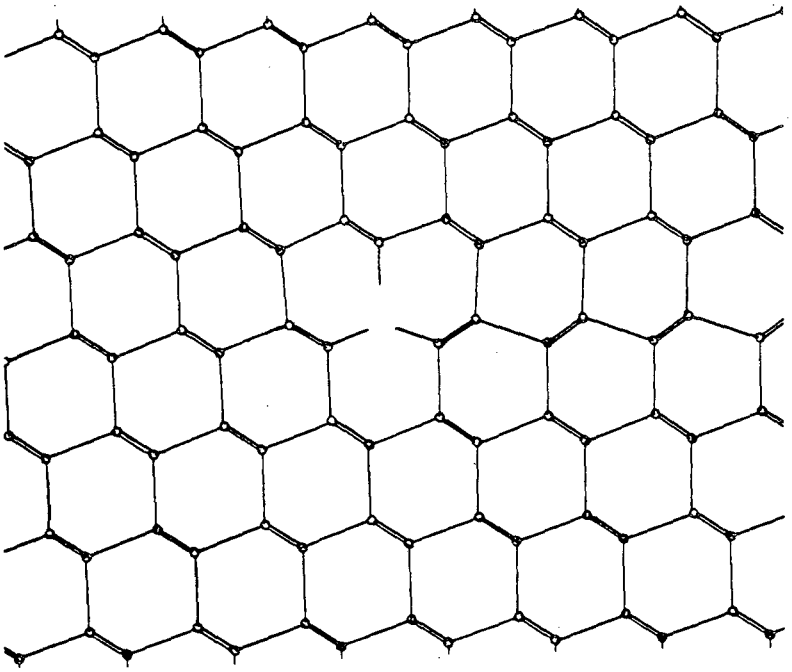

30 ° + Vacancy Row

Fig. 2-9 The two shuffle configurations of the 30° dislocation. The vacancy form is obtained by removing a row of atoms (inserting a row of vacancies) into the glide model while the interstitial form has an added row of atoms (filled circles). Note that the bottom figure is upside down with respect to the top. XBL 855-2562

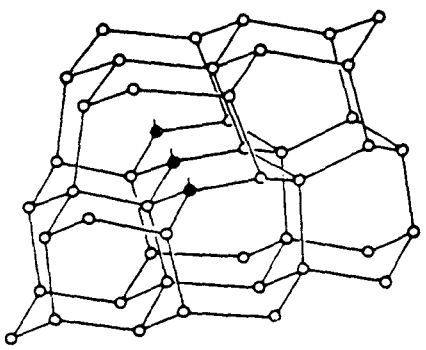

30 ° + Interstitial Row

models generally assumed to be possible in the literature though without explanation.

The **screw dislocation** as noted earlier is neither glide nor shuffle. Since Hornstra assumed only shuffle partials exist, his split screw model has a vacancy row in one partial and an interstitial row in the other.[7] However, as indicated above, these two partials are expected to have substantially different core strain energies. One might then expect that both partials would assume the same form, i.e. that of lowest energy. This leads us to postulate a screw with two glide partials or with two shuffle partials of vacancy type. The latter situation does not correspond to a simple dislocation: if its partials were to combine a perfect screw dislocation associated with a double row of vacancies would be obtained. Apparently, this last possibility has not been discussed in the literature. An important conclusion here is that both partials in a screw dislocation should be examined. A figure for the screw dislocation is not given since its partials are identical to the 30° partials of the 60° dislocation.

CHAPTER 3

Grain Boundary Structure

In this chapter, grain boundary structural theories will be outlined followed by a discussion of their relavence to grain boundaries in tetrahedrally coordinated, covalently bonded materials. Lastly, consideration will be given to specific modeling schemes for diamond structure grain boundaries.

3.1. General Theory

Lattice Dislocation Grain Boundaries

Macroscopically, grain boundaries may be described in terms of five degrees of freedom; three for the relative rotation between the two lattices and two for the choice of the grain boundary plane. Early studies assumed that the material composing the grain boundary was essentially amorphous. In 1939, Burgers demonstrated that grain boundaries of small misorientation (low-angle) could be described in terms of regular arrays of dislocations[12] which yield strain free grains. This model has since been well established experimentally for all crystalline materials.

The simplest type of boundary is the symmetric tilt; that is, with the rotation axis lying in a boundary plane which has mirror or glide symmetry. Assuming a Burgers vector perpendicular to the boundary plane exits, only one set of parallel edge dislocations is required (otherwise, two sets). Rotation of the grain boundary plane away from a symmetric orientation requires addition of a second set of dislocations. A pure twist boundary necessitates two sets of crossing screw dislocations. For a general

boundary, three sets of dislocations with non-coplanar Burgers vectors are required.

Coincidence Site Lattice Theory

As the angle of misorientation increases, the density of the dislocation mesh increases: hence the dislocation cores grow closer. As the cores begin to overlap, the dislocation description loses physical meaning, this occuring for misorientations of approximately 25°.

Though such high-angle *general* grain boundaries were thought to have energies similar to a free surface, it was recognized in 1927 by Friedel[13] that at *special* orientations a grain boundary could contain a portion of lattice sites common to both grains. Such boundaries (which include twins) were expected to have significantly lower surface energy than a general boundary. Specifically, one obtains the common sites for a given misorientation by allowing the lattices of either grain to extend throughout space. The common sites give a superlattice or *Coincidence Site Lattice* (CSL), which is independent of boundary plane. Naturally, this description requires the rotation axis to intersect a pair of common lattice sites. The CSL also leads to a simple catagorization of special grain boundaries according to the reciprocal of the fraction of shared lattice sites, by definition Σ. (Throughout the following, Σ=# is abbreviated as Σ#). While Σ values up to 11 belong to a unique misorientation, larger values of interest (to Σ55) correspond to two or three distinct possibilities. These are distinguished by a letter suffix, e.g. Σ27a and Σ27b.

Mathematically, any misorientation between two objects may be expressed as a rotation of some angle θ about a single common axis. This leads to the so called axis-angle pair description of grain boundaries.[14] In general, a given relative misorientation

of two cubic lattices has 24 different axis-angle pair descriptions. By convention, that with smallest θ or lowest index rotation axis is selected. With cubic symmetry, θ may extend to 45° for a <100> rotation axis and 90° for <110>. For illustration, a $\Sigma 9$ CSL is equivalently given by <110>/38.94°.

The extension of this theory to actual grain boundaries comes in the assumption that lowest energy boundary planes will tend to intersect a high density of CSL points, minimizing the structural mismatch of the grain boundary. In general, symmetric boundary planes are expected to offer lowest energy of the infinite number of possible boundary orientations for a single CSL. For both the <100> and <110> rotation axis CSL's, this leads to two possible boundary orientations; either with a {100} or {110} plane in the median lattice. (By definition, the median lattice is a reference lattice midway in orientation between the two grains, i.e. at $\theta/2$ from either grain.)

The definition of the axis-angle pair may now be extended to allow its use for designation of specific grain boundaries. Firstly, limiting consideration to symmetric boundary orientations, each axis-angle pair now corresponds to two different grain boundaries. Next, the median plane is taken to be {110}. From this viewpoint, θ may extend above 45° and 90° for <100> and <110> respectively to give the second possible symmetric boundary plane orientation (i.e. that with {100} median plane). For example, a $\Sigma 9$ <110>/38.94° grain boundary by definition has a {110} median grain boundary plane while the identical CSL $\Sigma 9$ <110>/141.06° is associated with a {100} median plane, this leading to a different boundary structure. Though axis-angle pairs will occasionally be used to refer just to the CSL, this should be clear in context. The physical sense and usefulness of this description will manifest itself in the

following sections.

As reference, important (high coincidence) CSL grain boundaries are given in Table 3-1 in order of increasing θ. Note that these grain boundaries are also twins due to their mirror symmetry. However, in most cases they are not naturally occuring and so are twins only in the geometrical sense.

Clearly then, CSL theory only gives a qualitative prediction of relative grain boundary energies, but continues to be very useful due to the lack of a fundamental theory based on solid state physics.

O-Lattice Theory

The CSL theory was further extended and unified with the dislocation description of low-angle grain boundaries by the development of Bollman's O-lattice theory.[15] This theory provides a detailed matrix algebraic basis for the prediction of the dislocation structure of an arbitrary grain boundary.

First consider low-angle grain boundaries. The concept of coinciding lattice points is generalized to a coincidence of equivalent points in space. These *O-points* generally form a periodic array of parallel lines of well matched spatial coordinates extending in the direction of the rotation axis. The intersection of the chosen boundary plane with the O-lattice then gives a set of points corresponding to sites in the grain boundary of good geometrical matching. These points are then allowed to expand to regions of perfect matching while the mismatched regions are confined to lines which are geometrically equivalent to dislocations. The theory then reduces to the Read-Shockley[16] dislocation description for low-angle grain boundaries.

Cubic CSL Symmetric Grain Boundaries					
<110>			<100>		
Σ	θ	Grain Boundary Plane	Σ	θ	Grain Boundary Plane
1	0°	{110}	1	0°	{110}
33a	20.05°	{441}	41a	12.68°	{540}
19a	26.53°	{331}	25a	16.25°	{430}
27a	31.58°	{552}	37a	18.92°	{750}
9	38.94°	{221}	13a	22.62°	{320}
11	50.48°	{332}	17a	28.07°	{530}
41c	55.88°	{443}	5	36.87°	{210}
33c	58.98°	{554}	29a	43.61°	{730}
3	70.53°	{111}			
17b	86.63°	{433}			
----	----------	----------	----	---------	----------
17b	93.37°	{322}			
3	109.47°	{211}			
33c	121.02°	{522}	29a	46.39°	{520}
41c	124.12°	{833}	5	53.13°	{310}
11	129.52°	{311}	17a	61.93°	{410}
9	141.06°	{411}	13a	67.38°	{510}
27a	148.42°	{511}	37a	71.08°	{610}
19a	153.47°	{611}	25a	73.75°	{710}
33a	159.95°	{811}	41a	77.32°	{910}
1	180°	{100}	1	90°	{100}

Table 3-1: Symmetric CSL grain boundaries in the FCC lattice.

The power of the O-lattice theory manifests itself in the extension of the overly simple CSL description of special high-angle grain boundaries. At rotations of exact

CSL orientation, the O-lattice description gives potentially well matching grain boundary planes free of dislocations. As for a near $\Sigma 1$ (low angle) grain boundary, a misorientation from the exact CSL introduces dislocations in the grain boundary plane which preserve the configuration of the CSL between the dislocations. However, these grain boundary dislocations (GBD) no longer have perfect lattice Burgers vectors. Rather, their Burgers vectors come from the set of vectors connecting all lattice sites of the two grains to each other. This set of vectors makes up the *displacement shift complete* (DSC) lattice. Note that perfect lattice vectors are a subset of this. Translation of one grain relative to the other by a DSC vector preserves the symmetry of the grain boundary, just as translation of a lattice by a lattice vector preserves the original lattice. Small misorientations from the exact special boundary are accomodated by DSC Burgers vector dislocations which are unique to the grain boundary. These dislocations are termed *secondary* as opposed to the primary, lattice Burgers vector dislocations.

Lastly, O-lattice theory allows consideration of possible rigid body translations ignored by CSL theory. It is expected that many grain boundaries will obtain lower energy configurations with the introduction of a relative translation between the two grains, this amounting to an additional three geometrical degrees of freedom. While such a translation destroys the lattice site coincidence required by the simple CSL approach, the O-lattice remains intact reflected in the continuing periodicity of the grain boundary structure.

Bicrystallography

A few researchers have extended crystallographic theory to the description of grain boundary symmetry. Two viewpoints have been taken, as described below.

Pond and Bollmann[17] have applied the concepts of color symmetry[18] to the description of grain boundaries. One grain is designated as white, the other black. Color reversing symmetry elements are indicated with a " $'$ ". For example, a twin boundary has a m$'$ (color mirror) plane parallel to the grain boundary plane. All such symmetry elements lie in the boundary plane while all conventional elements are perpendicular to it. In particular, the three translation symmetry axes of a single crystal are reduced to 0, 1, or 2 translation axes in a bicrystal. In the case of symmetric tilt boundaries, only the translation symmetry axis perpendicular to the grain boundary is lost.

Next, consider the effect of a relative translation of the two lattices. To define the reference state for measurement of a rigid body translation of τ, the rotation axis is assumed to intersect coinciding black and white lattice sites in the untranslated ($\tau = 0$) state. For a CSL, the rotation axis intersects any of the parallel rows of CSL sites: by definition, a CSL exists only for $\tau = 0$, assuming a single atom basis. Introducing a translation separates these sites, destroying the CSL. This separation is given by τ. Obviously, the value of τ depends on the black and white sites selected for measurement. By convention, those giving the smallest value are taken. For crystals with multi-atom bases, the atom giving highest bicrystal symmetry is defined as the origin for translation measurements.

A rigid body translation may affect the point symmetry, but not the translation symmetry, i.e. the grain boundary periodicity remains. Ordinary symmetry elements

are conserved if τ is parallel to the element. Color symmetry elements survive if τ is perpendicular to the element and the element is shifted in location by $\frac{1}{2}\tau$. For example, movement of the right-hand grain by τ perpendicular to an m′ plane shifts the m′ plane by $\frac{1}{2}\tau$. A translation parallel to a mirror plane creates a mirror-glide plane.

For non-holosymmetric crystals, the situation grows more complicated. In the case of a diamond structure bicrystal, a translation of one grain by $\frac{a}{4}<111>$ maintains atomic site coinsidence, though leading to a bicrystal of different symmetry and structure. The importance of these two options will be demonstrated by the $<110>$ tilt boundaries of Sec. 3-2. There, the above choices lead to two distinct though physically viable grain boundary core models.

Gratias *et al.*[19] have described bicrystals from the viewpoint of group theory. Their development is closely related to the O-lattice approach and is satisfying fundamentally. However, they do not take the grain boundary plane into account and so are somewhat removed from the viewpoint of the electron microscopist.

Structural Unit Theory

To this point, no mention has been made of details of atomic configuration. The geometrical models discussed above only provide a starting point for these considerations. Research on atomistic models has largely been limited to FCC metals which may be physically approximated with hard sphere or bubble raft constructions or via computer calculations of minimum energy configurations which assume spherically symmetrical, central force potentials. Such modelling does not provide a theoretically fundamental basis for the predition of grain boundary atomic structure, however it has led to a number of insights which have been experimentally supported.

Most computer calculations have been performed on FCC metals of symmetric tilt boundaries,[20] this being easiest to model. The following discussion is therefore in terms of the 2-D projected structure of the grain boundary. These studies have led to the observation that such grain boundaries consist of a series of contiguous, atomic scale *structural units*. These units are simply building blocks consisting of a group of several closely packed atoms forming a polyhedron. Tilt grain boundaries consist of ranges of misorientations each consisting of uniformly spaced series of two distinct structural units. At the limit of these ranges are grain boundaries made up entirely of a single type of repeating unit. These latter boundaries correspond to some CSL orientations and have been termed *favored* boundaries.[21] The structural units in intermediate orientations thus originate in the neighboring CSL boundaries. Other CSL orientations, some having fairly short repeat units, simply contain two units originating in favored boundaries. Aside from their periodic structure, such boundaries are similiar to general boundaries.

From this perspective, a misorientation in a favored boundary introduces *foreign* structural units from the next occuring favored boundary, thereby accomodating the misorientation. The foreign units are associated with DSC dislocations. The structural unit theory is thus reconciled with O-lattice theory. The precise atomic positions within the structural units naturally will vary with misorientation, however the essential features of the units are preserved.

3.2. Silicon and Germanium Grain Boundaries

One must now ask how relevant the previous discussion is to grain boundaries in semiconductors. One expects the low-angle, dislocation model to apply directly: this

has been experimentally demonstrated in simple tilt and twist boundaries in, for example, germanium,[22] silicon[23],[24] and gallium arsenide.[25] However, the CSL and O-lattice theories only account for good coordinate matching, while in semiconductors the highly directional bonds must be expected to play an important role. An extended O-lattice theory taking account of bond directions may prove desirable though it has yet to be attempted. In any case, recent observations have demonstrated the existence of DSC dislocations in some germanium grain boundaries.[26],[27],[28] So, this description is assumed to possess at least partial validity. In addition, as described below, previous structural studies of diamond structure grain boundaries have employed CSL theory as a useful framework. Most simply, this arises since CSL's give periodic grain boundary structures, low Σ values in particular giving short periods.

Though HRTEM work on germanium and silicon grain boundary atomic structure began in 1977, the theoretical foundations essentially were developed in the late 1950's by Kohn[29] and, in particular, by Hornstra.[30],[31] Since Kohn's work described grain boundaries arising from naturally occurring twinning in silicon, a brief discussion is worthwhile here.

Twin boundaries ($\Sigma 3$, $\{111\}$) have long been recognized as occuring in diamond crystals. This is attributed to the very low surface energy of the boundary which only disturbs bonding beginning with third nearest neighbors while the bonding energy is concentrated in the nearest neighbor, covalent bonds.

Muliple twinning operations during grain growth can lead to grain orientations in addition to $\Sigma 3$ $<110>/70.53^\circ$. For example, two twinning operations (rotation of 70.53° about a $<110>$ axis) lead to two possible new orientations; the first the trivial case of zero net rotation and the second with the axis-angle pair $<110>/38.94^\circ$

(141.06°). Referring to Table 3-1, one notes that this is a Σ9 CSL. A third twinning operation gives two non-trivial options (plus Σ3). Rotation about the same <110> axis produces <110>/31.58° (148.42°) which is Σ27a while rotation about a different <110> axis produces a non-CSL orientation. Additional twinning produces CSL's of increasingly low density (Σ81, Σ243, etc.)

Due to their origin, Σ9 and Σ27a grain boundaries are often called second-order and third-order twins, respectively. Since they occur indirectly and have distortions in first nearest neighbor coordination, Kohn suggested they may be more accurately called "high-order joins".[32] Their importance from the present point of view is that one may expect to find them in highly twinned silicon crystals and that they are <110> tilt boundaries and thus ideal for HRTEM: the structures under discussion are not artificially idealized.

In two seminal papers, Hornstra provided a general foundation for the discussion of tilt CSL grain boundaries with <110> rotation axis[30] and <100> rotation axis[31]. He attempted to model all θ's with $\frac{a}{2}$<110> Burgers vector dislocations. Only high density CSL's were considered since these give boundary structures of short period. In fact, Hornstra foreshadowed the development of the structural unit theory as attested in the following quote from his 1959 paper[30]:

> It is impossible, even in the case of a single rotation axis, to study the grain boundary structure for all values of the angle θ. Only those boundaries will be discussed which consist of single dislocations or small groups of dislocations at perfectly regular intervals. In these *regular boundaries* the period of the boundary pattern in any direction is a simple multiple of the lattice vector in that direction. In this case there exists a coincidence lattice... For other values of θ the boundary may be considered as a mixture of two regular boundaries, one with a larger and one with a smaller value of θ.

Though Hornstra gave no mention to grain boundaries in metals, hindsight allows us to rationalize the direct use of dislocations as structural units with the more abstract approach currently under development for metals. In metals, dislocation cores are expected to spread somewhat in high angle boundaries so that a structural unit may have no obvious relationship to a simple dislocation core. However, in semiconductors, the covalent bonding is expected to lead to narrow dislocation cores which may keep their essential configuration and a distinct identity when participating in a grain boundary. (Such assumptions are the basis for all models of semiconductor grain boundaries.) For this reason, though grain boundaries in metals have been studied far more than grain boundaries in silicon and germanium, the "structural unit approach" curiously appeared first as a useful descriptive tool for semiconductor grain boundaries.

<110> Tilt Grain Boundaries

Hornstra observed that boundaries with θ up to 26.53° (Σ19) could be modeled with separate Lomer dislocations. This has been observed in small-angle germanium grain boundaries by Bourret.[33] Hornstra's Σ19 <110>/26.53° model is depicted in fig. 3-1. This value of θ gives the minimum distance between dislocations without overlap. From a local viewpoint, the grain boundary contains five- and seven-membered rings in addition to the perfect lattice, six-membered rings.

For $\theta > 26.53°$, overlap of dislocation cores is accomodated with some new structural features. The cores may assume a "zigzag" arrangement (fig. 3-2, top) or two dislocation cores may combine to effectively produce a single core with an a <110> Burgers vector (bottom). These two possible components are at minimum

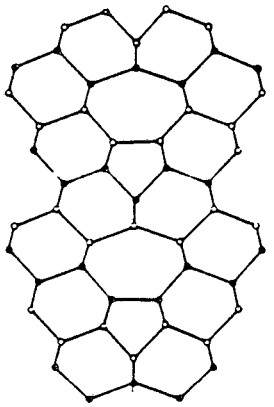

Σ19 (331)

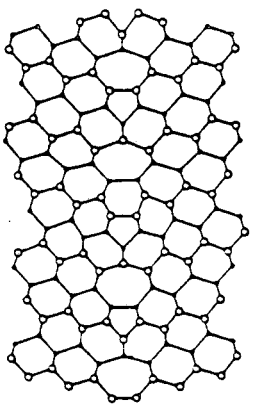

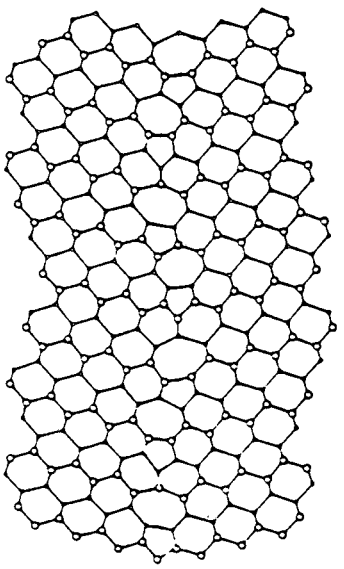

Σ27 (552)

Fig. 3-1 (**top**) The Σ19 {331} boundary has Lomer (edge) dislocation cores at minimum separation. There are two per grain boundary repeat distance (after Hornstra[30]) (**lower**) An increase in tilt rotation angle leads to a zigzagging of the cores (far left) or overlapping with the resulting appearance of boat-shaped rings (near above). This leads to the two possible models for the Σ27 boundary shown here (after Vaudin *et al.*[34]) XBL 855-2383

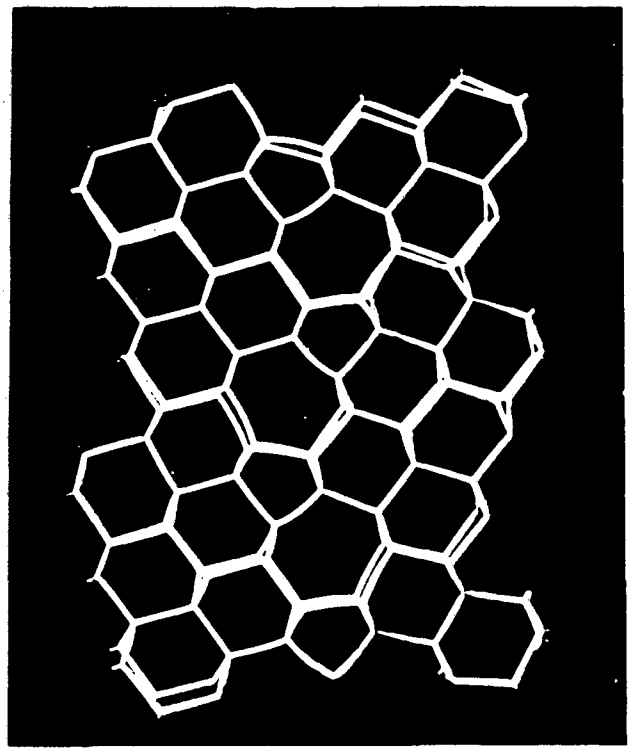

Σ9 (221)

Fig. 3-2 The overlapping or zigzagging Lomer cores reach saturation at the Σ9 rotation angle. The figure on the left is the zigzag model, that at the bottom the overlap model. Overlapping Lomer cores in effect produce a new dislocation core with Burgers vector a <110>. Note the mirror symmetry of this structure. XBB 855-3689

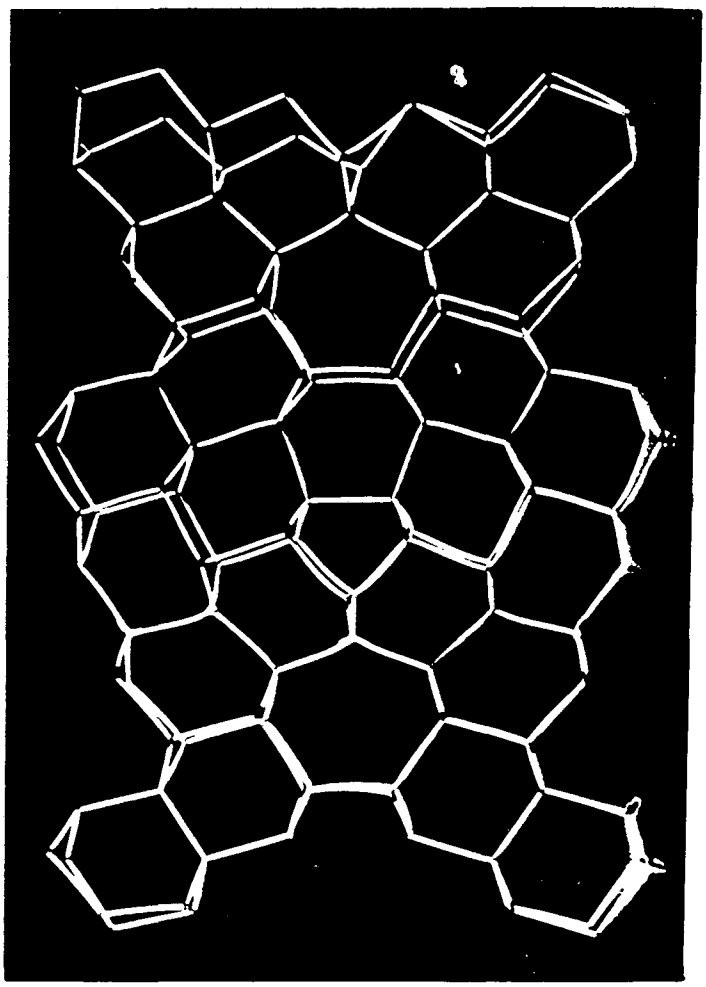

separation in this figure, a Σ9 grain boundary. Note that the two Σ9 models correspond to the two fundamental translation states (τ=0 or $\tau=\frac{a}{4}<111>$) alluded to in the previous section. The former case coincides with the overlapping dislocation model while the latter leads to the zigzag model. The author's plastic tube models give small differences in atomic positions from Hornstra's graphical approach. One assumes that the physical models more realistically approximate the true atom positions. Note that the zigzag model contains alternating five and seven-membered rings while the overlaping dislocation pair has a boat-shaped six-membered ring interposed between a five and a seven-membered ring. The boat-shaped ring (four staggered and 2 eclipsed bonds), as opposed to the perfect lattice chair-shaped ring (all staggered bonds) will be frequently encountered in other grain boundaries. Grain boundaries of θ between 26.53° and 38.94° are then expected to consist of either of the two possible Σ9 units and the Σ19 (Lomer dislocation) unit. Kohn was first to propose the Σ9 zigzag model,[29] though his aim was simply to select a grain boundary plane causing least distortion by allowing it to intersect CSL sites. He thus interpreted this model as consisting of faceting of the {221} boundary plane onto {211} planes.

As consequence to the above, the third order twin, Σ27, is expected to contain a combination of elements of the Σ19 and Σ9 grain boundaries, though Hornstra gave no models. Vaudin *et al.* suggest two possible models, the one given in fig. 3-1 (bottom) being supported by their HRTEM observations on CVD silicon specimens.[34] Note again the apparent preference for the zigzag type of Σ9 units.

For $\theta > 38.94°$, five and seven-membered rings must overlap. This combination produces a boat-shaped six-membered ring, as found in one of the Σ9 models (fig. 3-2, bottom). These boat-shaped rings are characteristic of the Σ3 {111} twin. So, as θ

increases, more boat-shaped rings are introduced - triple, quadruple, etc. dislocations as Hornstra described it - until the Σ3 orientation is reached. At this point, the boundary is of the expected simple twin configuration, entirely consisting of boat six-rings.

The next favored boundary, then, is Σ3 70.53°. Grain boundaries intermediate to Σ9 and Σ3 (such as Σ11, Σ41c, and Σ33c in Table 3-1) should contain elements of each. There are many ways of ordering the structural units in these (or any mixed) grain boundaries. For example, if a given grain boundary is required to consist of three units of type A and two units of type B, its actual structure could be AAABB, ABAAB, or ABABA. Since there is no *a priori* means of choosing amongst such possibilities, an experimental or calculational source of additional information is required. Papon *et al.* have studied the Σ11 50.48° grain boundary in germanium using electron diffraction and the α-fringe technique.[35] From examination of grain boundary periodicity and rigid body translation, they descriminate between several possible models. Their two preferred choices are given in fig. 3-3 (top).

For $\theta > 70.53°$, edge dislocations are added, reaching saturation for Σ11 129.53°. In other words, the number of boat 6-rings decreases until they are eliminated for Σ11.

Hornstra's models in this θ range contain broken bonds. However, Fontaine and Smith have proposed a broken bond free model for the lateral twin (Σ3 109.47°, {211} boundary plane), found in fig. 3-3 (bottom).[36] This boundary again contains 5- and 7-membered rings and boat-shaped rings as discussed above.

Since all models for Σ 11 129.52° appearing in the literature contain broken bonds, it is not clear if boundaries in the range $109.47° < \theta > 129.52°$ can be

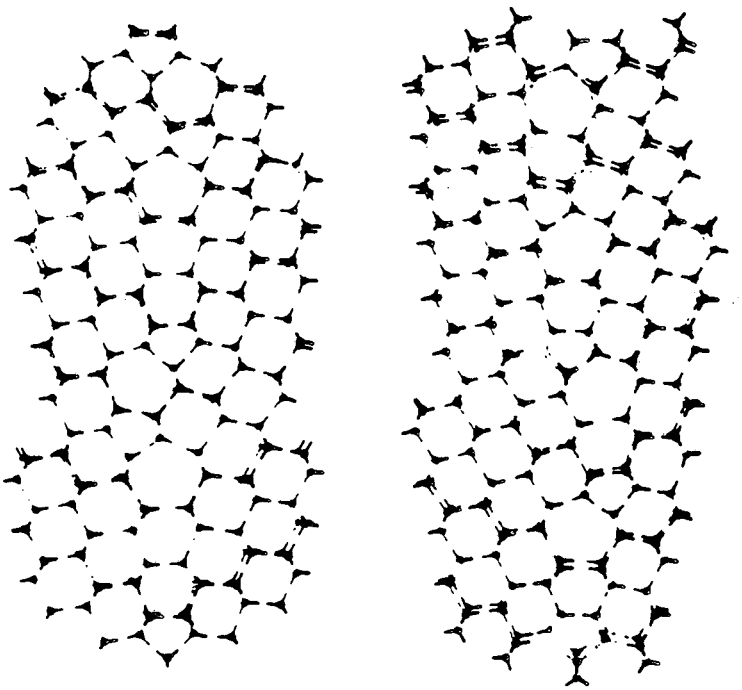

Σ11 (332)

Fig. 3-3 With increasing rotation angle, dislocation cores are forced to combine, producing boat-shaped rings. The individual structural elements within a single repeat unit may be arranged in several ways. Two possibilities for the Σ11 boundary are given on the left (after Papon *et al.*[35]) Note that these structures have twice the CSL predicted periodicity.

Σ3 (211)

Σ3 (111)

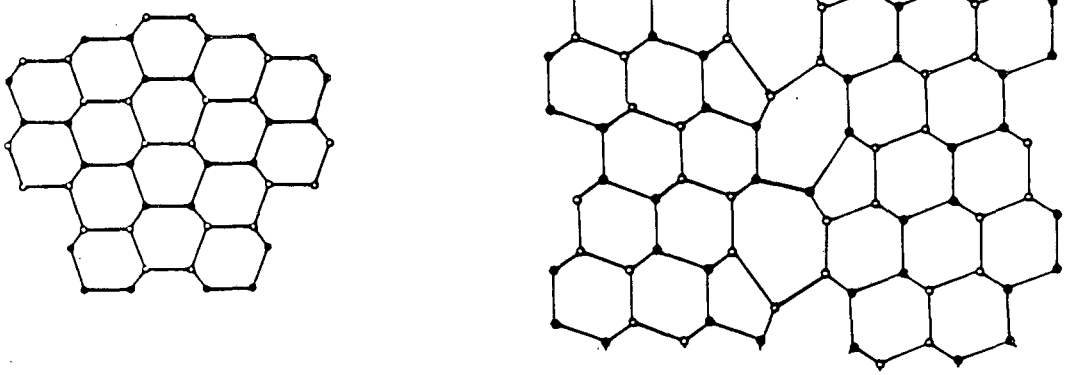

In the figure on the left, boat-shaped rings reach saturation for the common Σ3 twin. All five- and seven-membered rings have been eliminated. No bond length and direction distortions are required, unique to this boundary. The lateral twin (right) may in principle be formed without unpaired valence electrons (after Fontaine and Smith[36]) XBL 855-2384

modeled without broken bonds as might be expected.

Hornstra has modeled boundaries of $\theta > 129.52°$ as consisting of pairs of 60° dislocations, one broken bond per dislocation core. Apparently, broken bonds are unavoidable in this final range of θ (to 180°). It is simplest to treat these as low-angle boundaries with {100} median plane.

On the subject of general boundary orientations (asymmetric median planes), Hornstra pointed out that minima in dislocation density occur for {110} and {211} median planes, while {100} leads to a broad maxima. Thus, the later might be expected to facet onto more favorable planar orientations. Essentially, the goal here is to identify potentially universal features of grain boundary atomic structure which lend themselves to experimental examination.

<100> Grain Boundaries

Discussion of research into the structure of <100> tilt boundaries is necessarily limited in comparison to the previous section since relatively little work has been done on this subject. This has partially been due to the unavailability of electron microscopes with the requisite point to point resolution (1.9Å for silicon) for direct observations.

As described by Hornstra,[31] the situation here is simpler than for <110> tilt boundaries. For all values of θ, boundaries are modeled with either the edge or 45° dislocations (<100> line direction) described earlier. Small-angle boundaries with {110} median plane may consist of identical edge dislocations. As θ increases, all dislocation cores eventually touch for $\Sigma 5$ 53.13°. Hornstra's model is given in fig. 3-4 (top left). An alternative model for $\Sigma 5$ 53.13° using edge dislocations has been con-

Σ5 (310)

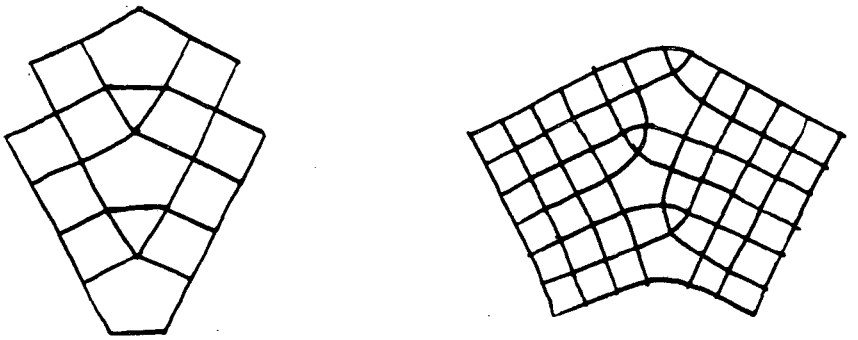

Σ5 (210)

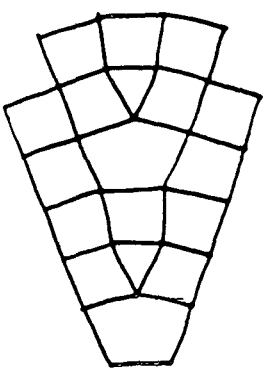

Fig. 3-4 Two models for the Σ 5 (310) grain boundary, at which dislocation cores touch. Hornstra's version[31] is on the left while Bacmann *et al.* recently proposed the alternate edge dislocation model to its right.[37] The Σ5 (210) grain boundary (left) has a {110} median plane. For this reason, it can be modeled with one set of edge dislocations. XBL 855-2385

structed by Bacmann *et al.*[37] (fig. 3-4, top right). It appears to be supported by their electron diffraction and α-fringe measurements.

For $53.13^\circ < \theta < 90^\circ$, boundaries may be constructed with pairs of edge or 45° dislocations. Either type gives the same dislocation density since the Burgers vector component perpendicular to the boundary plane of each pair is identical (and in the <100> direction of the median lattice). From this point of view, when all dislocations touch at $\theta = 53.13^\circ$, the resulting grain boundary is identical to that derived from the single dislocation model for $\theta < 53.13^\circ$. In fig. 3-5 are found the two possible models for two boundaries of intermediate orientation, $\Sigma 13$ 67.38° and $\Sigma 25$ 73.75°.

Summary

The salient observation is that the essential components of <100> tilt boundaries are homologous to those of <110> tilt boundaries (and indeed to dislocations). These structural elements are pictured in fig. 3-6. That is, the models proposed contain 5 and 7-rings (though no boat-shaped rings or broken bonds in the <100> boundaries). In projection, these are not apparent for <100> parallel defects. Here, the three-sided polygons mark the location of 5-rings while the 5-sided figures locate 7-rings. The question remains as to whether a description in terms of imperfect rings and broken bonds is preferable to one in terms of repeating units of favored boundaries. The later is useful for predicting possible configurations for specific grain boundaries, while consideration of both should yield insight into grain boundary properties.

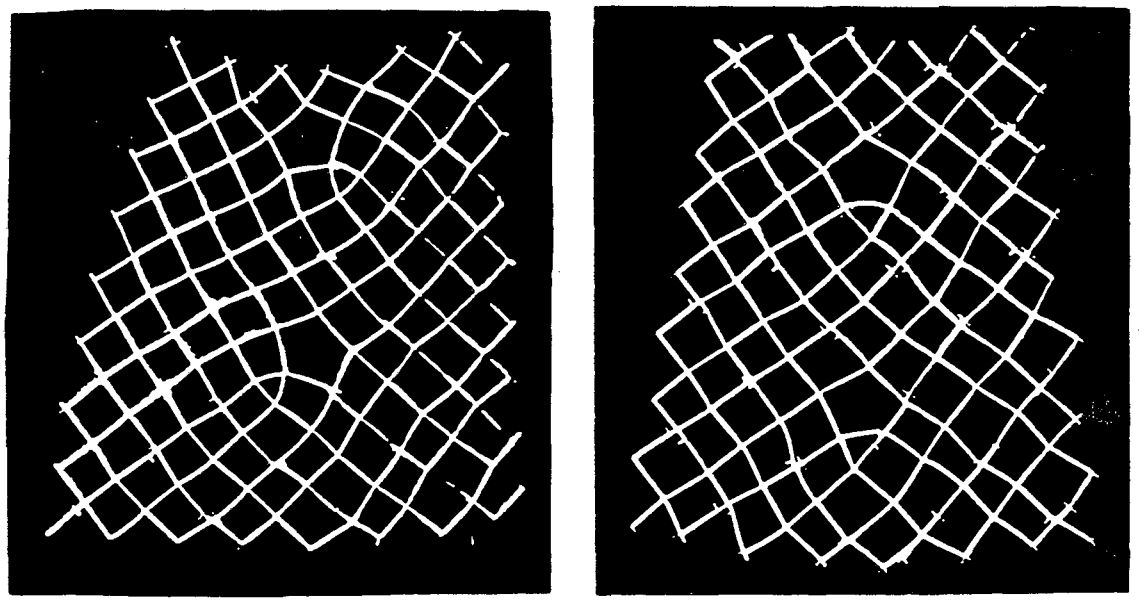

Σ25 (710)

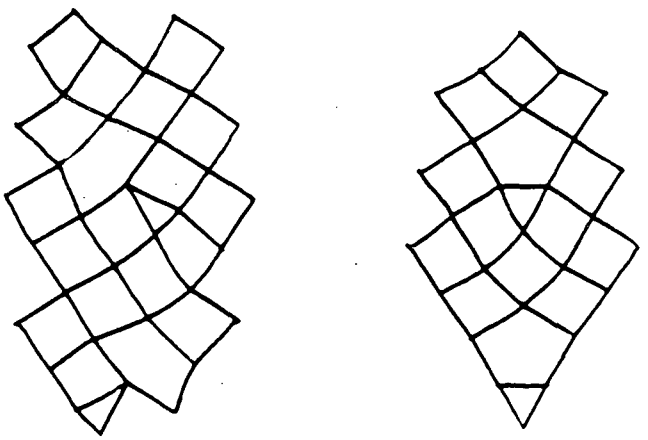

Σ13 (510)

Fig. 3-5 Examples of two-dislocation boundaries. On the left are versions with edge dislocations, on the right with 45° dislocations. The repeat unit length and net Burgers vector are independent of dislocation type. XBL 855-2386

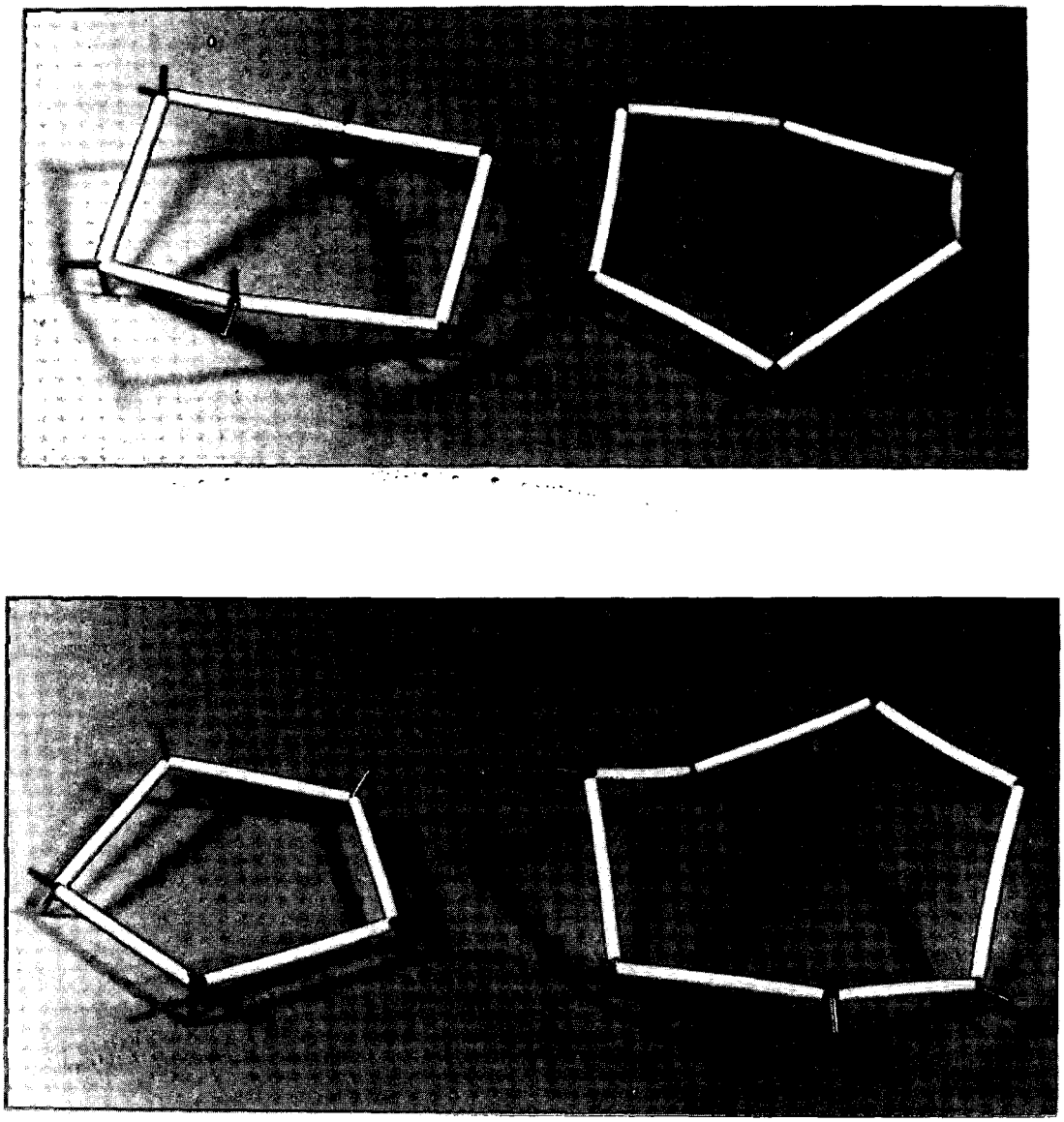

Fig. 3-6 Ring configurations found in diamond structure crystalline defects. The top left figure is a perfect lattice 6-membered ring (all bonds are staggered). To its right is a boat-shaped 6-membered ring. The lower right hand atom in effect has been flipped up. At lower left is a five-membered ring which is essentially planar. The seven-membered ring, lower right, is free to adjust its precise configuration. XBB 855-4033A

CHAPTER 4

Atomistic Segregation Models

The first section of this chapter reviews impurity segregation at dislocations and grain boundaries. With this background for perspective, the bias in the second section returns to the atomistic approach taken in the earlier discussion on defect structure. Models for impurities segregated at diamond structure dislocations and grain boundaries are suggested. Salient consideration is given to a model postulated for dopant segregation in the 30° dislocation core. In addition, models for interstitial metallic impurity segregation are offered.

In Chapter 7, these models serve as a basis for the discussion of the potential application of HRTEM for the study of impurities at defects.

4.1. General Concepts

Throughout this work, consideration is limited to undersaturated systems, i.e. no concern is given to the formation of additional phases. Two possibilities then hold:

(1) equilibrium segregation in which the concentration of impurity has achieved a free energy minimizing distribution with enhanced concentration in the vicinity of a defect or,

(2) nonequilibrium segregation such as may occur due to rapid diffusion of an impurity along a defect with concurrent diffusion into the neighboring crystal.

In the following, equilibrium is assumed to hold since the concern here specifically lies in learning more about the nature of energetically preferred impurity sites.

Most segregation phenomena arise from two physically distinct components; strain fields and bonding effects. Naturally, a combination of these may be involved in a particular situation. The latter is of essential concern in semiconductors due to the importance of electronic defects. Therefore, particular attention falls on the role of bonding in segregation in silicon, something simpler to model on an atomic scale than for non-directionally bonding materials. The following gives an overview of the currently perceived role of the above factors in impurity segregation.

Strain Field Segregation

A simple thought experiment to help elucidate segregation in a strain field is found in considering a pure edge dislocation in a crystal containing a small amount of substitutional solute. If the solute atoms are of a different size than the solvent atoms, a strain field is produced in their vicinity. In addition, the edge dislocation has regions of compressive and tensile strain, respectively "above" and "below" the edge of the dislocation half-plane. Solute atoms may reduce their contribution to the free energy of the crystal by migrating to the dislocation strain field, relatively small atoms residing in the compressive field while large atoms tend toward the tensile region. In this manner, strain energy is reduced and an impurity *atmosphere* is said to exist by the dislocation. If the impurity induces a shear strain, as found for some interstitials, it may interact with the shear strain field of a screw or mixed dislocation.

The same concepts apply to grain boundaries (or any strain inducing defect). However, the strain field due to a dislocation decreases inversely with distance from the dislocation line while a grain boundary strain field diminishes (at least) as distance squared. Hence, grain boundary segregation is expected to be highly localized. In fact,

X-ray diffraction measurements of grain boundary strain field thickness yield values on the order of ten angstroms.[38]

Defect Core Segregation

The above considerations suit well to describe impurity behavior in the region of strained though otherwise perfect material neighboring a defect. Such a segregation phenomenon has a continuum nature; hence the description as an impurity "atmosphere". Of essential interest is the **defect core** which, as commonly defined, consists of atoms strained beyond the limits of linear elastic theory or, from the present viewpoint, those atoms with major bonding distortions. Segregation in such material is likely to involve or be dominated by bonding effects. To describe segregation involving such atoms, a continuum approach is no longer appropriate. Rather, an atomistic view is clearly required.

For grain boundaries in particular, defect core segregation is an exceedingly complex though important problem for which little direct experimental data exists. As demonstrated in the case of silicon, defect cores contain a number of configurationally distinct interstitial and substitutional sites. Hence, a variety of possible sites for segregating atoms is expected, each with a unique binding energy. In addition, the types of available sites and their distribution is a function of the particular grain boundary in question. In principle, the solute atoms may interact and/or induce changes in the defect structure. Thermodynamic approaches to the problem of grain boundary segregation are unable to predict the details of such behavior since they average over the structural details of the boundary. This is no longer satisfactory since, as discussed, grain boundaries possess a variety of structures for which theoretical models are now

being developed (Chapter 3). However, a quantitatively accurate model for segregation likely awaits direct experimental observations.

The very few direct observations of atoms segregated at grain boundaries have all been in metals and yielded little information about correlations with grain boundary structure.[39] The only information with atomic resolution comes from Field Ion Microscopy studies.[40] This technique has rather severe specimen requirements in addition to being a surface technique and, as such, of uncertain correlation to the true grain boundary structure.

One might then ask if impurities at core sites are observable with HRTEM. Indeed, the present study's interest with such core atoms is two-fold: the interaction of impurities with defect cores is an exceedingly important fundamental and practical concern while it is also exactly such sites which are potentially experimentally accessible to HRTEM. Defects which may be imaged with HRTEM are invariant in one direction: in other words, the repeat distance in this direction is that of the parallel lattice vector. This is simply the planar spacing. Such is the case for pure tilt grain boundaries and straight dislocations. As a consequence to this, equivalent core atomic or interstitial sites will be found in each crystallographic plane. Filling all of a particular type of segregation site then leads to a column of impurity atoms with spacing identical to the parallel columns of matrix atoms. If the impurity is of sufficiently different Z from that of the solute, one might expect the impurity column to be detectable in an HRTEM image. With less than full saturation of segregation sites, detection becomes more problematical. In any event, no such experimental studies have been reported nor has the potential for detection with consideration of optimum experimental conditions been considered.

This subject is explored in detail with computer image simulation analysis in Chapter 7. For motivation and input for the image simulations, specific models for segregation in silicon dislocations and grain boundaries are discussed in the following section.

4.2. Segregation Models

Type III/V Dopants

First insight into the nature of segregation sites for dopants at defects in silicon, comes from consideration of amorphous semiconductors. As indicated previously, crystalline defects in silicon are expected to contain similar structural components. In other words, dislocations, grain boundaries, and amorphous material are likely to be structurally homologous. Each seems to consist of some eclipsed bonds, non-six-membered rings, unpaired electrons, and reconstructed bonds in the attempt to maintain tetrahedral coordination. Hence, it is safe to assume that the behavior of dopants in these and other crystalline defects will exhibit some fundamentally similar features. The goal here is to predict the structural (chemical) aspects of dopants in defect core regions. Though this subject has been lightly touched for dislocations and grain boundaries, there has been substantial research on amorphous material due to practical problems with controlled doping. This serves as a logical springboard.

Generally, only a small fraction of dopant introduced into an amorphous semiconductor acts as a donor/acceptor.[41] If a dopant atom resides in a substitutional site with tetrahedral bonding one expects it to behave electrically as in crystalline material. Mott[42] suggests that five-fold coordination may be achieved in amorphous silicon, allowing a pentavalent dopant (P, As, or Sb) to form five bonds, thus

becoming electically neutralized. Though no details are given, this suggestion may be rationalized by recourse to the chemistry of bonds. Examining the molecular forms encountered for the column V pentavalent elements when bonding with those in column VII (the monovalent elements F, Cl, Br, and I) one finds the natural occurence of both three- and five-fold coordination (e.g. PF_3, PF_5, PCl_3, PCl_5, PBr_3, and PBr_5). The three-fold form utilizes sp^2 hybrids in the formation of a planar molecule (see Appendix A), while the latter type employs sp^3d bonding usually in a trigonal bipyramidal configuration. Here, three equidistant bonds form a plane normal to the other two oppositely directed bonds. In the three-fold case, the two remaining valence electrons reside in the remaining p orbital. Note that boron, a trivalent dopant, only forms compounds of three-fold coordination.

Next, consider how this relates to observations on segregation of dopants at silicon grain boundaries and dislocations. Kamins[43] found that the resistivity of polysilicon recoverably varied inversely with annealing temperature. This was suggested to arise from dopant atoms segregating at the grain boundaries in an *electrically neutral* state. Additional work involving boron, phosphorus, and arsenic demonstrated a heat of segregation for the latter two of approximately 10 Kcal/mole, but no significant segregation for boron,[44] indicating the dominance of bonding effects. Their electrical measurements could not detect segregating dopant which was not neutralized, however, using more direct, non-electrical measurement techniques, Swaminathan, *et al.*[45] and Rose and Gronsky[1] found similar levels of segregation. The saturation level of dopant was somewhat less than one monolayer. This is as expected for segregation sites specific to the grain boundary core.

It appears then that the affinity of these impurities for defect cores lies in the alternative bonding coordination afforded by the defect structure. It is likely that unpaired electrons participate since any other possible site only offers tetrahedral coordination and is therefore probably unable to neutralize the dopant atom. This leaves two possibilities:

(1) a silicon atom possessing an unpaired electron is at a potential substitutional segregation site or,
(2) a silicon atom *neighboring* an atom with an unpaired electron is at a potential segregation site.

In case one, a dopant atom replaces a silicon atom and its unpaired sp^3 hybrid. This is feasible for both the trivalent and pentavalent dopants. For phosphorus and arsenic, this would leave two non-bonding valence electrons. In the second situation, the segregating atom forms a fifth bond involving the neighboring unpaired electron. This option is unavailable for boron: as noted though, boron apparently does not segregate at grain boundaries. It is then suggested that the preferred segregation site is that of case two.

Apparently, significant energy reduction only results by pairing the "broken bond" with a neighboring impurity. Though no attempt is made here to justify this on more fundamental grounds, research on swirl defects may also be interpreted as indicating a tendency for donor segregation at dislocations.[46] Here, A-swirls (dislocation loops) are observed to be suppressed by phosphorus, arsenic, and antimony but not boron or gallium, indicating segregation only of the former.

Lastly arises the question of how this applies to the dislocation and grain boundary models already considered. First, one notes that the grain boundaries employed in this thesis (or any tilt boundary obtainable for study) probably contain no unpaired

electrons. Therefore, they have none of the possible segregation sites considered above. This does not mean the segregation model is wrong, simply that in polycrystalline material, particularly the fine-grained polysilicon employed in the above mentioned studies, most grain boundaries will be of random orientation, containing unpaired electrons and exhibiting segregation. In support of this, Rose and Gronsky[1] observed negligible phosphorus segregation at a twin boundary (no unpaired electrons).

However, the <110> line direction dislocations produced during deformation do potentially contain unpaired electrons. Examination of the models employed in this study demonstrates that the 30° partial dislocation possesses an atomic configuration consistent with the above model for segregation. In an unreconstructed model (see fig. 2-7 and Appendix A), one finds that the unpaired electron extends approximately in the direction of a nearby atom at the end of the stacking fault, roughly a bonds length away. Figure 4-1 depicts this with a <111> projection of the two atomic planes immediately above and below the stacking fault. This second atom could then be replaced by a type V impurity and form a fifth bond with the unpaired electron of its neighbor. Placing a metal connector with a trigonal bipyramidal bond configuration at the model's hypothetical segregation site permits five bonds with nominal strain. The model of fig. 4-2 is therefore taken as a likely representative of dopant segregation in silicon dislocations and grain boundaries.

Interstitial Impurities

The ever present, and generally undesirable, metallic impurities may also exhibit segregation. These impurities are generally interstitial: their segregation potential may

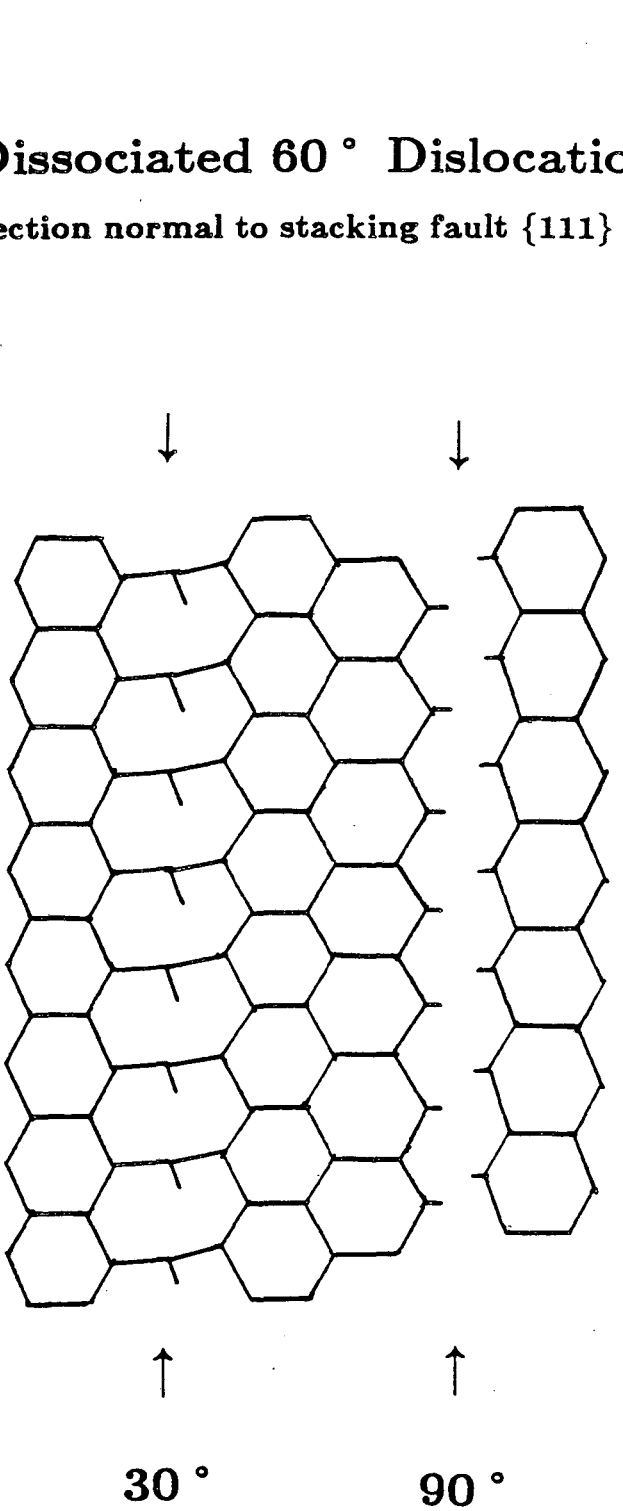

Fig. 4-1 Schematic view of a dissociated 60° dislocation, looking down on the stacking fault plane. Geometrically unpaired valence electrons in the partial dislocation cores are indicated by broken segments.

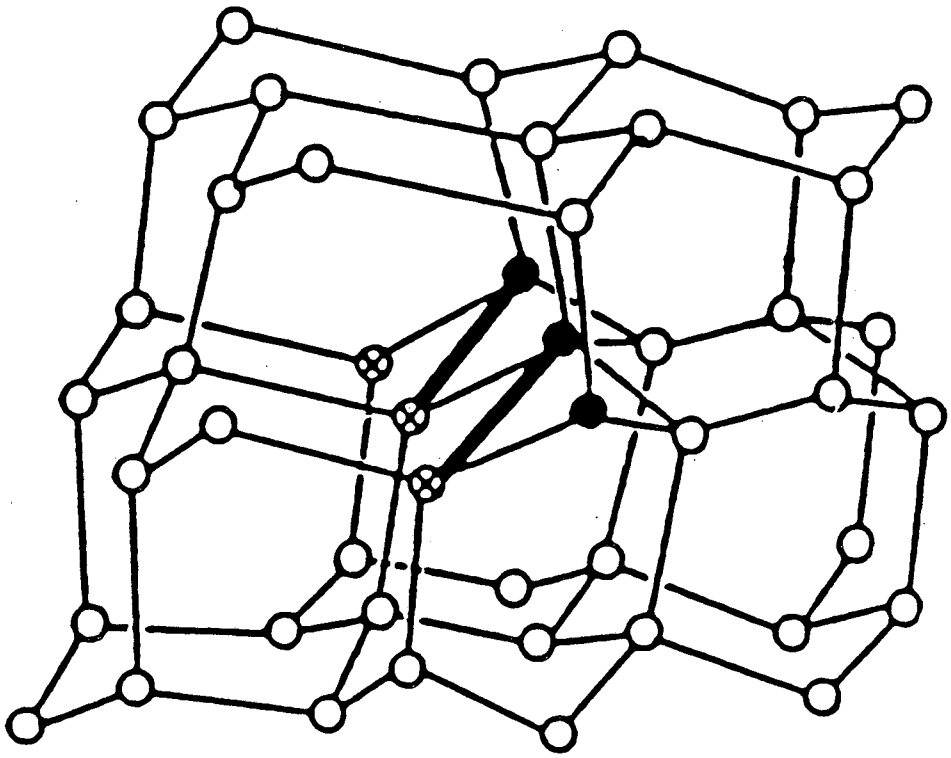

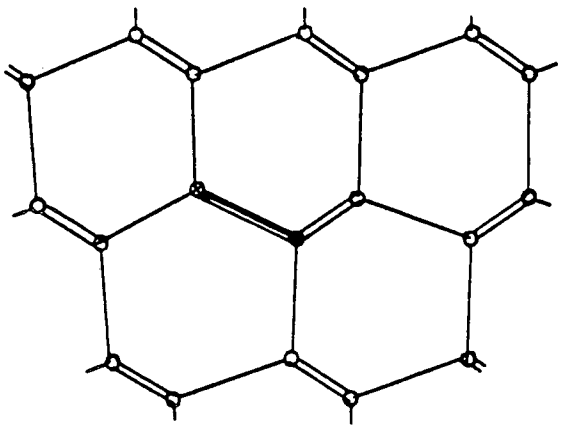

Fig. 4-2 The 30° partial dislocation donor atom segregation model (the bottom figure is a projection of the top, though flipped about a horizontal axis). Atoms at the end of the half-plane are marked with ×'s while segregated atoms are filled. The fifth bond of the donor atom accomodating the potentially unpaired valence electron of a core atom is indicated with a bold line. XBL 855-2557

be evaluated by searching models for larger than normal interstices. To look for potential interstitial segregation sites, spherical balloons were placed in the plastic models, testing for locations significantly larger than normal interstices. Naturally, defects offer interstitial sites of different configuration from that of the matrix. In particular, large sites are available at dislocation cores and at 7-membered rings. In projection, this is most readily visible for the $\Sigma 9$ grain boundary. In fig. 4-3, "interstitials" are observed to reside in the large tunnels in the grain boundary core, as intuitively expected. The center of the interstice is indicated in the bottom projection.

The situation is somewhat more complicated for $<100>$ tilt grain boundaries. For both 45° and edge dislocation models, two geometrically distinguishable interstitial sites are available (figures 4-4 and 4-5). Also, the centers of these sites are colinear with a $<100>$ column of silicon atoms. There are two each of each type of site for the edge dislocation leading to four interstitial locations per repeat length of the dislocation (fig. 4-4) while the 45° core has one pair of equivalent sites or three total (fig. 4-5).

The same approach is applied to the dissociated 60° dislocation. Models depicting all possible sites are given in fig. 4-6 and, for clarity, repeated schematically in fig. 4-7. In both the unreconstructed and reconstructed 30° partials, there are two interstitial sites below the dislocation half-plane while the reconstructed partial also has two above. The 90° partial has a single site while all tunnels adjacent to the stacking fault are also potential sites (one is given as example). Note that this is essentially just Suzuki segregation.

These interstices are roughly 10% larger than matrix sites. Though specific values are irrelavent to this study, the relative sizes at each defect are (in decreasing

Σ9

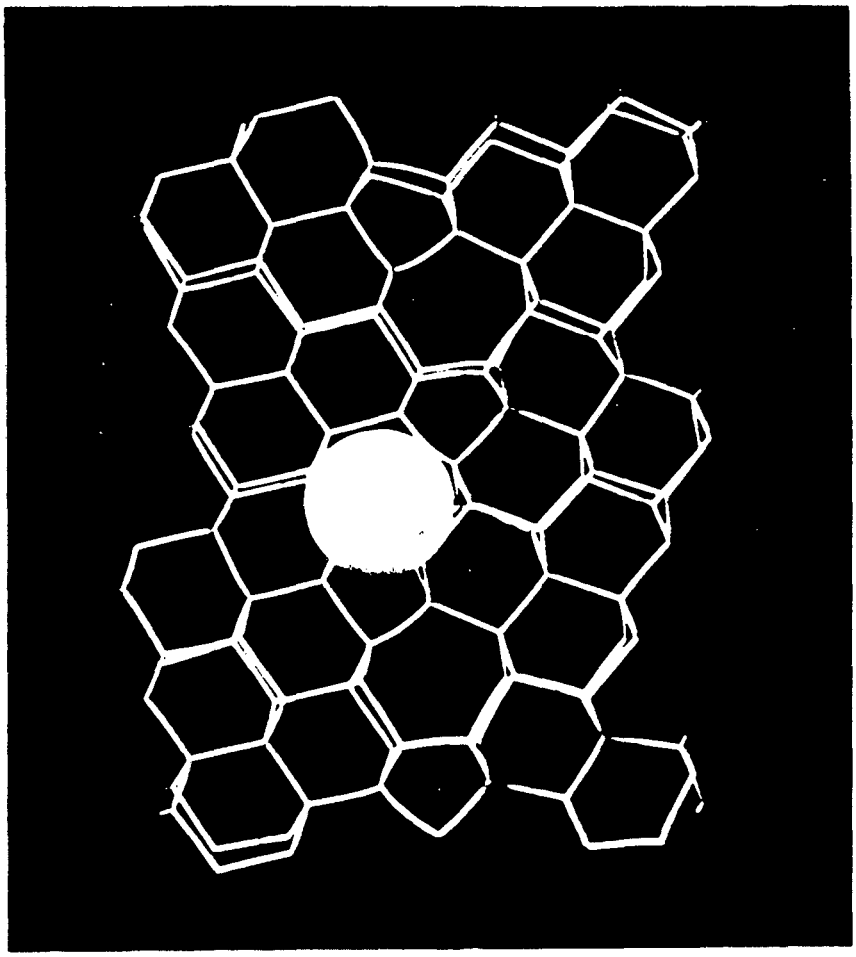

Fig. 4-3 The Σ9 {221} grain boundary interstitial segregation model (above). The center of the interstitial "atom" is indicated below. In projection, it lies within the 7-membered ring. XBB 855-3688

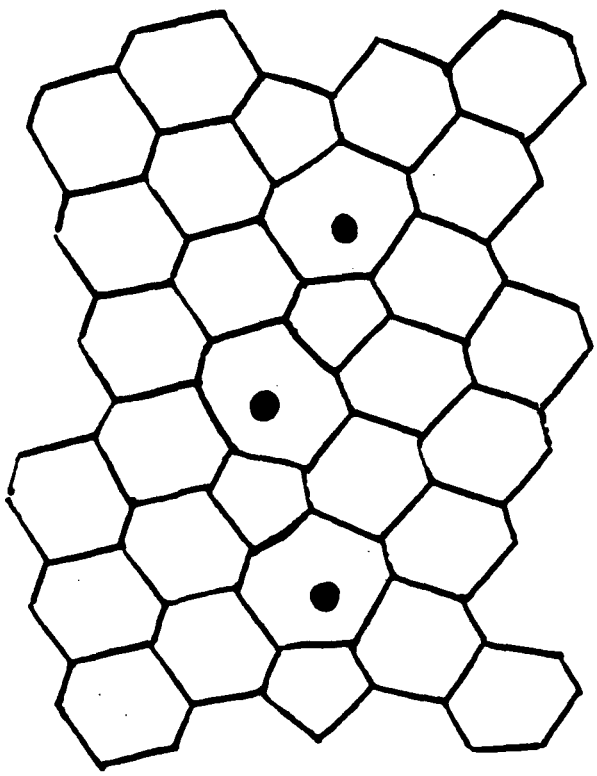

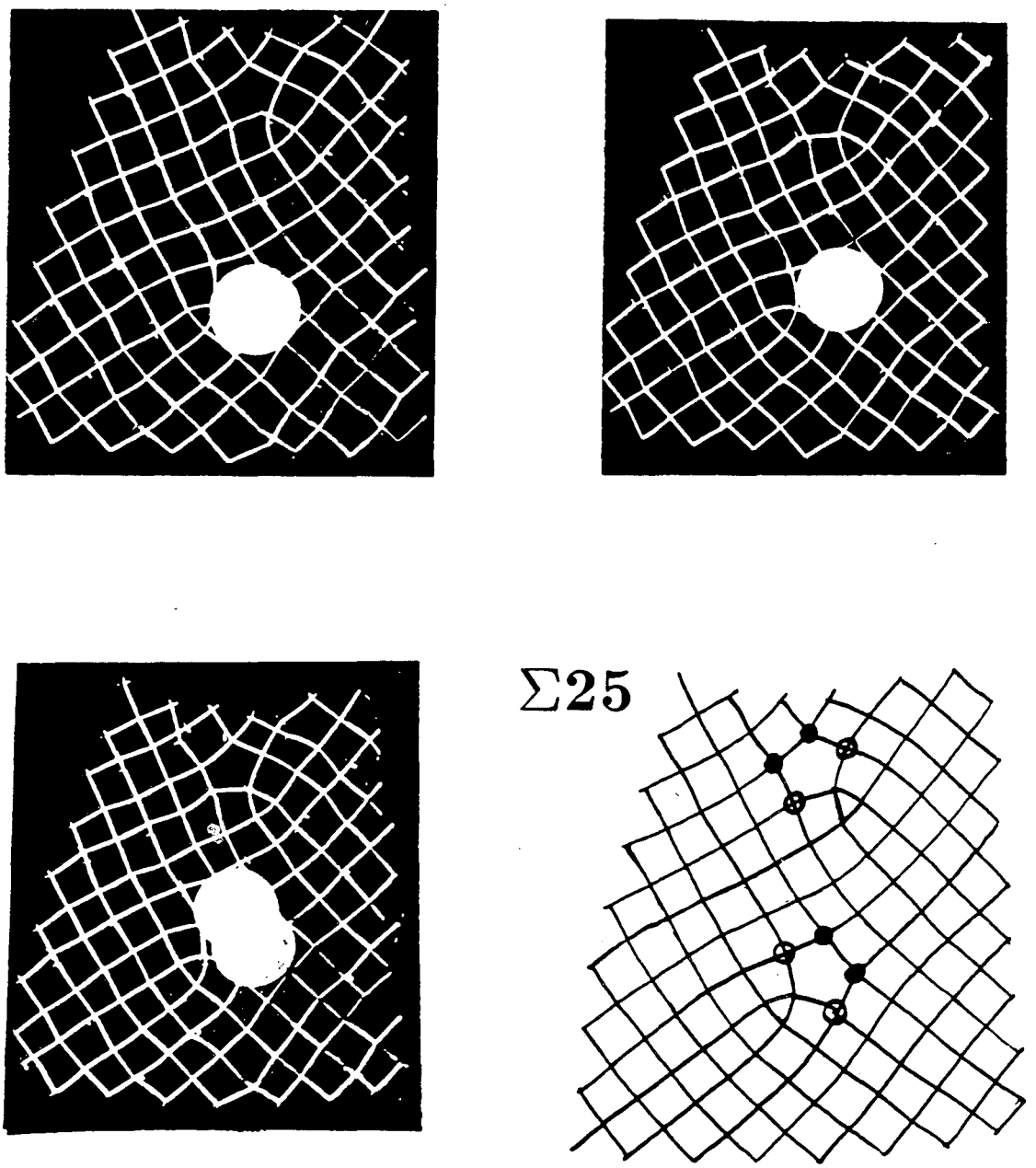

Fig. 4-4 The top figures give the two distinct interstitial sites for a <100> line direction edge dislocation (here, in a Σ25 grain boundary). Their centers are indicated in the lower right figure; open circles correspond to the upper left figure, filled circles to the upper right. The lower left figure shows the two filled circle sites occupied. In projection, any combination of the four interstitial sites may be filled. XBL 855-2387

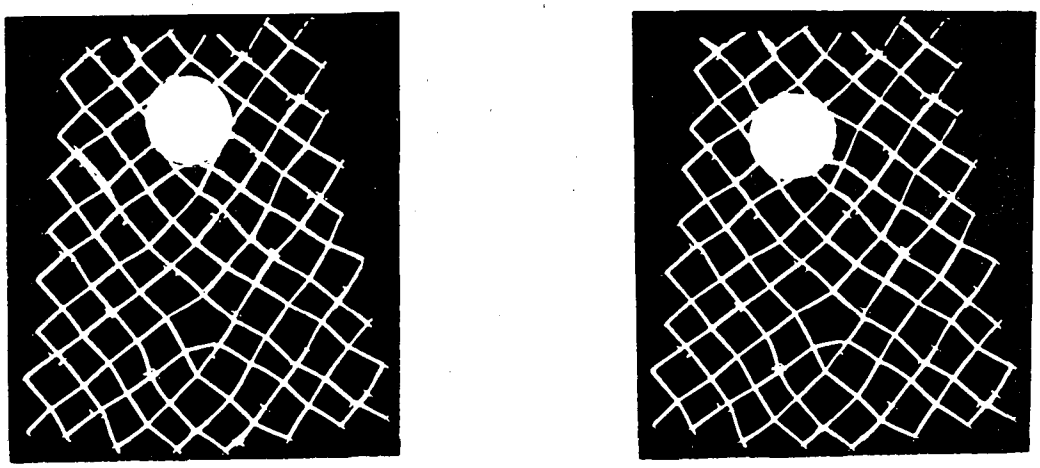

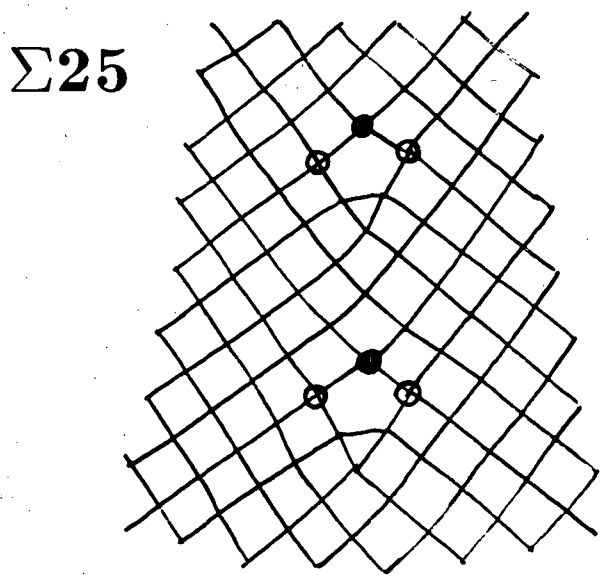

Fig. 4-5 Interstitial sites of the 45 ° dislocation (in a Σ25 grain boundary). The top left figure gives an open circle site, the top right a filled circle site. Site centers appear in the lower figure. XBL 855-2388

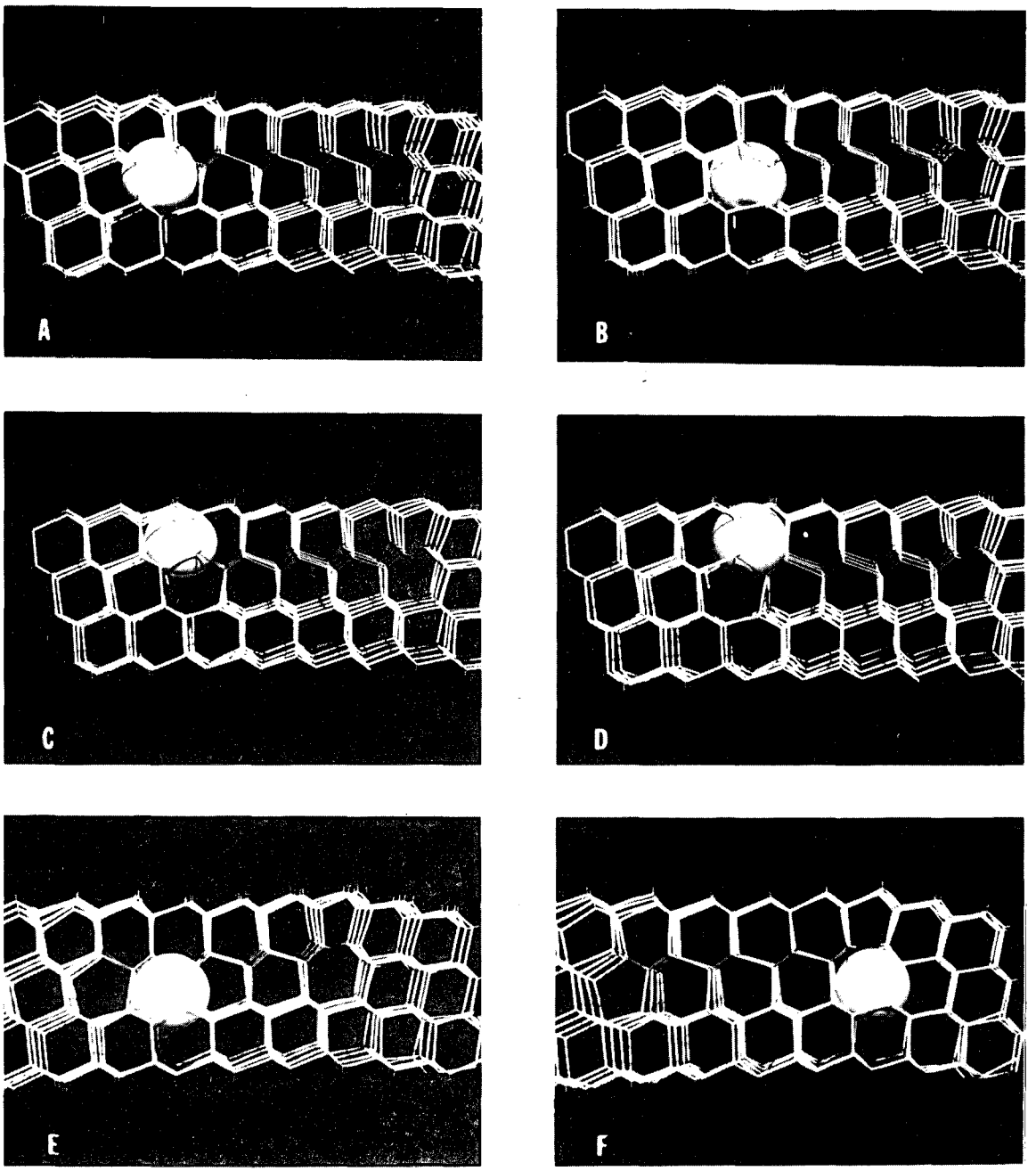

Fig. 4-6 Photographs of split 60° dislocation model with an interstitial balloon, giving hypothetical segregation sites. The 30° dislocation core is on the left, 90° dislocation on the right. Sites in A, B, C, and D are in the 30° core, E is by the stacking fault, and F is in the 90° core. Interstitial centers are schematically shown in fig. 4-7. XBB 851-697-A

Interstitial Segregation Sites in the Dissociated 60 ° Dislocation

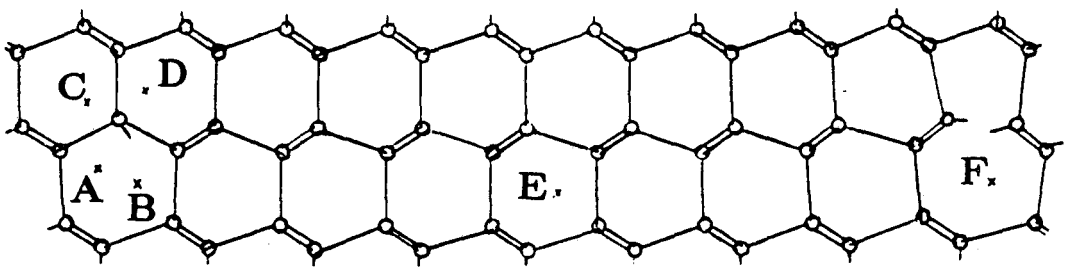

Fig. 4-7 Potential interstitial segregation sites in the 60 ° dislocation. Labelling corresponds to models in fig. 4-6. XBL 855-2556

order); unreconstructed 30° partial- A/B (same); reconstructed- A, B, C/D; edge dislocation- A/B; 45° dislocation- A, B.

CHAPTER 5

HRTEM

All transmission electron microscopy may be categorized as utilizing diffraction (amplitude) contrast or phase contrast. Diffraction contrast images generally utilize the objective aperture to exclude all but the transmitted or a single diffracted beam. Contrast in the image arises from regions with differing absorption or elastic scattering due to orientation changes or the presence of a defect.

In phase contrast imaging, two or more beams are allowed to interfere to form an image. With two or a row of beams contributing, a *fringe* pattern is obtained while three or more non-colinear beams can produce a *lattice image*. The desired spacings must be within the resolution limit of the instrument, that is, the lens system must preserve the coherence of the image forming beams. This is the technique of HRTEM. This term implies the use of a microscope which has been optimized for resolution capability, e.g. via specimen stage and objective lens design and electronic and mechanical stability.

The first section below gives a general outline of phase contrast imaging plus some salient concepts useful for the interpretation of HRTEM micrographs. The following section discusses practical aspects of concern while working on the microscope. Lastly, specimen preparation details relevant to this thesis are given.

5.1. Theory

The definitive feature of HRTEM is perhaps the two-dimensional nature of the information it provides. While a specimen may be tilted in conventional TEM to obtain three dimensional information, one is generally limited with HRTEM to observations of projected atomic structure along low index poles with planar spacings within the resolution limits of the microscope. For this reason, one would like to directly interpret an HRTEM image as a simple map of the projected structure (crystal potential). However, such an interpretation is only possible for a very narrow range of instrumental parameters and specimen thickness. This situation is well described theoretically and so provides the starting point for the following discussion.

A useful approximation in the description of the interaction of the electon beam with the specimen is found in the assumption of phase changes only, that is, a phase object. An incident wavefunction ψ_o incurrs a phase change proportional to the crystal potential

$$\psi = \psi_o \, e^{-i \sigma t \, \phi_p (x,y)}$$

where σ is the electron interaction parameter, t the specimen thickness, and ϕ_p the projected potential.

By additionally assuming a weak interaction, one obtains the Weak Phase Object (WPO) approximation

$$\psi \approx \psi_o \left(1 - i \sigma t \, \phi_p (x,y) \right) .$$

Application of this requires that

$$t \ll \frac{1}{\sigma \phi_p} .$$

Hence, the required thickness decreases with increasing atomic number, though it is less than 100Å for all materials of interest. The above form of the exit wavefunction has a straightforward physical interpretation. The dominant transmitted wave is approximated by ψ_o (unit amplitude) while to this is added a relatively weak scattered wave of amplitude $\sigma t \, \phi_p(x,y)$ and phase $\frac{-\pi}{2}$ relative to the unscattered portion, as it is purely complex. For such thicknesses and assuming an ideal Scherzer lens, i.e. one that imposes a phase change of $\frac{-\pi}{2}$ on all diffracted beams, a linear relationship between image intensity and projected crystal potential is obtained

$$I(x,y) = 1 - 2\sigma t \, \phi_p(x,y) .$$

The effect of the objective lens must then be considered. In an ideal lens, diffracted beams undergo a phase shift which is strictly a function of their angle from the optic axis. Assuming the transmitted beam is aligned along the optic axis, this angle is $2\theta_B$, twice the Bragg angle of the beam. Allowing for spherical abberation and a lens defocus, Δf the phase change is

$$\chi = \pi \lambda g^2 \left(\tfrac{1}{2} \lambda^2 c_s \, g^2 - \Delta f \right)$$

where g is the magnitude of the reciprocal lattice vector, c_s is the sperical abberation coefficient of the lens, and the other terms have the usual meaning. By definition, Δf is the distance from the specimen exit plane to the lens object plane. The defocus is taken as negative for an underfocused lens (obtained by reducing the lens current).

The effect of the objective lens then is to multiply each diffracted beam by the phase factor $e^{i\chi(g)}$. Under the WPO approximation, the transmitted beam ($\chi = 0$) and the real components of the diffracted beams interfere to form the image, i.e. a diffracted beam's contribution is proportional to $\sin\chi$. For negative χ, the diffracted beams interfere destructively with the transmitted beams, producing "black" atom images while a positive χ leads to "white" atoms.

It is common for one to plot a linear Contrast Transfer Function (CTF) to describe the lens action, that is, a plot of $\sin\chi$ versus g. For a WPO, the largest number of beams will contribute to the image by maximizing the portion of the CTF where $\sin\chi = 1$ or close to it. Requiring that $\chi \leq \frac{-1}{\sqrt{2}}$ leads to the Scherzer defocus value

$$\Delta f_{Scherzer} = 1.2\,(c_s\,\lambda)^{\frac{1}{2}}\,.$$

The first zero crossover gives the Scherzer resolution limit

$$d_{Scherzer} = .7\;c_s^{\frac{1}{4}}\lambda^{\frac{3}{4}}\,.$$

This is the highest resolution at which one may hope to directly interpret an HRTEM image. Decreasing the defocus value leads to higher order passbands at

$$\Delta f_n = \left(\tfrac{1}{2}c_s\,\lambda(8n\,+3)\right)^{\frac{1}{2}}$$

which may be employed to resolve finer detail, $n = 0$ giving the Scherzer passband. Since higher passbands exclude some lower angle scattering, their direct interpretation is impossible, particularly in the case of defect imaging for which diffuse scattering possesses important image information. In addition, electronic instabilities effectively

damp higher frequencies, limiting the number of useful passbands. This damping limit is usually called the information resolution limit.

As seen above, proper selection of defocus is employed to optimize resolution. While working at the microscope, one uses the *minimum contrast* condition as a reference point. At this defocus setting, diffracted beams are as close to a $\frac{-\pi}{2}$ total phase shift as possible, minimizing interference with the transmitted beam: in other words, $\sin\chi$ is close to zero over a maximized range. This is given by

$$\Delta f_{\text{min}} = -.44\,(C_s\,\lambda)^{\frac{1}{2}}$$

which is about one third the Scherzer defocus value.

The above concepts are commonplace in discussions of HRTEM results even though the WPO approximation is usually invalid (it is quite difficult to produce a good specimen of less than 100Å thickness). However, they provide an acceptable starting point for selecting proper imaging conditions and for micrograph interpretation. Thicker samples are acceptable if one does not require detailed information about defect atomic positions, e.g. applications in phase identification, interfacial morphology, etc. Proper evaluation of defect atomic positions or even configurations requires concurrent image simulations using hypothetical models until good matching with experimental images is achieved. This subject is discussed in the following chapter.

5.2. Practical Aspects

Though a good theoretical background is required for the interpretation of HRTEM micrographs, much practical experience at the microscope is necessary before

interpretable images may be obtained with any regularity. Key experimental concerns are outlined below.

Suitable specimens are essential; preferably flat, clean, gradually decreasing to zero thickness at an amorphous edge. Microscope alignment is critical. The filament tilt, heating, and bias must be adjusted for a suitable compromise between brightness and coherence. The condenser aperture is chosen to allow sufficient illumination while limiting beam divergence. Alignment of the beam along the optic axis is always a concern since deviations of as little as 0.1°, presently unmeasurable, may strongly affect the image. Ojective lens astigmatism is corrected by observing the "granular" appearance of an amorphous or contaminated edge and obtaining a maximum definition/minimum contrast condition. Finally, and likely the most difficult particularly with warped specimens, is correction of specimen tilt. Normally, Kikuchi bands or convergent beam patterns are employed for precise tilt adjustment, however any portion of specimen evincing such effects is too thick for HRTEM imaging. The thin edge is usually warped a bit so one must use a selected area aperture, tilting the specimen until the intensity of diffacted spots appears to be balanced about the transmitted beam. This requires a certain amount of guess work, particularly since the selected area aperture includes scattering from areas in addition to that of interest. These concerns apply most strongly to imaging of defects where structural information is required. Perfect crystals allow somewhat more leeway in selecting an area suitable for imaging.

5.3. Silicon Specimen Preparation

Single crystal silicon readily provides excellent microscope specimens using HF/HNO_3 based etching solutions. Since defects generally etch preferentially to some degree, ion milling was usually employed as a final preparation step. Wafers were cut with an ultrasonic drill into microscope standard 2.3 or 3 *mm* discs. These were hand polished to approximately 125μ, then etched in 1HF:2Acetic Acid:$3HNO_3$ to a thickness of about 10 or 20μ, and finally ion-milled. This gave the best specimens in addition to saving milling time. The etching step can be replaced with use of a specimen dimpler.

CHAPTER 6

HRTEM Image Simulation

As discussed in the previous chapter, HRTEM micrographs have a direct correlation to the projected structure of the specimen for only an extremely narrow range of experimental conditions. In particular, interpretation of images of defects and complex structures such as found in ceramics generally requires matching of images with companion computed image simulations for reliable interpretation. This chapter gives the essential background on calculated lattice image simulations required for consideration of subsequent chapters. Section 1 outlines the history and basic theoretical foundations of this technique while Sec. 2 gives details concerning the programs employed in this study.

6.1. General Principles

At the heart of any image simulation calculation is the treatment of the beam/specimen interaction. Current image simulation calculations are usually based on the physical optics theory of Cowley and Moodie[47],[48],[49] for the dynamical calculation of diffracted amplitudes. This is commonly referred to as the *multislice method* since the amplitude and phase at the exit surface of a crystalline specimen is found by treating the crystal as consisting of N slices of thickness Δz so that the total thickness $t = N\Delta z$. The crystal potential of each slice is then replaced by its two dimensional projected potential, an adequate approximation for sufficiently small Z or Δz. The effect of the first slice on the incident wavefunction is calculated; the resulting wavefunction is then propagated through free space to the next slice. This is repeated

until the desired thickness is achieved. For large unit cells and thin specimens, this is currently the most efficient means for a high voltage electron dynamical interaction calculation.

Though this work, published in the late 1950's, provided the essential theoretical foundation for the calculation of HRTEM images, it was not until the early 1970's that such work began.[50],[51] This was partially a consequence of limitations on experimental work as the required microscopes were being developed, but to a greater extent due to the computational requirements, i.e. the necessary computers for the calculations did not exist. However, continuing advances in computing speed and cost plus the development of more efficient computing algorithms today permits calculations on the order of seconds that just a few years ago would have required hours (and prohibitive cost).

Complete calculation of an image has two distinct components: calculation of the beam interaction with the specimen, as with the above approach, followed by calculation of the effects of the microscope lenses. The theory on which these calculations are based is outlined below (for more detail see references [52] and [53]).

Figure 6-1 serves as a guide in the following discussion. The calculation usually commences with a plane wave of unit intensity incident on the specimen. The electron wave function must then be calculated at three locations within the electron microscope; at the specimen exit surface, at the back focal plane (BFP), and at the image plane. Only the objective lens is considered since the subsequent lenses simply serve to further magnify the image for the final viewing screen. The particular microscope does not enter the beam/specimen calculation except in the form of the beam voltage. The influence of the objective aperture, focusing error (defocus value),

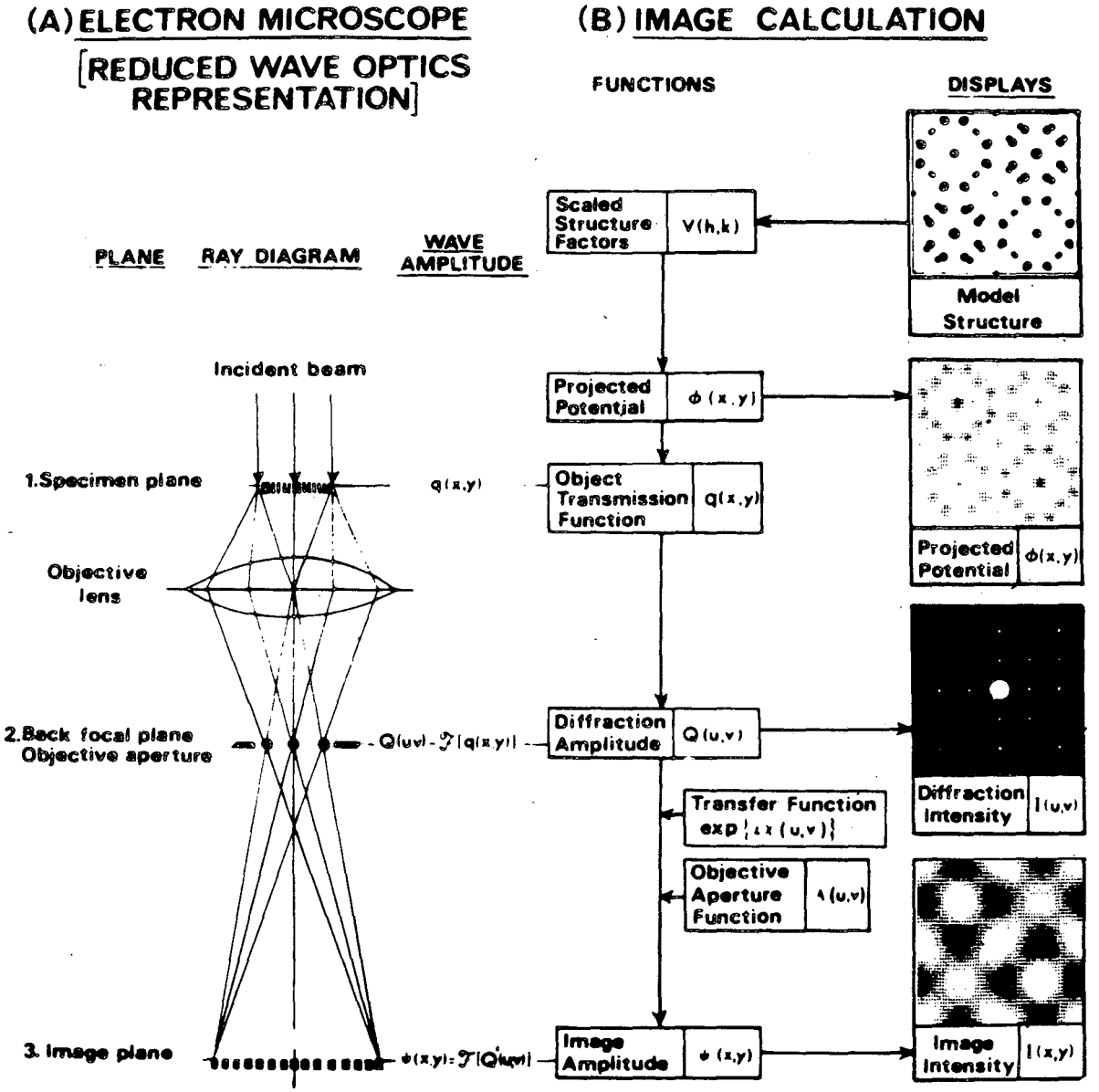

Fig. 6-1 This figure serves as a pictoral guide for the discussion of the various steps in the calculation of a HRTEM image (courtesy of M.A. O'Keefe.) XBL 8312-4698

spherical aberration, and other instrumental effects are applied at the BFP.

The calculation may be divided into three salient steps; evaluation of the scattering due to a single slice of the specimen, performing the iterative multislice, and lastly taking the exit surface wavefunction as object for the imaging lens with inclusion of phase and amplitude changes due to instrumental parameters.

First, a "super" unit cell - generally larger than the crystal unit cell - is selected with specification of atomic species and coordinates. The thickness of the unit cell is generally that of the lattice vector magnitude in the beam direction. It was tacitly assumed in the previous section that the crystal slices could vary freely in the x-y plane. Such is clearly unsuitable for computer calculations where a periodic structure is generally required due to the use of Fourier transforms. Hence, the x-y dimensions of the cell define the repeat distance for the calculation. Using the electron scattering factors, f_j (equivalent to the Fourier transform of the potential distribution of the atom), the structure factors for the reciprocal lattice zone normal to the beam direction are given by

$$V(\mathbf{k}) = \frac{h^2}{2\pi m_e e V_c} \sum_j f_j \mid \mathbf{k} \mid \exp(-2\pi i \, \mathbf{k} \cdot \mathbf{r}_j)$$

where V_c is the unit cell volume, j identifies the atoms in the unit cell, and $\mathbf{k}$ identifies reciprocal lattice sites, $\mathbf{k} \equiv [u, v]$. Taking the Fourier transform of $V(\mathbf{k})$ provides the *projected* potential of the unit cell, $\phi_p(x, y)$. For a phase object (no absorption), the *transmission function* of the slice is then

$$q(x, y) = \exp\left(i \sigma \, \phi_p(x, y) \, \Delta z \right)$$

where $\sigma = 2\pi m e \lambda / h^2$ is the electron interaction parameter for the beam voltage.

This is also referred to as the *phase grating*, an approximation appropriate to small-angle scattering as obtained here with high voltage electrons. A transmission function is evaluated for each different type of slice (often, all slices are identical).

The output of a particular slice is found by convolution of the incident wavefield with the transmission function. With a unitary incident wave, the output of the first slice is simply $q_1(x,y)$. This provides the initial input to the multislice calculation. With iteration, the exit wavefield of the n^{th} slice is;

$$f_n(x,y) = \left\{ f_{n-1}(x,y) \ * \ p(x,y) \right\} \cdot q_n(x,y)$$

where * represents convolution and $p_n(x,y)$ is the free space propagator which transforms the exit wavefunction of one slice to the incident wavefield for the next slice. With the small-angle approximation, the propagator has the form

$$p(x,y) = \exp\left(\frac{-ikr^2}{2\,\Delta z} \right)$$

where $r^2 = (x^2+y^2)$ and $k = \frac{2\sin\theta}{\lambda} = (u^2+v^2)^{\frac{1}{2}}$. The subscript (n) is dropped with the assumption of equal spacing between slices. The propagator originates in Huygen's Principle in which it is assumed that the waveform incident on slice n is found by summing over infinite point sources at the exit surface of slice $n-1$.

Fourier transforming the exit wavefield yields the diffracted wavefield, i.e. the amplitude/intensity at the BFP, $F(u,v)$. In fact, the multislice is typically carried out in reciprocal space, leading directly to $F(u,v)$

$$F_n(u,v) = \left\{ F_{n-1}(u,v) \cdot P(u,v) \right\} \ * \ Q_n(u,v)$$

where the propagator now has the form

$$P(u,v) = \exp\Big(\pi i\, \varsigma(u,v)\, \Delta z\Big)\,,$$

$\varsigma(u,v) = \lambda k^2$ being the z-component of the excitation error for the reflection $\mathbf{k} = (u,v)$ (i.e. distance to the Ewald sphere in the beam direction). Note here that the phase grating approximation treats the Ewald sphere as being flat. It is in the propagator function that its true curvature is taken into account.

With $F(u,v)$, instrumental effects must lastly be accounted for to obtain the wavefunction at the object plane, $\psi(x,y)$. The previous chapter gave the phase changes due to spherical aberration (C_s) and defocus (Δf)

$$\chi(u,v) = \pi\lambda k^2 \left\{ \tfrac{1}{2}\lambda^2 C_s\, k^2 - \Delta f \right\}.$$

A more conceptual approach to the effect of defocus is found by noting that the object plane generally does not coincide with the exit surface of the specimen, depending on the focus (objective current) setting. The required wavefield at the object plane is found by applying a final propagator for the distance Δf from the exit surface

$$P_{\Delta f}(u,v) = \exp(\pi i\, \Delta f\, \lambda k^2)$$

which is identical to the above result. Including an objective aperture, $A(u,v)$, equal to one within the selected aperture radius and zero beyond, the modified BFP wavefield becomes;

$$^{m}F(u,v) = F(u,v)\, A(u,v)\, e^{-i\chi(u,v)}\,.$$

Next, aberrations due to deviations from an incident ideal plane wave must be taken into account. The real electron beam has both a small energy spread, leading to

chromatic aberration, and a convergence (in the usual jargon called the divergence). The energy spread produces an approximately Gaussian spread in the location of focus (half-width roughly 100-200 Å) while the divergence leads to image formation over a range of incident angles (half-angle on the order of $1mR$). Both effectively produce a superposition of images, limiting resolution. It has been demonstrated that this may be accounted for by multiplication with two damping functions[54],[55] again in the BFP. Their effective apertures are generally smaller than the objective aperture (the objective aperature serves to improve image contrast by eliminating some background noise due to incoherent higher order scattering.)

Including the effects of high voltage and lens current ripple, the spread in defocus value due to chromatic aberration may be estimated by

$$\Delta = C_c \left\{ \frac{\sigma^2(V)}{V^2} + \frac{4\sigma^2(I)}{I^2} + \frac{\sigma^2(E)}{E^2} \right\}^{\frac{1}{2}}$$

where C_c is the chromatic aberration coefficient, V the beam voltage, I the objective lens current, E the thermal energy of electrons emitted from the filament, and σ^2 the variance of these quantities. Usually, Δ is employed as the half-width in a Guassian damping function

$$A_{C_c}(u,v) = \exp\left\{ -\frac{\pi}{2} \left[\pi \Delta^2 \frac{k^2 \lambda}{4} \right]^2 \right\}.$$

Damping due to divergence is generally expressed similarly or with a Bessel function. Though these approximations are derived under the assumption of a dominant transmitted beam, they have been found to give good matching with micrographs, even for thicknesses with strong diffracted beams.

Lastly, the image intensities are obtained by Fourier transforming the fully modified BFP wavefield to obtain the image plane wavefunction, $\psi(x,y)$, which gives the image intensities by squaring

$$I(x,y) = \psi(x,y) \cdot \psi^*(x,y)$$

i.e. the simulated image.

6.2. The ASU Multislice Programs

The image simulation programs employed in this thesis were developed at Arizona State University[56] and based on the Ph.D theses of Fejes[57], O'Keefe[58], and Skarnulis[59]. They have been adapted to run on the LBL Control Data Corp. 7600 machine by R. Kilaas. Though these programs are now a few years behind the state of the art, they sufficed for the necessary calculations. Currently, a dedicated HRTEM image simulation computer system is being installed at the National Center for Electron Microscopy which will permit more sophisticated calculations in the near future.

The computation is divided into four programs - FOCOEFF, PHASGRATE, MULTISLICE, and IMAGER - each using the output of the previous program plus its own input file. Figure 6-2 serves as a guide in the following discussion.

The simulation cell dimensions (A, B, and C), atom positions, and species are required as input to FOCOEFF. Assuming one has a model for the crystal or defect in question, proper selection of the unit cell is essential. For a perfect crystal, one simply selects some multiple of the crystal unit cell parameters in the x and y directions respectively for A and B. For a defect, a unit cell containing the defect is defined: in effect, the programs calculate an image for a periodic array of identical defects, the so

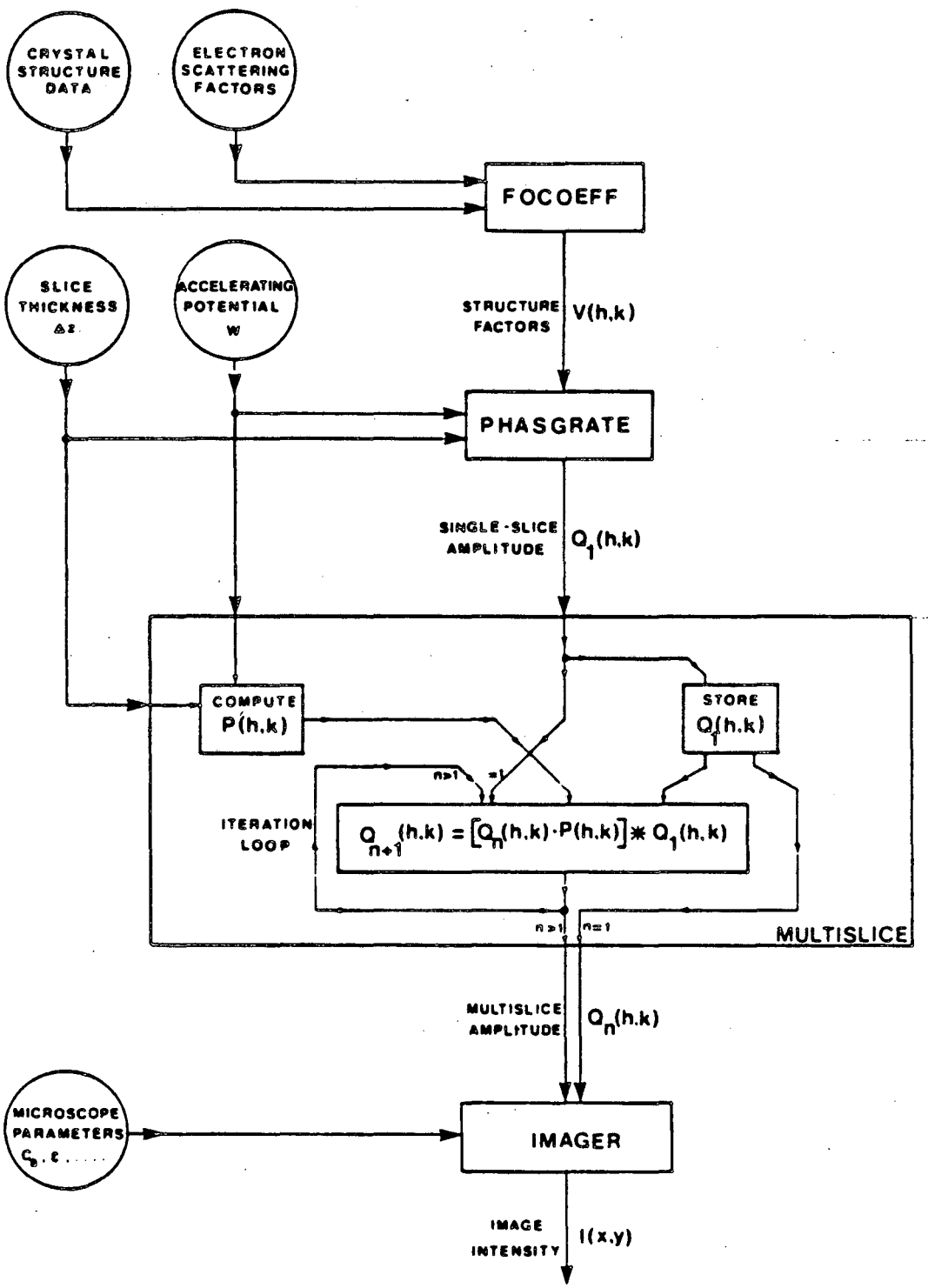

Fig. 6-2 This figure gives a flow chart for the computer calculation of HRTEM images. Circles give input files while rectangles indicate basic steps of the calculation. Arrows give the flow of data (courtesy of M.A. O'Keefe.)

called *periodic extension* method. The use of Fourier transforms also requires that the unit cell be smoothly varying at the boundaries. However, if this is impossible (as for grain boundaries), the cell may be made of sufficient size so as to isolate the defect from the anomalous image effects in the vicinity of the cell boundary.

Balanced against this is a computational limitation on cell size. The ASU programs utilize arrays with dimensions of 128x128 which must provide suffcient sampling of the real space phase grating. Materials of large and/or rapidly varying potential require a finer phase grating sampling interval. Given the array size constraint, this shrinks the allowable cell size with increasing atomic number. This is readily apparent from a reciprocal space viewpoint. Materials of higher atomic number scatter more strongly with relatively more scattering going to higher angles, i.e. further out in reciprocal space. To include all significantly excited beams, one generally needs to sample reciprocal lattice points to about 4Å^{-1}. This value is readily estimated from an experimental diffraction pattern corresponding to the simulation conditions. With a 128x128 array sampling four quadrants in the u-v plane, this leads to a minimum point spacing of $4\text{Å}^{-1}/64 = .0625\text{Å}^{-1}$. The inverse of this gives the maximum cell size of the input model, 16Å, which is a rather severe limitation when modeling large defects. Fortunately, sampling to 2Å^{-1} suffices for silicon (Z=14) allowing a $32\text{Å} \times 32\text{Å}$ cell size.

A computational unit cell of dimensions larger than the crystal lattice parameters thus leads to a reciprocal lattice containing points between the usual perfect crystal Bragg spots. Physically, these reciprocal lattice sites serve to account for the diffuse scattering that arises from a defect in crystalline material.

Lastly, the phase grating approximation generally limits slice thickness (unit cell C dimension) to less than 4Å, though for silicon 5Å is acceptable. Thus for <100> projections, the silicon FCC unit cell length of 5.4282Å may be taken as the slice thickness.

The PHASGRATE program runs next using the output of the above program plus an additional input file whose primary function is to specify the beam voltage. The reciprocal space phase grating is calculated as output. As discussed earlier, this is equivalent to the scattering due to a single slice. This program is run once for each different type of slice such as encountered when modeling materials with large unit cells (e.g. minerals) or when including an isolated defect in the crystal (e.g. an interstitial impurity).

This output file(s) is now fed to MULTISLICE which performs the iterative calculation with an additional input file specifying the correct order of the input phase gratings.

Output from thicknesses of interest are saved for final input to IMAGER which applies the effects of the various microscope parameters (Δf , C_s , divergence, objective aperture size, etc.) in the calculation of image intensities. The ASU programs use overprinting halftone routines to dispose the simulated images. Additional features were added for this thesis to take advantage of the graphics capabilities of the Varian Plotter at the LBL Computer Center.

CHAPTER 7

Imaging Impurities in Silicon

It is hoped that HRTEM will some day prove to be a powerful tool for the detection of differing impurity species segregated at crystalline defects. Virtually no work has been done in this area due to experimental difficulties and the lack of a thorough theoretical foundation.

This chapter describes results obtained with systematic image simulations investigating the feasibility and optimum conditions for observing impurities at silicon defects. The first section provides a foundation through an analysis of an impurity column in an otherwise perfect silicon crystal. The second section extends these results to substitutional impurities at a 30° dislocation and interstitial impurities in a $\Sigma 9$ grain boundary.

7.1. Substitutional Impurity Columns

To provide a basis for discussion of imaging of impurities at defects and to reduce computing costs through use of a smaller calculational unit cell, systematic calculations were first performed for substitutional impurity columns in an otherwise perfect <110> oriented silicon crystal.

The unit cell employed for calculations is depicted in fig. 7-1: it consists of two cubic unit cells in height and width. An impurity atom is situated at the center of the cell as indicated. A complete sample is obtained by interposing slices containing the required impurity type with slices of pure silicon. In this manner, a column containing

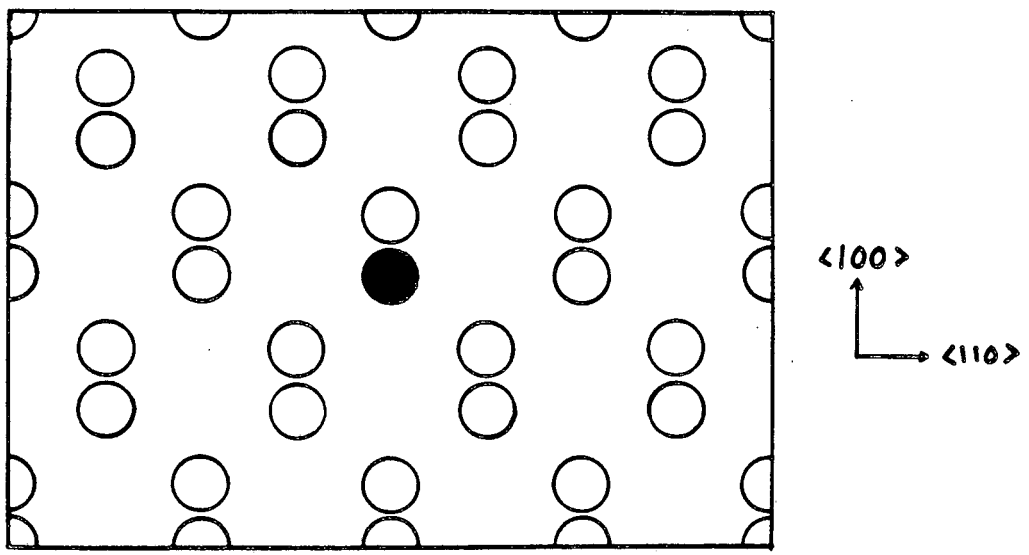

Fig. 7-1 Calculational unit cell for a <110> slice with a substitutional impurity (in black). The width is $2\sqrt{2}a$, height is $2a$.

impurity atoms is built up in which the impurity atoms may be substituted for any silicon atoms in the column. The specific concentrations studied and their modeling are given in Table 7-1.

The phase gratings were calculated with 2091 coefficients (to $2Å^{-1}$ in reciprocal space) while 484 beams ($.957Å^{-1}$) were included in the multislice calculations. These values were deemed adequate through examination of experimental diffraction patterns.

All simulations employed microscope parameters derived from the JEOL 200CX at the NCEM, that is 200KeV, spherical abberation of 1.2mm, half-width spread in defocus of 50Å, objective aperture radii of $.26Å^{-1}$ and $.6Å^{-1}$, and beam half-angle of convergence of 1.0mR. The $.6Å^{-1}$ aperture admits the <111> diffracted beams while

Column Defect Models

Concentration	Impurity Location (slice numbers)
$\frac{1}{30}$ (3%)	15,45,76
$\frac{1}{20}$ (5%)	10,30,50,70,90
$\frac{1}{10}$ (10%)	5,15,25,35,...
$\frac{1}{5}$ (20%)	3,8,13,18,...
$\frac{1}{3}$ (33%)	2,5,8,10,...
$\frac{1}{2}$ (50%)	1,3,5,7,...

Table 7-1: Impurity atom concentrations in the defect column employed in calculations. Slice numbers give the location of impurity atoms.

the .26Å^{-1} aperture only passes the central, transmitted beam.

Most images were produced with a Varian Plotter utilizing a half-tone graphics routine to convert the array of image intensity values as produced by the image simulation programs. This device possesses a 16-level greyscale (the human eye can distinguish about 40 different shades of grey). The greyscale in each image is set so that the highest and lowest intensities are respectively represented by white and black. This permits easiest examination of image detail, but gives the false impression that all images have an identical range of intensity values. This must be kept in mind when comparing images.

Results

Systematic simulations were first examined for columns containing arsenic to determine impurity observability as influenced by concentration, specimen thickness, objective aperture size, and objective lens defocus. Figure 7-2 shows a series of lattice images (objective aperture of .6Å^{-1}) for high concentration arsenic impurity columns as a function of specimen thickness. Note that the dumbell pair of atoms, separated by 1.36Å, appears as a single spot given the resolution of the 200CX (about 2.4Å point-to-point). The strongest image effects occur for a wide range in the relatively thick region.

To quantify this, image contrast was analysed by examining intensity values in the image intensity arrays. Contrast was defined as the absolute value of the intensity at the impurity column location minus that at the silicon column (pair) in the lower left corner as a ratio to the later:

Simulated Lattice Images of <110> Silicon

Substitutional Arsenic Impurity Column

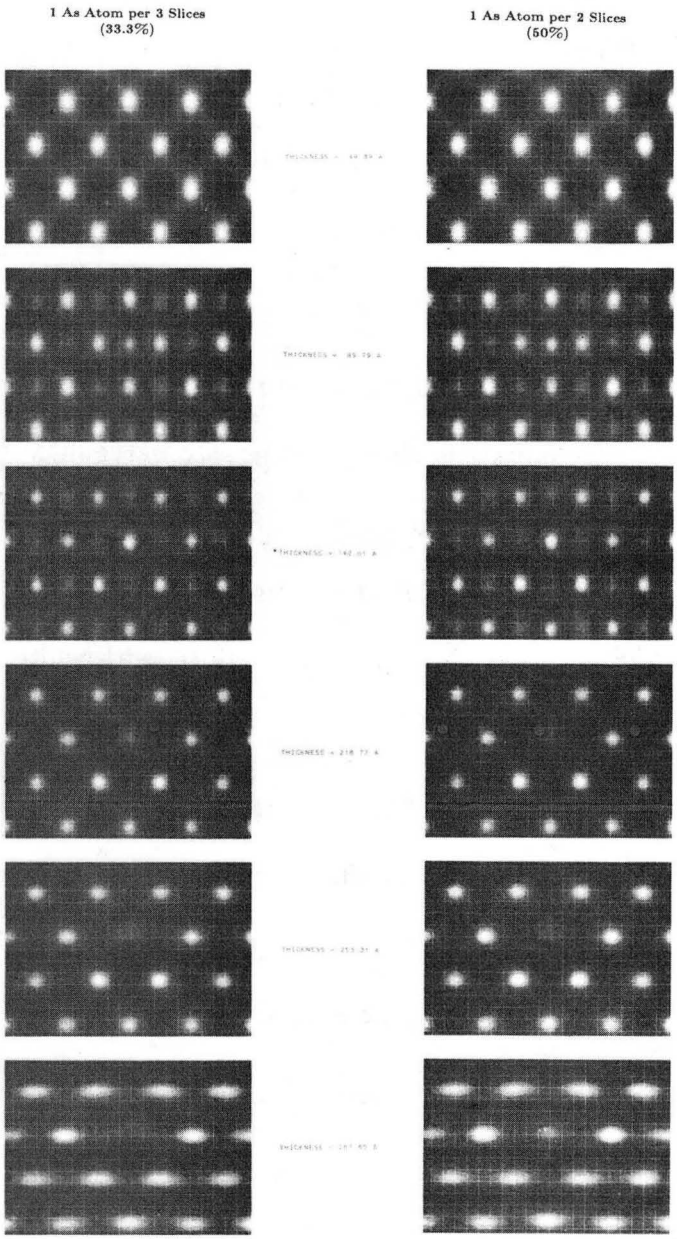

Fig. 7-2 Through thickness lattice image simulations of high concentration arsenic impurity columns. Impurity column is only strongly observable for thicknesses greater than $\frac{1}{2}\xi$.

XBB 857-5495

$$Contrast \equiv \left| \frac{(I_{impurity} - I_{silicon})}{I_{silicon}} \right| \times 100\% .$$

Intensity was obtained by averaging over the maximal intensity grey level of the white (or black) spot at the desired location. Since the computed images contain no noise, drift, and other such instrumental effects, there is no detection limit *per se*. However, Iijima suggests a minimum contrast level of 3% for experimental detectability.[60]

Contrast for the 33.3% and 50.0% arsenic columns is given in fig. 7-3. This agrees with a visual interpretation giving strongest observability for thicknesses of about 250Å with a pronounced drop at approximately 142Å. As expected, "black" atoms are found in the thin areas (50Å and 100Å). Here, the impurity "peak" is at a lower intensity than other peaks. In the thicker regions, with white atoms, the impurity again leads to a reduction in intensity.

To assist in the interpretation of these results, the Bragg beam intensities versus thickness for a <110> oriented perfect silicon crystal were calculated with the MULTISLICE program (fig. 7-4). The effective electron beam extinction distance (ξ) is seen to be 288Å. Comparing with fig. 7-3, the contrast dip is found to occur at $\frac{1}{2}\xi$ (144Å). Near this thickness, most of the image intensity is carried in the diffracted beams.

To examine the effect of exclusion of all diffracted beams, calculations were performed with an objective aperture of radius .26Å^{-1}. This is referred to as *diffuse imaging* since contrast in the image arises solely from interference between the transmitted beam and the diffuse scattering admitted out to the angular limit set by the aperture. Figure 7-5 gives as example through focal series at four thicknesses for a 10% arsenic

Fig. 7-5: Through focus, simulated diffuse images of a 10% concentration arsenic impurity column for four sample thicknesses. Δf is varied in 100Å steps from 400Å to -600Å (the final image is at Scherzer defocus [-660Å]).

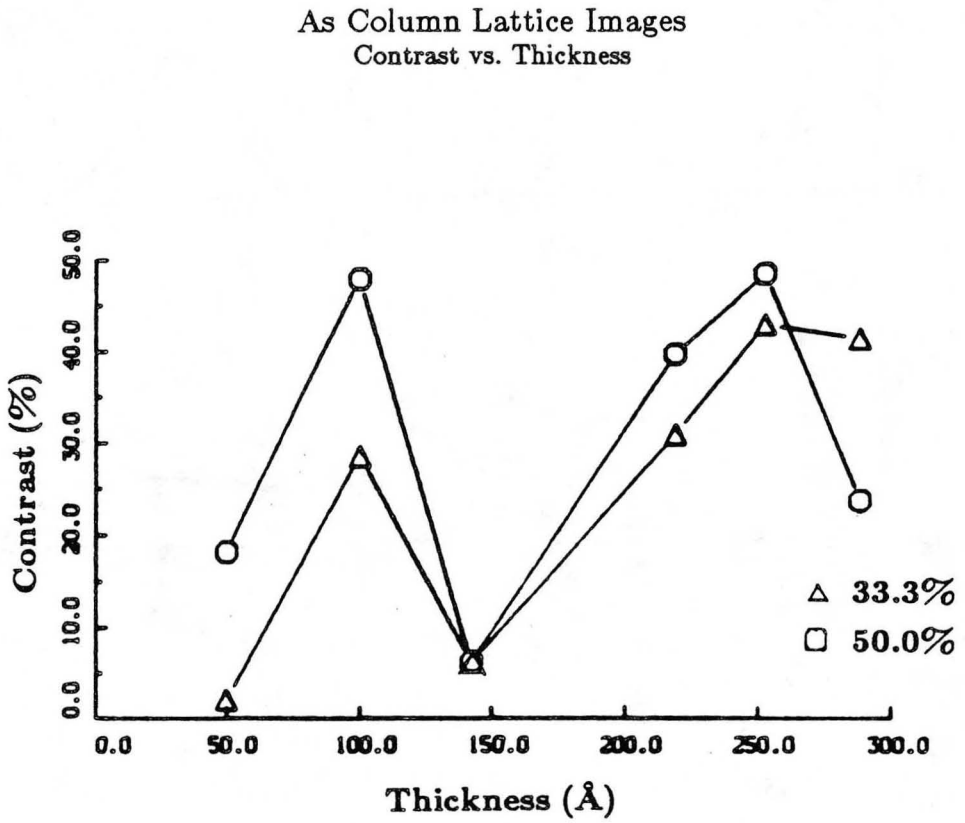

Fig. 7-3 Arsenic impurity column contrast in lattice images as a function of specimen thickness. Curves for two concentrations are given. The central minimum occurs near half the effective extinction distance.

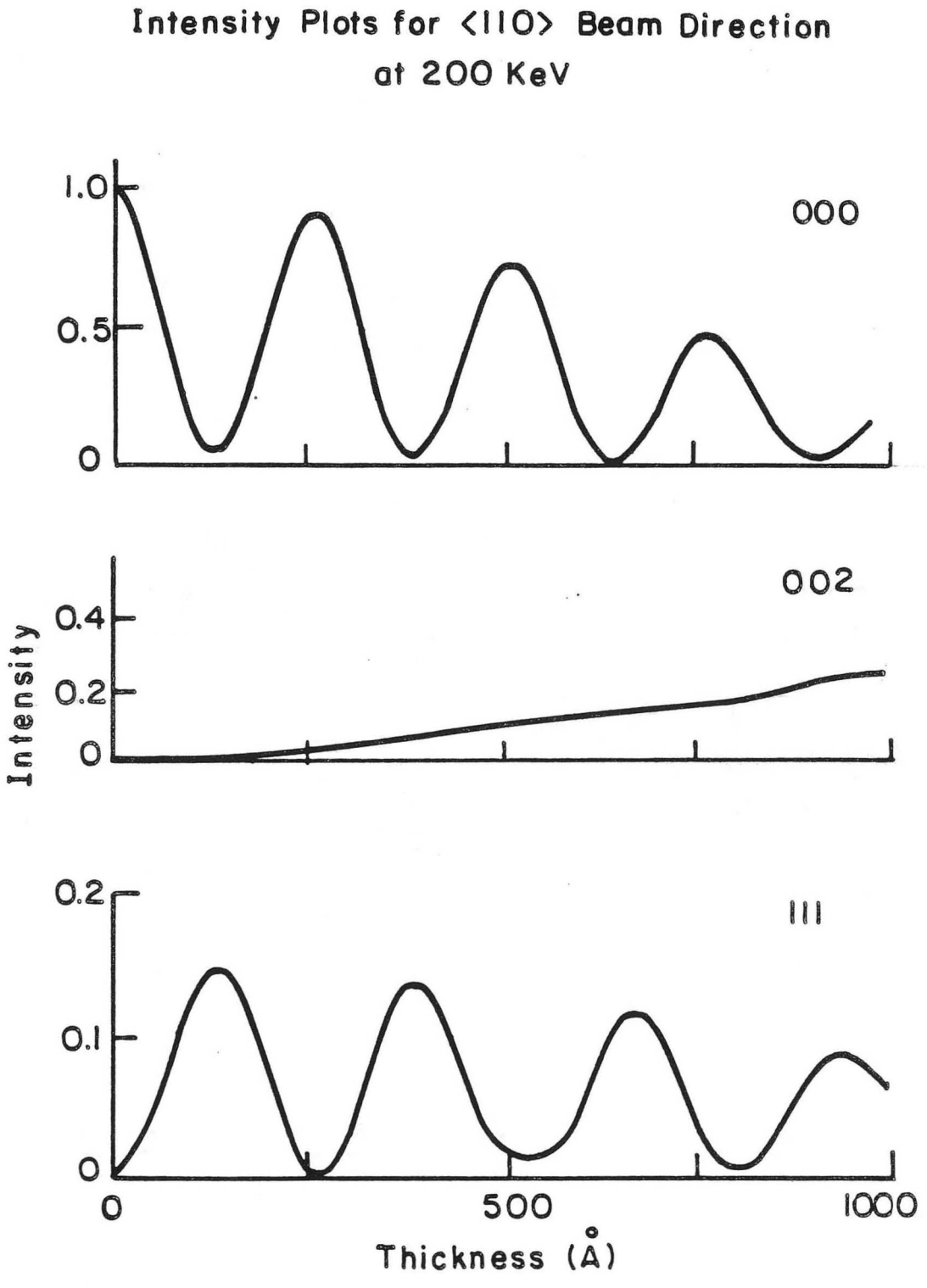

Fig. 7-4 Calculated intensity versus thickness plots of the transmitted and important Bragg beams for 200KeV electrons. The forbidden 002 beam arises from double diffraction. XBL 857-6403

10% Arsenic Column Diffuse Images

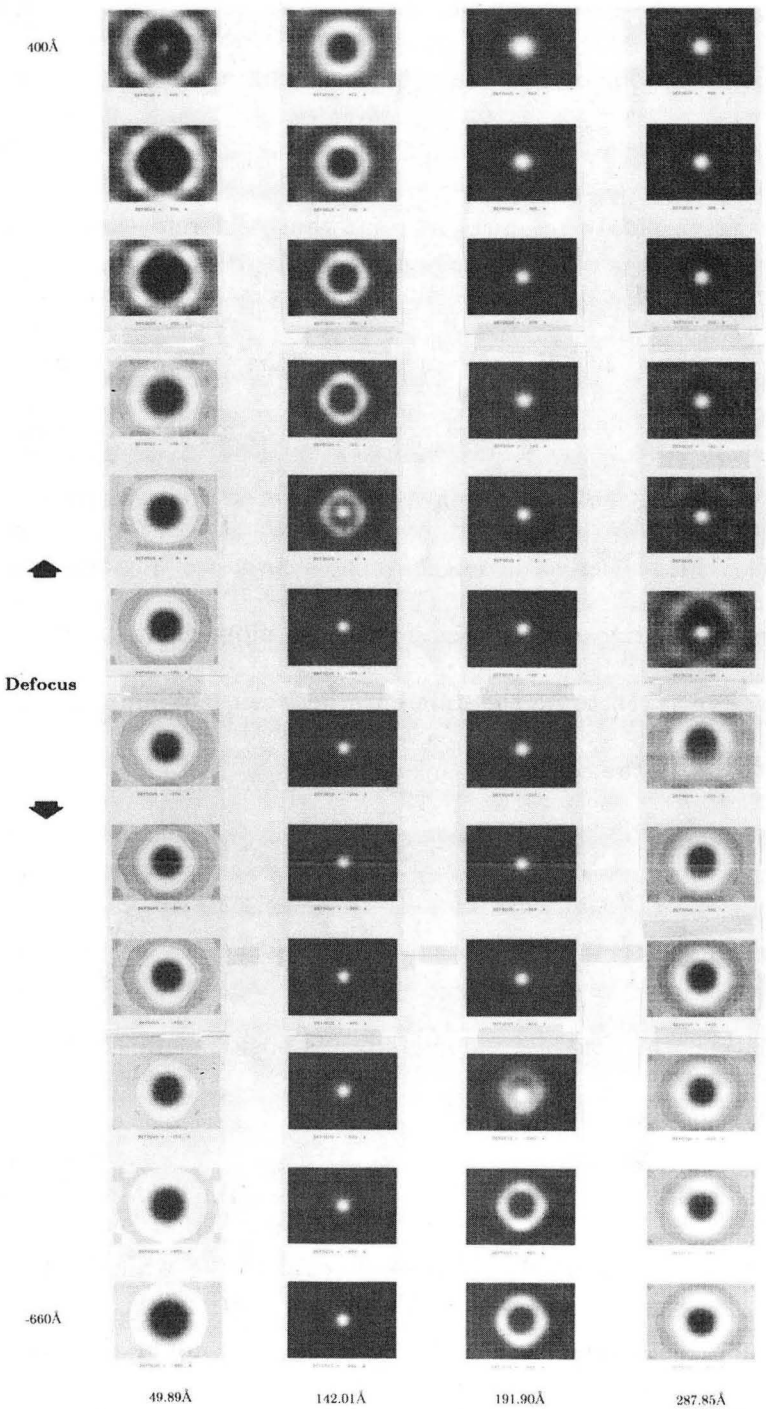

XBB 857-5500

Fig. 7-5

column. Images may be categorized as having a white or black "doughnut" appearance with transitions from one to the other occuring as one travels through focus or through thickness.

Diffuse images clearly require a somewhat different definition of contrast. Without the presence of a defect, the image possesses a constant intensity level since no phase contrast arises with the sole presence of the transmitted beam. If the introduction of a defect simply caused the appearance of a peak above or dip below this "background", contrast could be taken as the ratio of the peak (dip) height to background intensity. However, all defect images produce regions of increased and decreased intensity relative to the background. A more meaningful measure of image contrast is therefore taken to be the difference between maximum and minimum defect intensities as a ratio to the constant background:

$$Contrast = \frac{I_{\max} - I_{\min}}{I_0} \times 100\%$$

With this definition, the contrast value is always positive. Intensity values were averaged as for lattice images.

Graphically examining the diffuse contrast as a function of thickness in fig. 7-6, one notes a very *high* contrast for thickness equal to $\frac{1}{2}\xi$ while there is an additional broad peak in contrast centered at a thickness of ξ. It might then be hoped to utilize a thickness of $\frac{1}{2}\xi$ combined with diffuse imaging for optimum detection of impurities, however examination of fig. 7-7 demonstrates that image intensities are likely too low for practical exposure times for thicknesses in the 100Å to 200Å range. Glaisher and

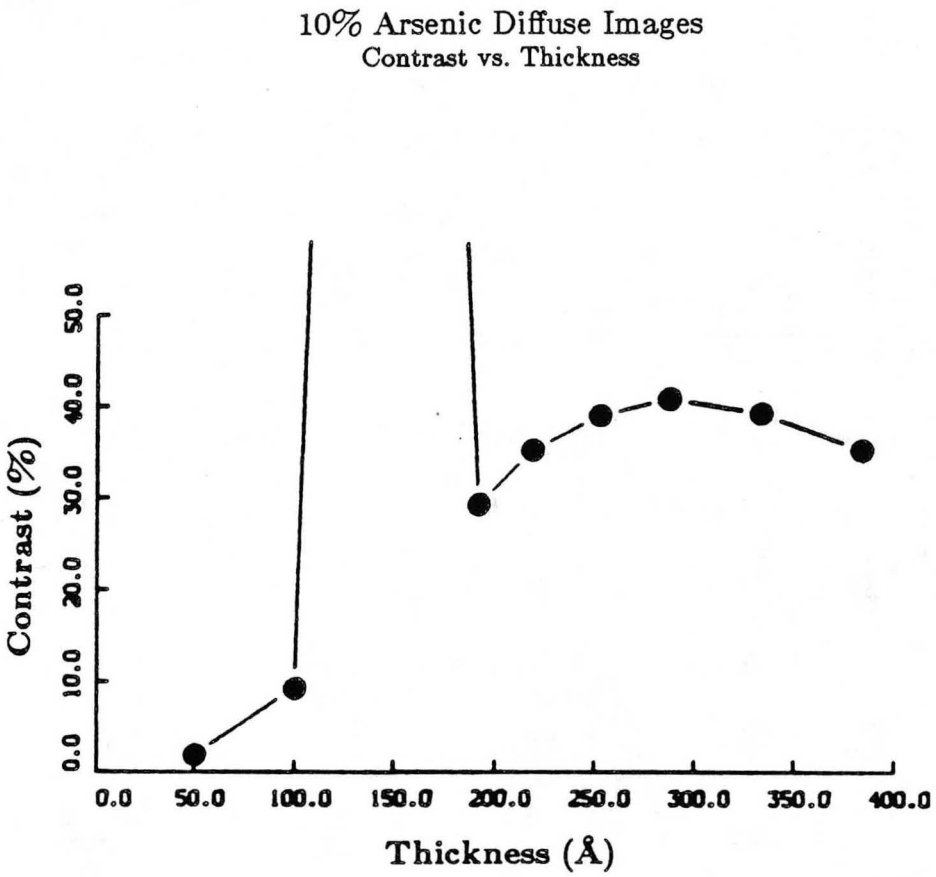

Fig. 7-6 Contrast as a function of specimen thickness for a 10% arsenic column. Arsenic atoms are in slices 5, 15, 25, etc. Maximum contrast (280%) occurs at half the extinction distance (ξ) with a secondary maximum at ξ.

Perfect Silicon Diffuse Images

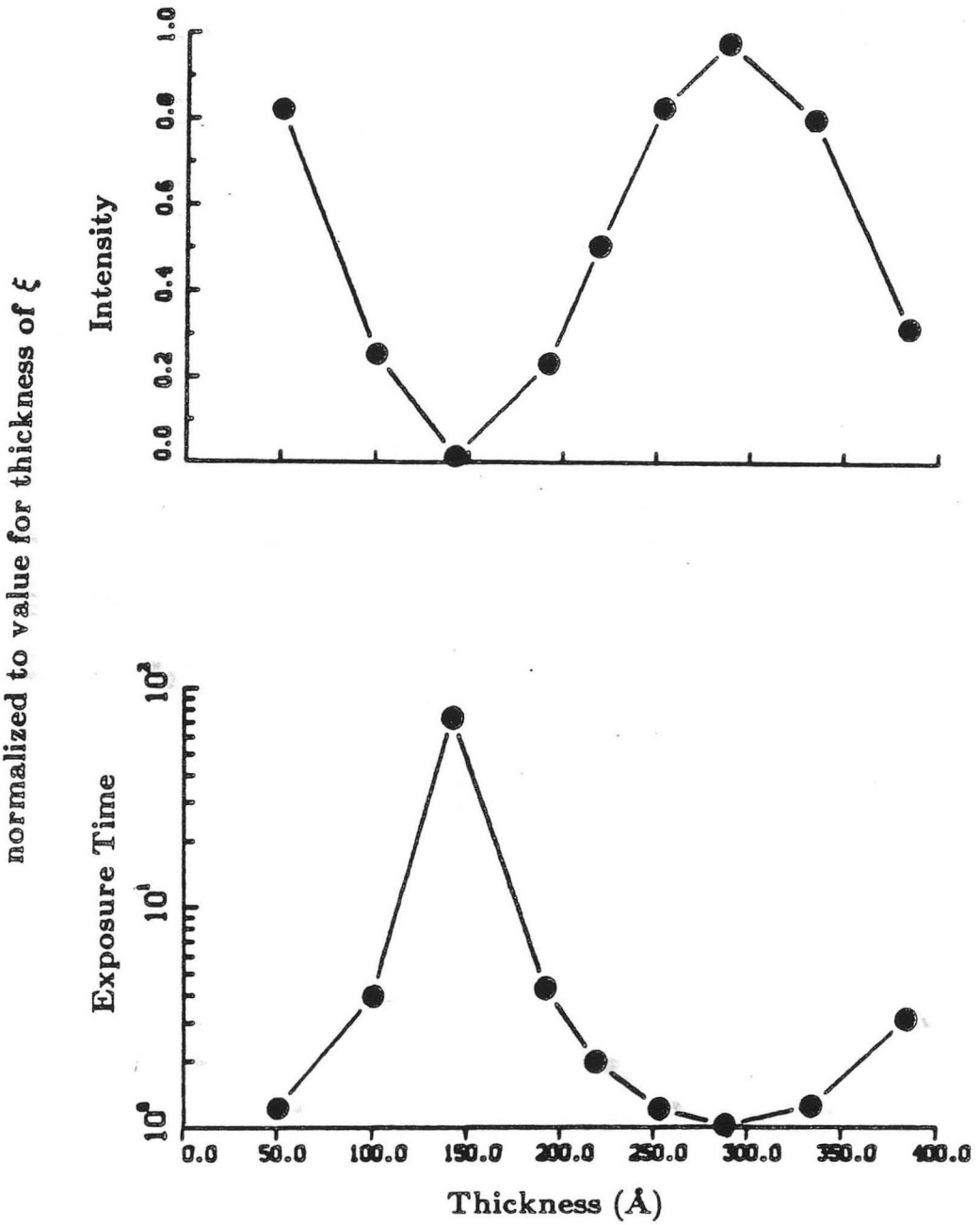

Fig. 7-7 Diffuse image intensity as a function of specimen thickness for a <110> oriented perfect silicon sample. Both intensity (a) and exposure time (b) are normalized to that for a thickness of ξ. Exposure times are prohibitively long in the 100Å to 200Å range.

Spargo came to the same conclusion concerning the imaging of a silicon self-interstitial.[61] This is simply a result of the weak transmitted beam (fig. 7-4). The minimal exposure time for thickness equal to ξ and high contrast previously noted led subsequent investigation to focus on image behavior at this thickness (288Å).

Figure 7-8 gives the contrast versus defocus behavior corresponding to the fourth column in fig. 7-5. Contrast peaks at -660Å with a secondary maximum at about 300Å. This is readily explained as a consequence of the maximized contrast transfer function first-order passbands encountered at these defocus values (-660Å is Scherzer defocus for the JEOL 200CX while the other defocus value optimizes the contrast transfer function for a range near +1, fig. 7-9). The clearest symmetry information locating the impurities in the lower member of the dumbell pair occurs at transitional defocus values (-500Å for t=192Å and -100Å for t=288Å). If the impurity column was located at the top of the dumbell, all images would be flipped about an x-y axis, given simple symmetry considerations.

Examining defocus effect in lattice images of a 10% arsenic column, similar optimum contrast values are found, fig. 7-10. At 100Å defocus (fig. 7-10 top), the impurity column has increased intensity in comparison with white silicon dumbells while at Scherzer defocus (bottom) the white spot has reduced intensity.

Again for lattice images, through concentration images are given in fig. 7-11 and contrast values in fig. 7-12. Visual detection requires greater than 5% arsenic though a densitometer trace would allow somewhat better detectability depending on the selected reliability level. Through concentration diffuse images appear in fig. 7-13 with the corresponding contrast curve in fig. 7-14. All images are similar in appearance, though there is some change at the highest concentrations which reflects the symmetry

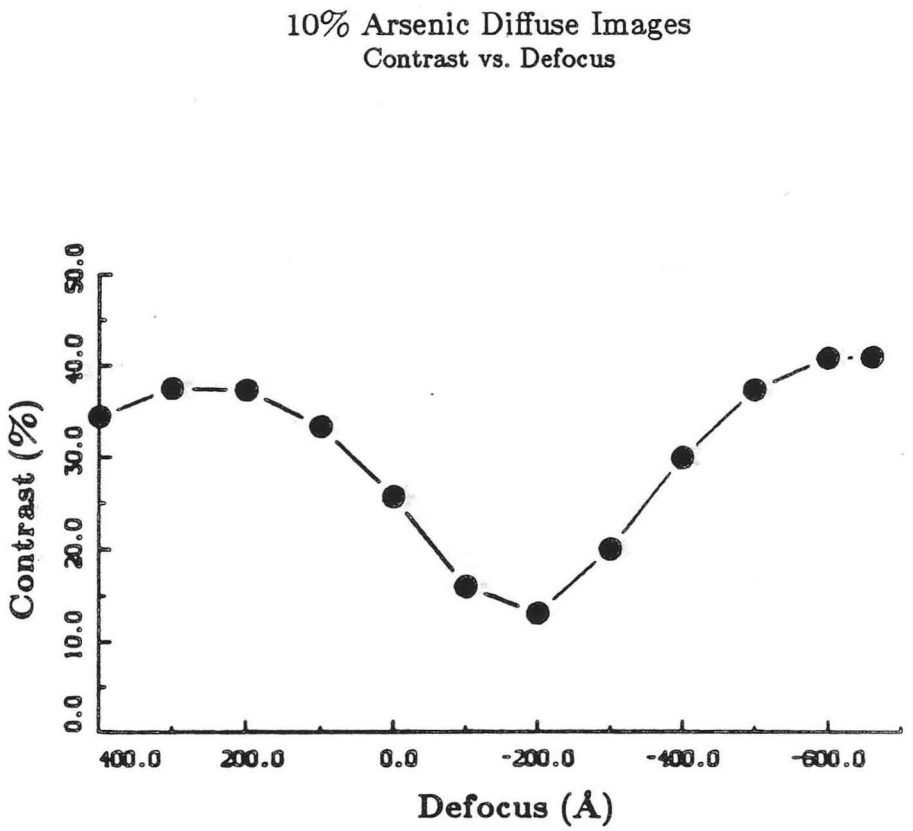

Fig. 7-8 Contrast as a function of defocus for diffuse images of a 10% arsenic column. The maxima occur for defocus values which permit the greatest amount of diffuse scattering to contribute to the image (-660Å is Scherzer defocus.)

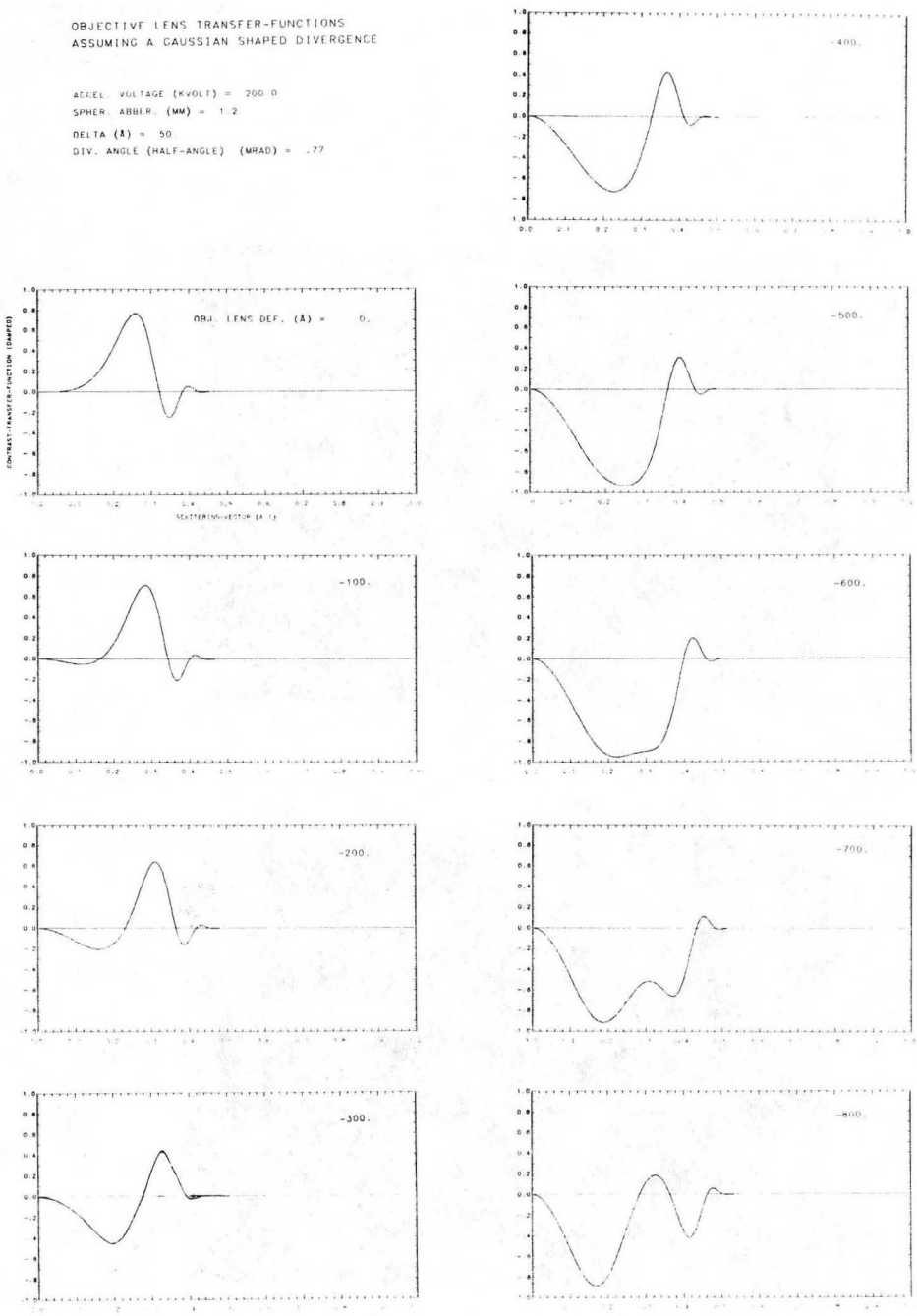

Fig. 7-9 Through focal series of damped contrast transfer functions for microscope parameters typical of the JEOL 200CX.

XBL 857-3120

Arsenic Column - 1 per 10 Slices

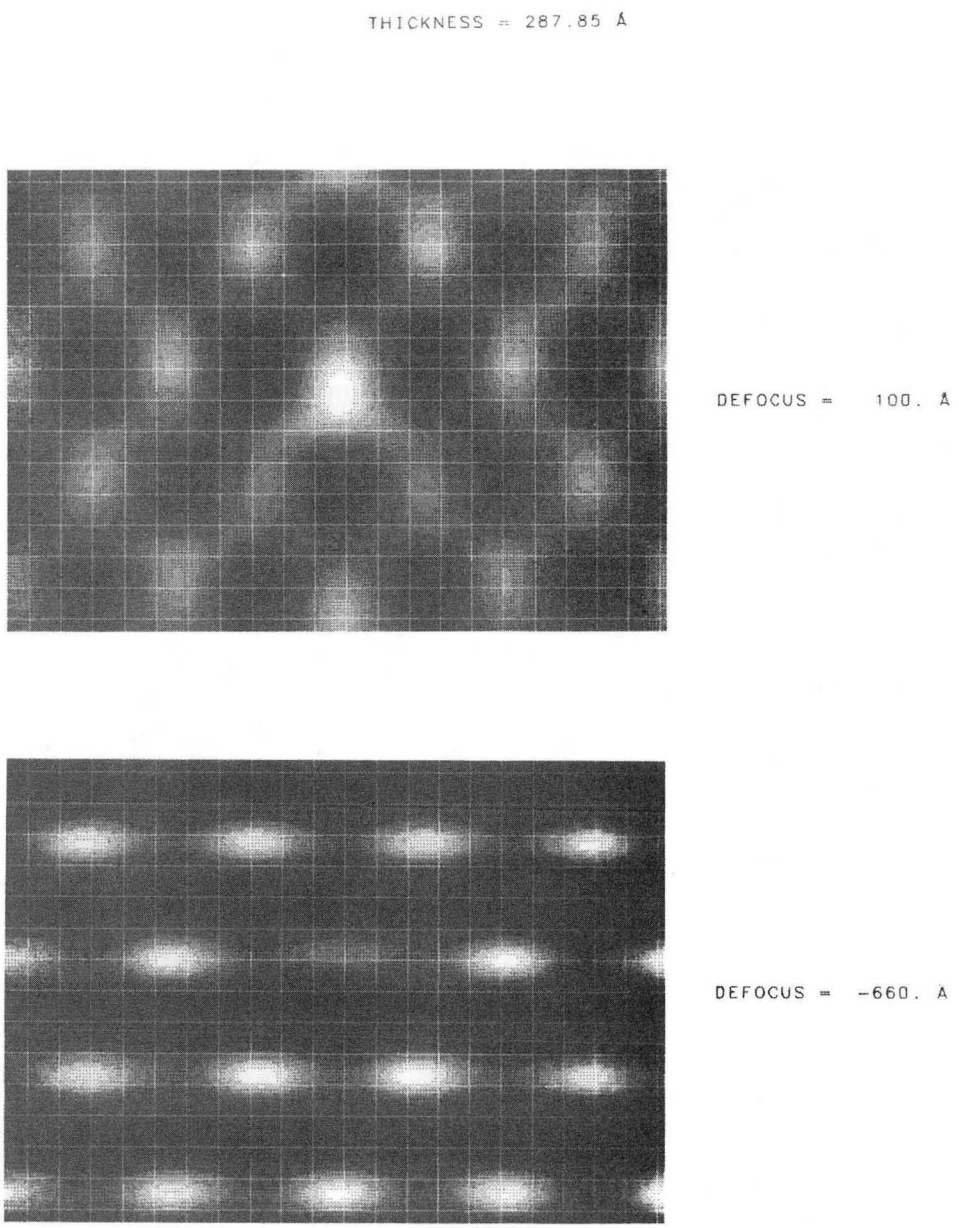

Fig. 7-10 Optimum thickness and defocus simulated lattice images for an arsenic impurity column.

XBB 857-5498

Arsenic Column - Through Concentration

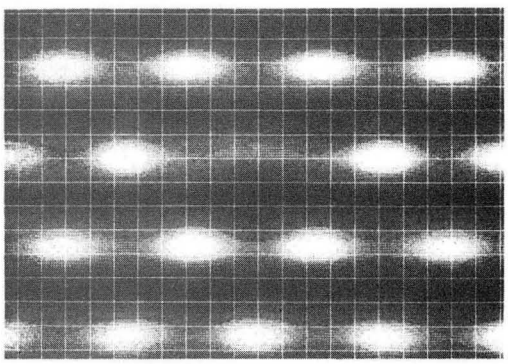

AS COLUMN 1 PER 5 SLICES

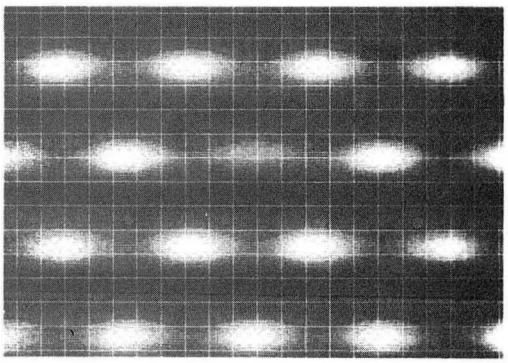

1 PER 10 SLICES

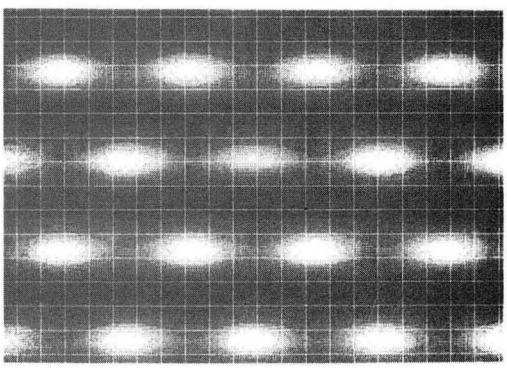

1 PER 20 SLICES

DEFOCUS = -660. A

OBJ AP = .60 A

THICKNESS = 287.85 A

VOLT = 200. KV

Fig. 7-11 Through concentration simulated lattice images of arsenic impurity columns. The detection limit is approximately 5% (bottom image).

XBB 857-4499

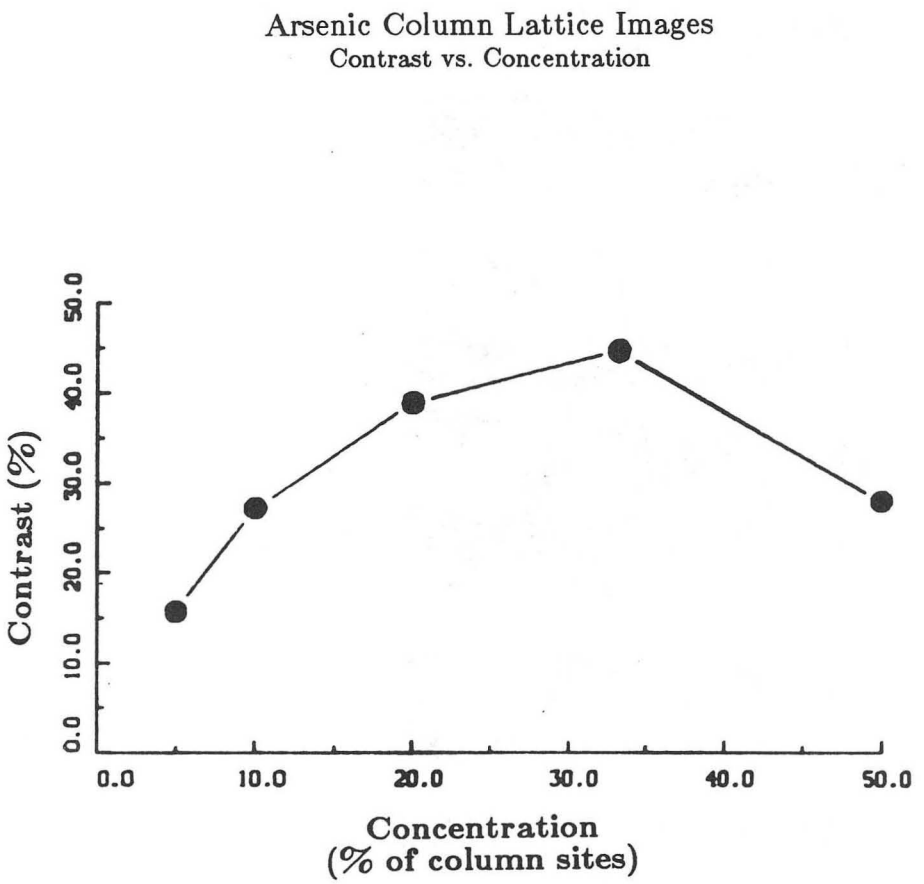

Fig. 7-12 Contrast as a function of arsenic line concentration for lattice images. The fall-off at high concentrations reflects spreading in the impurity image.

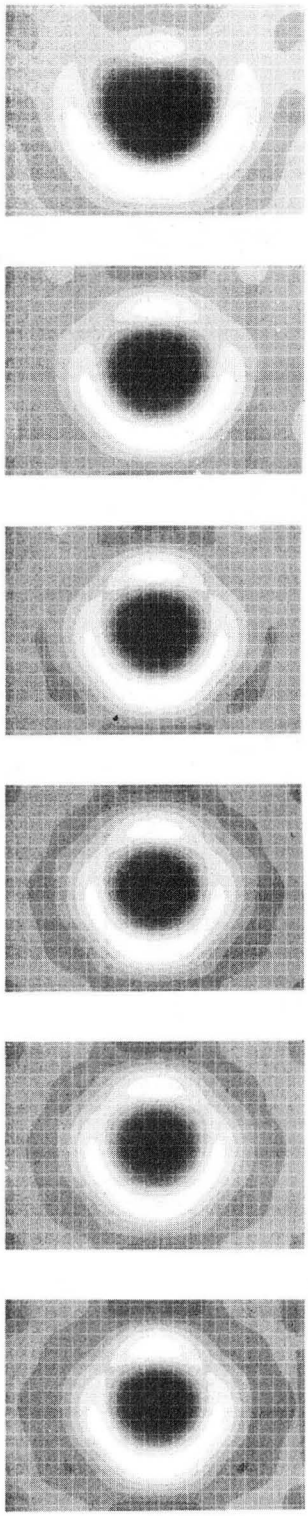

Fig. 7-13 Through concentration, simulated diffuse images of an arsenic column impurity. Image intensity extrema are indicated. Since these are assigned black and white values in each image, contrast falsely appears to be identical for all images. The detection limit is less than 3% (bottom).

XBB 857-5497

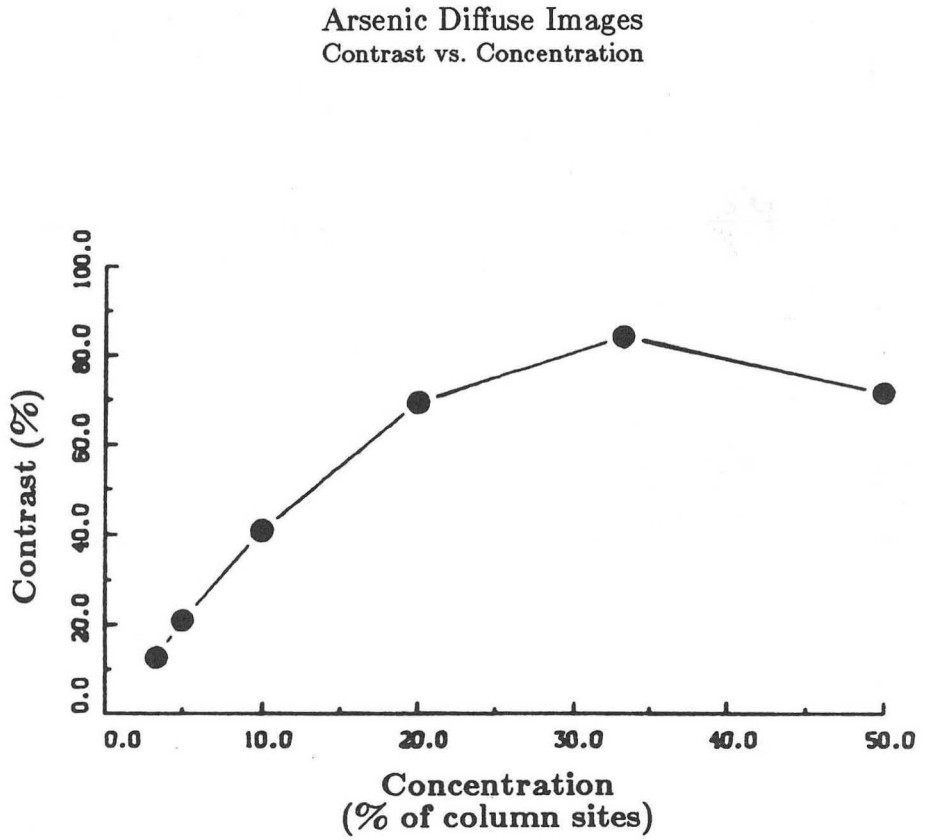

Fig. 7-14 Contrast as a function of arsenic line concentration for diffuse images. This has form similar to that for lattice image though contrast here is about twice as large.

of the defect. The drop in contrast at the highest concentration (50%) is misleading since image *size* has not been considered. The additional diffuse scattering expected here is accounted for in the increased area of the defect image (which would in fact make for easier detection in an experimental image).

To extend the above results to other dopant species, simulations for boron, phosphorus, and antimony were examined. Boron yields contrast levels similar to arsenic though with inverted image effects, i.e. reduced intensity in place of increased intensity and vice versa. For example, fig. 7-15 shows through focal images for a 10% boron column which may be compared to fig. 7-5 (contrast curve in fig.7-16). Here, images go from white to black doughnut rather than black to white doughnut. A boron defect lattice image, fig. 7-17 bottom, has enhanced white atom intensity rather than reduced as for arsenic (fig. 7-10 bottom).

Phosphorus, next to silicon in atomic number, yields much lower contrast than the above impurities. Figure 7-17 (top) shows optimum condition images for a saturated phosphorus column, i.e. all silicon atoms in the column have been replaced with the impurity. Contrast data for boron and phosphorus are given in Table 7-2.

Antimony proves to be a strong enough scatterer that single atoms are theoretically detectable with diffuse imaging. For this reason, it was selected to test the influence on imaging of the depth in a specimen of a single impurity atom. Figure 7-18 depicts a series of diffuse images for a single antimony atom located at varying depths from the surface of a sample of thickness ξ. Information concerning the location of the impurity in a dumbell is found with the impurity in the upper regions of

Fig. 7-18: Calculated diffuse images of a single substitutional antimony atom at various depths in an otherwise perfect silicon crystal. Specimen thickness and defocus are optimized and depth from the surface (toward the electron beam) is given in fractions of ξ.

Boron - 1 per 10 Slices

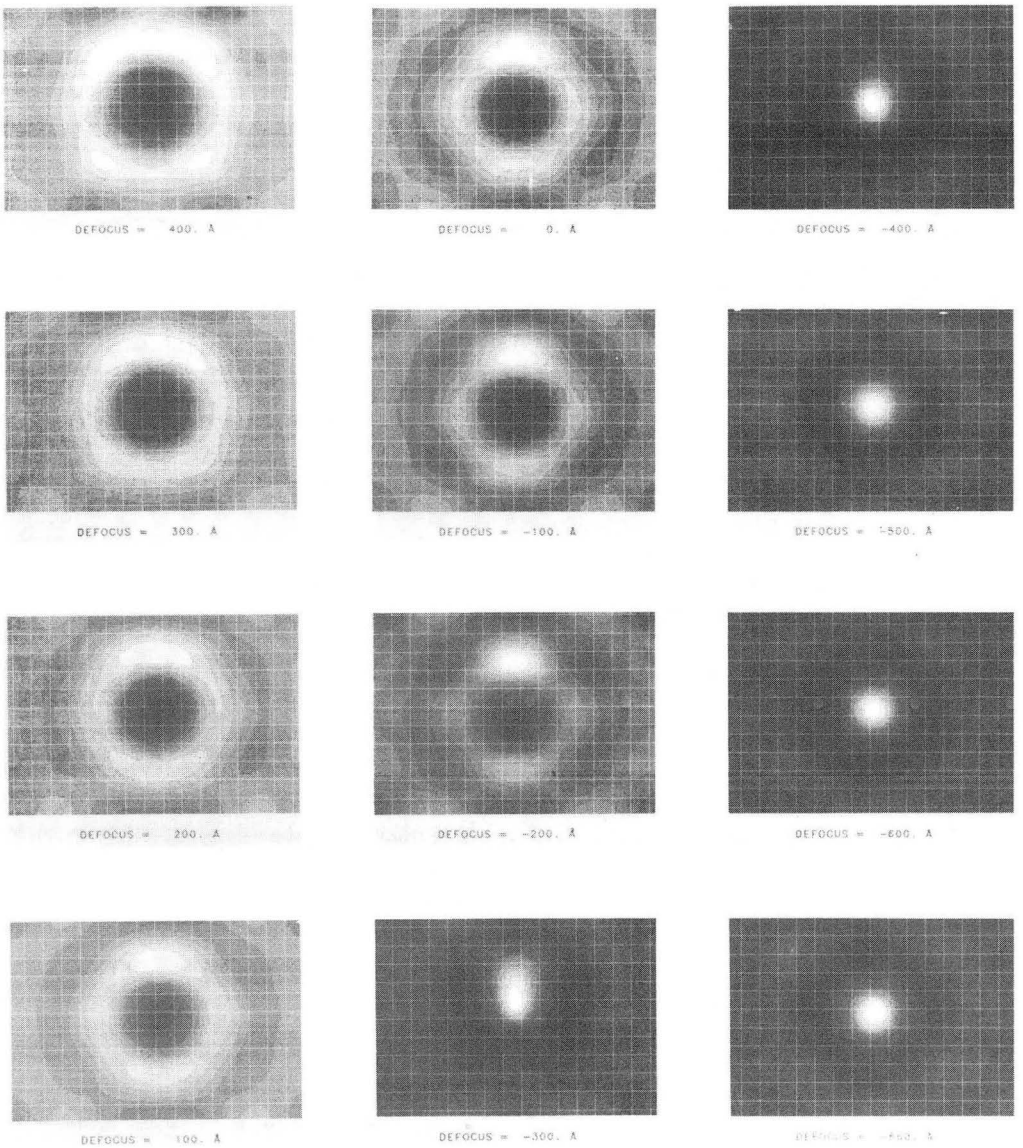

OBJ AP = 20 Å
THICKNESS = 287.85 Å

Fig. 7-15 Simulated through focal series of 10% boron column. The thickness is equal to ξ. Note that the progression from white "donuts" to black "donuts" is inverse to that of the heavy impurities.

XBB 857-5503

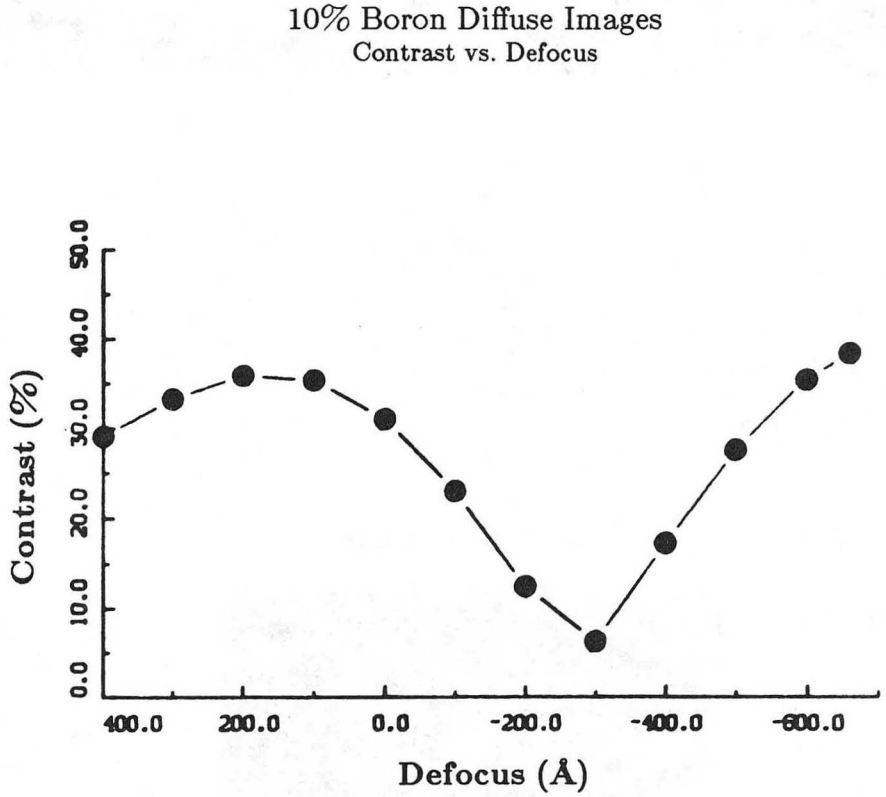

Fig. 7-16 Contrast as a function of defocus for a 10% boron column. As expected, the same form as for arsenic impurity is obtained as well as a similar contrast level.

Saturated Phosphorus Column

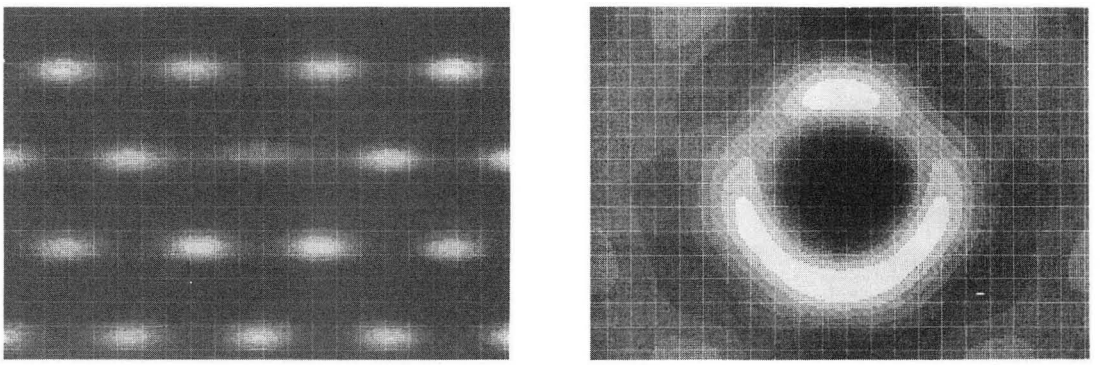

Fig. 7-17 Image simulations for phosphorus (top) and boron (bottom). At high concentrations, phosphorus is detectable with diffuse imaging while boron yields contrast effects similar to arsenic in magnitude though inverted in appearance.

DEFOCUS = -660. A
VOLT = 200. KV
THICKNESS = 287.85 A

Boron - 1 per 10 Slices

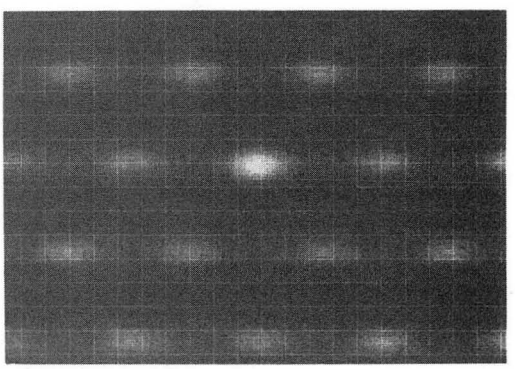

XBB 857-5502

Sb Atom Diffuse Images

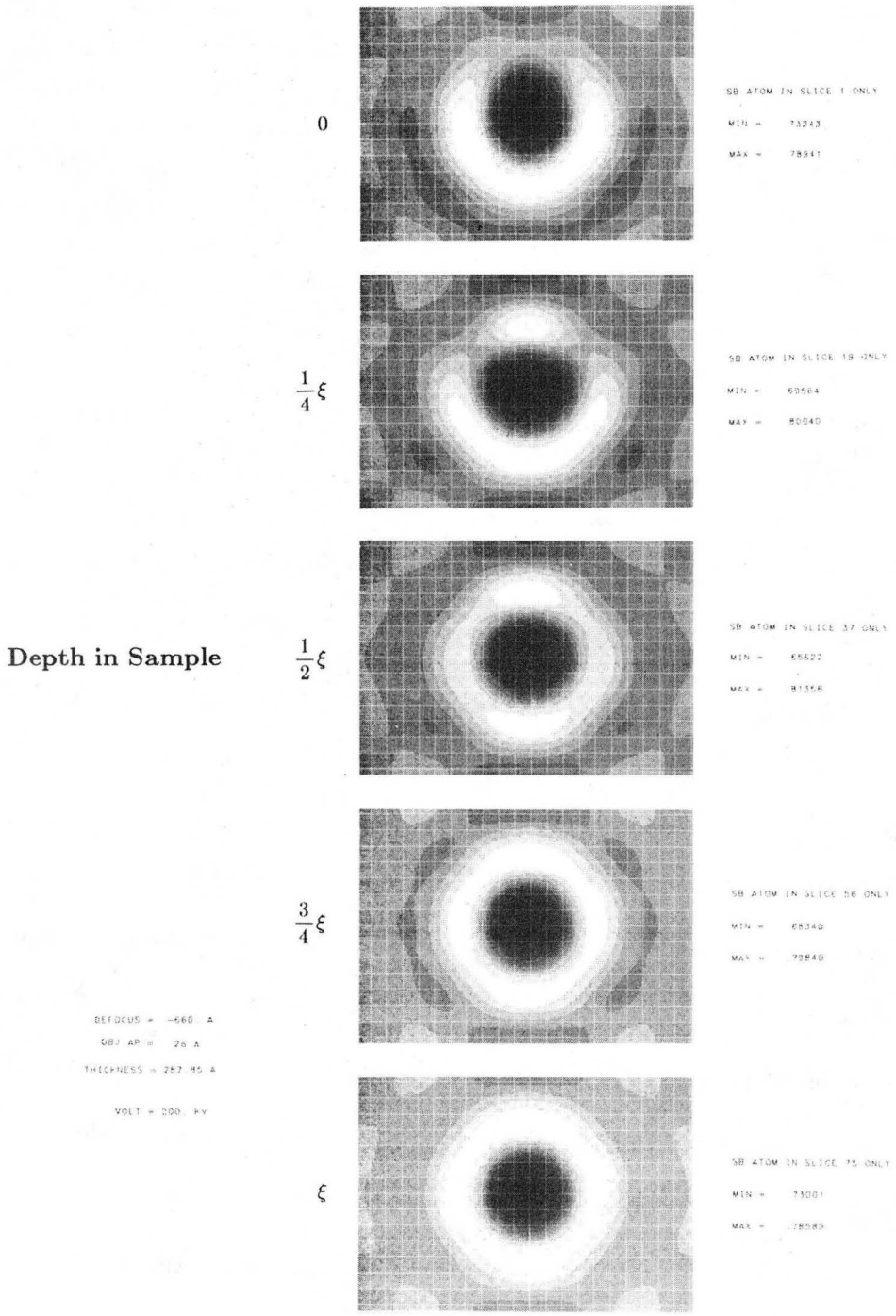

XBB 857-5501

Fig. 7-18

Image Contrast		
Impurity	Lattice Image	Diffuse Image
P (100%)	21.5%	29.9%
B (10%)	26.8%	38.4%
As (10%)	27.2%	41.0%

Table 7-2: Simulated image contrast values for boron and phosphorus impurity columns under ideal microscope and specimen conditions; thickness = ξ and defocus = -660Å (200CX). Arsenic is included for comparison.

the sample. In this location, the diffuse scattering due to the impurity has greater distance over which to interact with the scattering due to the crystal. Figure 7-19 gives the contrast versus antimony atom position. A gradual change in contrast appears with a maximum at $\frac{1}{2}\xi$.

Discussion

As seen in Chapter 5, a lattice image of a perfect crystalline specimen may be described in a relatively simple manner in terms of a transmitted and a few diffracted plane waves, each corresponding to a single spot in the back focal plane (BFP, reciprocal space). Any crystalline defect produces a continuum in the BFP which is accounted for in calculations with a discrete though still large set of points. In other words, there is no direct way to predict image contrast, hence the use of computers capable of processing large quantities of information. In the following, diffuse images are treated first.

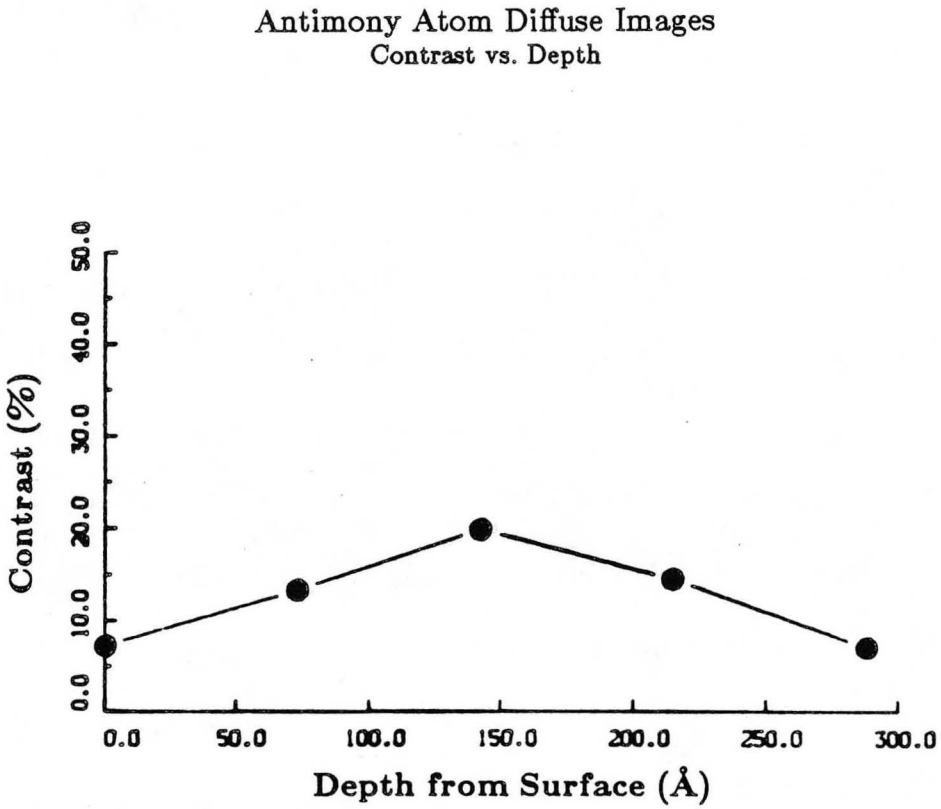

Fig. 7-19 Contrast as a function of position in the specimen for a single antimony atom. There is a gentle maximum for location in the middle of the sample.

To understand the origin of the images in the previous section it is best to begin with the simplest defect to interpret; a single impurity atom in the final slice of a sample. In this case, the electron wave function proceeds from the entry (top) surface until it interacts with the impurity as it leaves the crystal. The diffuse scattering from the impurity does not have the opportunity to interact with the scattering in the perfect crystal. In essence, with the exclusion of crystal Bragg reflections in a diffuse image, the image of a plane wave scattering from a single atom is expected.

Imaging of an isolated atom was described in 1949 by Scherzer, his expression for maximum contrast giving the aforementioned Scherzer defocus for optimum microscope resolution.[61] More recently, a number of researchers have experimentally and theoretically considered the imaging of heavy isolated atoms on low Z substrates.[62],[63],[64] A radially symmetrical image is expected. This is verified by the bottom image of an antimony atom in fig. 7-18.

An atom of moderate atomic weight may be treated as a weak phase object with considerations similar to those discussed in Chapter 5. The angular scattering distribution is peaked in the foward direction, relatively broader with increasing Z, and proportional to Z at higher angles. Under the approximations of Chapter 5 and taking the first Born approximation for the scattered wave due to an atom

$$\psi_{atom}(r) = \frac{\gamma}{rf(\theta)} e^{i\frac{r}{\lambda}},$$

the bright field image intensity of an atom utilizing an objective aperture of θ_{ap} is[65]

$$I(r) = 1 + \frac{4\pi\gamma}{\lambda} \int_0^{\theta_{ap}} f(\theta)\, J_0(\frac{2\pi\theta r}{\lambda}) \sin\chi(\theta)\, \theta\, d\theta$$

where θ is the scattering angle (for a crystalline reflection this is twice the Bragg angle), $r = \sqrt{x^2 + y^2}$, $f(\theta)$ is the atomic scattering factor, and $J_0(\theta)$ is the zero order Bessel function. At Scherzer defocus, this predicts an image dominated by a dark central region surrounded by alternating light and dark bands of decreasing intensity. The same effect gives rise to the Fresnel fringes observed by the edge of thin specimens, serving as a focusing and astigmatism correction aid. Increasing the focus value until $\sin\chi(\theta)$ is optimized for values near $+1$ produces a white cental image (fig. 7-5).

With the impurity atom moved from the bottom surface, the scattered electrons may interact dynamically with the crystal Bragg beams. For a thin specimen ($\sim$50Å), the image should remain essentially unchanged. However, for thicker specimens such as depicted in fig. 7-18, the crystal should have an increasingly strong effect on the impurity image as the impurity shifts position toward the top surface. The antimony atom at position ξ has a radially symmetrical image while near the top it has the symmetry of the defect slice model, that is, a vertical mirror plane through the dumbell containing the antimony atom. Hence, a diffuse image not only tells of the presence of a defect, but may also provide configurational information.

Perhaps more surprising is the small change in image size with position. This indicates that the general features of the image are dominated by the initial scattering in a region $\sim$10Å in diameter. This has a fairly simply explanation. The objective aperture admits scattering angles to 3.25mR (.374°). A point at the top surface leads

to a cone of radiation with radius ~1Å at the bottom surface, small in comparison to the initial size. Any aperture large enough to lead to substantial spread in the image would also pass multiple beams and hence produce a lattice image.

More surprising is the gradual increase in contrast as the antimony atom moves toward the center of the sample. Bursill and Jun found no contrast change with depth in the specimen in calculations on point defects in rutile.[66] With the antimony atom centered in the sample, it is at a depth of $\frac{1}{2}\xi$ so that the diffuse scattering originates entirely from the crystal Bragg beams. If anything, this might be expected to lead to a reduction in diffuse scattering passing through the aperture and a concurrent reduction in contrast, however the opposite transpires.

The above concepts may be extended to an impurity column by assuming that position effects are averaged by superposition. Indeed, the through focal and through thickness image behavior shows no new features. Varying the concentration of impurity atoms in a particular sample (e.g. the number of arsenic atoms in fig. 7-13) leads to contrast approximately proportional to concentration until at high concentrations ($\geq$50%) the image spreads enough in size to produce a reduction in contrast.

As noted, through focus image behavior has its basis in phase changes imposed by the objective lens, pictured in simplified form with the CTF. The through focal behavior is similar, but arises from the amplitude differences between the diffracted and diffuse "beams". For a sample of thickness $\frac{1}{2}\xi$, the image is inverted (black doughnut) as in fig. 7-5. Here, the transmitted beam is so weak that the diffuse scattering dominates the image, yielding greatest intensity at the center of the image (white). Naturally, such image behavior could not occur for a free-standing atom.

As found in fig. 7-5, configurational information arises at transitional defocus values, though only in thicker samples. In thin regions, the impurity scattering has insufficient opportunity to couple to the lattice beams. In thicker regions, one must cautiously resort to CTF's to elucidate image characteristics. The interaction with the lattice has likely affected the angular distribution of scattering as a function of position: this manifests itself in the image at a defocus which includes similar amounts of $\sin\chi$ values near -1 and +1.

Next, consider the influence of impurity species. For an isolated atom, changing Z essentially can affect contrast only. Calculations show that contrast is nearly proportional to $Z,$[67] as expected, since image intensity levels are proportional to the projected potential in a thin specimen. However, an impurity atom of lower Z (scattering power) than the matrix atoms gives inverted contrast (as observed for boron, fig. 7-15). While the dopants with $Z>14$ produce a surfeit of scattering at all angles relative to silicon, boron yields less: in an abstract (and crude) sense, it creates "negative" scattering or, rather, acts as an absorber when substituted for an atom in the silicon lattice. Mathematically, absorption is expressed by a complex atomic potential. This serves to change the sign in the earlier expression for $I(r)$, giving a white central spot at Scherzer defocus.

Finally, these considerations must be extended to the lattice image observations of the previous section. It becomes particularly apparent here that an intuitive approach to image feature prediction can be very dangerous. Since the phases of all beams are a function of thickness, only calculated images suffice for thicknesses greater than 50-100Å.

Referring to fig. 7-2 (through thickness arsenic impurity images) and fig. 7-17 (boron image), one notes that the defect's contribution to the lattice image is equivalent to that for diffuse images, though here it is somewhat masked by the lattice image. For example, for an arsenic column at 288Å thickness there is a decrease in intensity at the defect location while near $\frac{1}{2}\xi$ the impurity leads to an enhanced spot (compare with fig. 7-5). The variation in contrast with thickness, fig. 7-3, is similar to that for diffuse imaging, fig. 7-6, but for the drop rather than sharp peak in contrast at $\frac{1}{2}\xi$. At this thickness, the strong diffracted beams hide the impurity peak.

Again for a 10% arsenic impurity, fig. 7-10 demonstrates the predicted behavior at two defocus values for a thickness of ξ (whiter at 100Å and darker at -660Å). However, the lattice image has white atoms at both settings demonstrating that the CTF is invalid at this crystal thickness. On the other hand, the CTF proves to remain applicable to diffuse scattering over much greater thicknesses than for crystal scattering.

7.2. Impurity Columns at Defects

In this section, insight gained from consideration of the artificial defects of the previous section are applied to the 30° dislocation and $\Sigma 9$ grain boundary segregation models of Chapter 4. As noted there, segregation in these defects likely leads to impurity columns at specific sites in the defect core. The problem then becomes the extraction of impurity diffuse scattering from diffuse scattering due to crystalline disorder associated with the dislocation or grain boundary.

Calculations first require atomic positions. For the $\Sigma 9$ grain boundary, a simple computer program and plotting device were used to generate a set of points for a rigid

rotation. An image of the zigzag model from Chapter 4 was next projected onto the rigid atom position plot and atoms were shifted in the core region to fit the model (this also required a small translation of one grain relative to the other). The final model is depicted in fig. 7-20. Its height is equal to one repeat distance of the grain boundary. The two interstitial impurity sites are indicated by +'s.

A problem arises here which is common to all strain field inducing defects, that is, selection of calculational unit cell boundaries. In the case of the Σ9 grain boundary, no choice of the X-dimension can give a smoothly connected boundary for the periodic continuation. This violation of the boundary requirements of the Fourier transform leads to anamolous image features in the region neighboring the cell boundary. These effects were found to be limited to approximately 5Å distance from the boundary. Cell sizes were optimized by making certain that the defect core was sufficiently isolated from the cell boundary effects, while keeping the phase grating sampling interval small enough for a meaningful calculation. For final image presentation, the distorted border regions have been masked.

The Σ9 cell parameters are 32.57Å by 11.51Å. The phase gratings were calculated to $1.9Å^{-1}$ in reciprocal space giving 4479 coefficients which were limited to 1182 beams ($1.0Å^{-1}$) for the multislice.

For the 30° dislocation, atom positions were calculated using isotropic linear elasticity theory for a split 60° dislocation with partials separated by 27Å. Though this theory fails exactly in the region of interest, the dislocation core, it was found to give atom positions which matched reasonably well with those found from physical models.

Σ9 Calculational Unit Cell

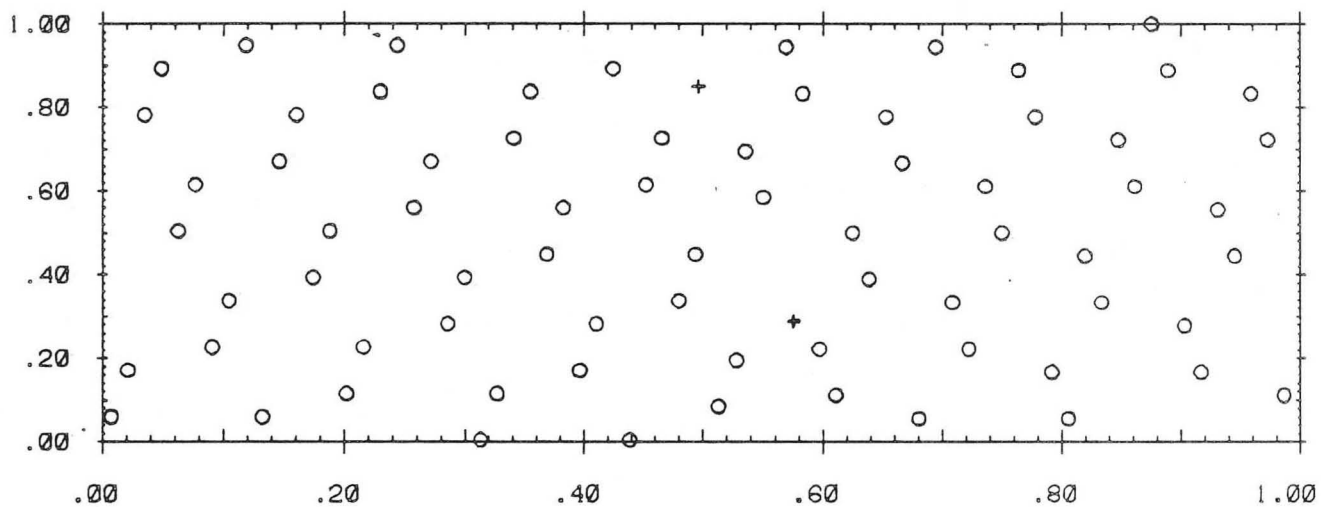

Fig. 7-20 The Σ grain boundary model calculational unit cell. The vertical dimension is that of the CSL. The centers of the interstitial segregation sites in the two 7-rings are marked with +'s.

A region surrounding the 30° dislocation with dimensions 26.27Å by 25.18Å was selected for simulations (fig. 7-21). Note that all boundaries are mismatched. Here (and for the side borders of the Σ9 model), the exact location of the cell borders and nearby atoms were adjusted to approximate as best as possible a physically reasonable continuation.

For the 30° dislocation, the phase-gratings were calculated with 8313 coefficients ($2.0Å^{-1}$) and the multislice with 2078 beams.

Programs written for model atom position calculations are given in Appendix C while atom positions are found in Appendix D.

Dislocation Results

Image simulations were performed for the shuffle and glide 30° dislocation models without impurities and with 10% arsenic atoms in the impurity site of the glide dislocation segregation model of Chapter 4. Lattice and diffuse images at the optimum conditions discussed in the previous section are shown in fig. 7-22.

Considering first the clean shuffle and glide models, top and middle respectively, one observes distinctly differentiable features in the lattice images, i.e. the additional white spot in the center of the glide model image. Earlier image calculations of these dislocations, again for a JEOL 200CX (until recently the state-of-the-art in high-resolution transmission electron microscopes), demonstrated that the two models could only be distinguished indirectly through careful evaluation of symmetry features in the images.[68] These workers only considered very then specimens, i.e. under 100Å. However, since defect configurational information lies in diffuse scattering, one apparently should maximize the image contrast arising from this scattering.

Shuffle Model

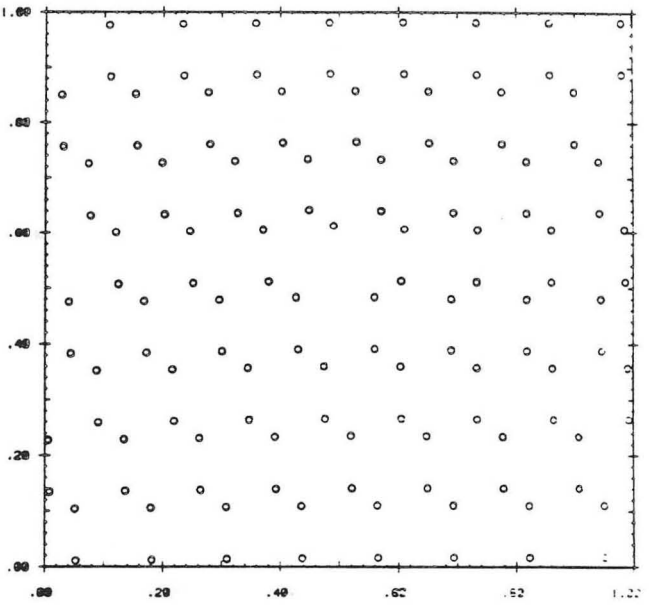

Glide/Segregation Model

(+ = segregating donor)

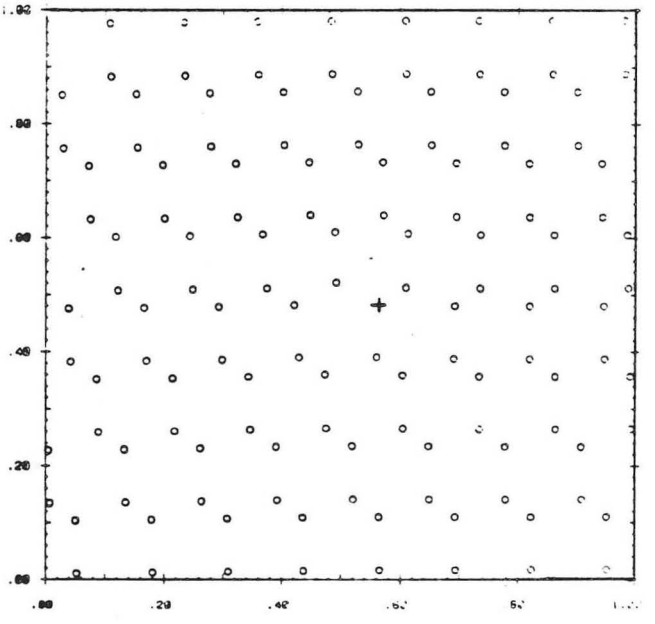

Fig. 7-21 Calculational unit cells for the shuffle and glide dislocation models. Atom positions for the glide/segregation model are the same as for a clean glide dislocation.

30 ° Dislocation Models
Lattice and Diffuse Images

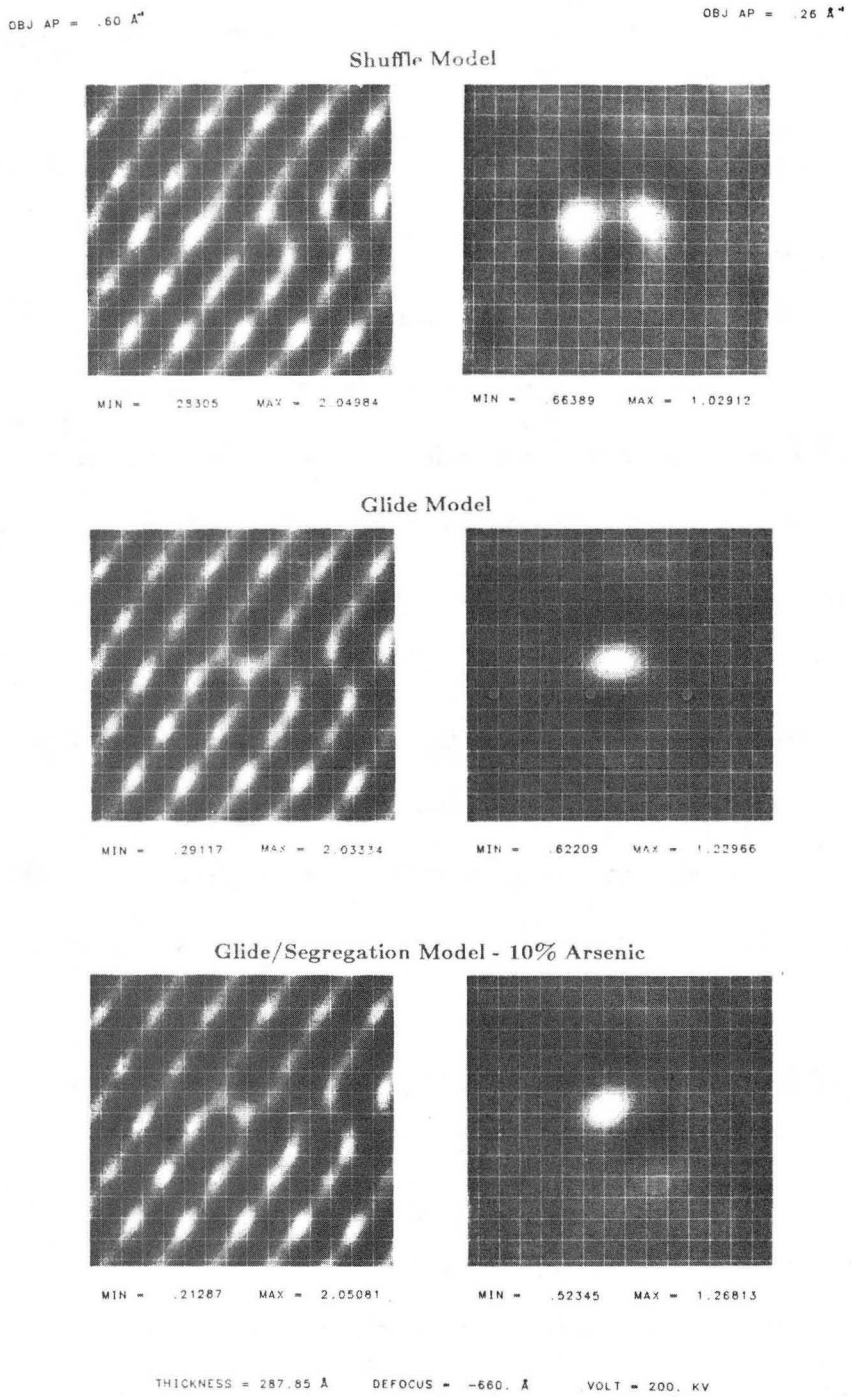

Fig. 7-22 Lattice (left) and diffuse (right) calculated images of the 30 ° shuffle dislocation model (top), glide model (middle), and glide model with 10% arsenic substitutional impurity (bottom), where the thickness is ξ. Minimum and maximum image intensity values are given below each picture to aid in comparison.

XBB 857-5496

The diffuse images (on the right) also serve to uniquely identify the models, indicating that addition of a column of atoms (glide model) greatly alters the diffuse scattering. These images have the same genre of features as the earlier impurity columns. In addition, they here have a "boron-type" image rather than an "arsenic-type" image (black central spot).

With introduction of 10% arsenic into the glide dislocation (bottom images), one finds changes in contrast rather than new image features. In the lattice image, there is a decrease in intensity below and to the right of the "glide spot" rather than a reduction in intensity of a particular white spot as for an arsenic column in an otherwise perfect crystal (fig. 7-10). In the diffuse image, contrast is increased and the image appears to be slightly rotated.

To assess the level of contrast arising from the strain field and the detectability of the impurity, contrast was again evaluated as for the unstrained lattice defects and is reported in Table 7-3. The clean defects have contrast equivalent to an arsenic column of concentration in the range of 15 to 20% as seen in Section 7-1. This suggests that segregated arsenic impurity of $\geq$10% concentration will give significant image contrast changes. This is verified by the entry in Table 7-3 showing that segregation has increased contrast by a factor of 1.23.

Grain Boundary Results

For the Σ9 grain boundary calculations, gold was selected as the interstitial impurity to examine the observability of a heavy impurity (in reality, it is primarily substitutional). Simulations were performed for a clean grain boundary and for a grain boundary with a single gold atom in slice 5 for the top 7-membered ring and

30 ° Dislocation **Diffuse Image Contrast**	
Model	Contrast
Shuffle	46.2%
Glide	76.9%
Glide/10% As	94.3%
10% As	41.0%

Table 7-3: Diffuse image contrast at optimum specimen thickness and objective lens defocus for the 30 ° shuffle and glide models and the segregation model with 10% arsenic. The 10% arsenic column defect from the previous section is repeated at bottom for comparison.

gold atoms in slices 5,15,25,...etc. for the bottom ring (10%). This provided more information for the same amount of computer time.

Figure 7-23 presents simulated diffuse images for thin samples of the clean and the segregated models. For clarity, each image consists of two grain boundary repeat lengths. There are two white spots per repeat length corresponding to the two zigzagging Lomer dislocation cores (four per image). Here, white spots approximately mark the location of the 7-rings while the darkest regions in the images locate the 5-rings. Based on the earlier conclusions, introduction of gold should slightly dim the intensity of the white spots. This may be observed in the high concentration gold columns in the lower right image.

A sample of optimum thickness, ξ, imaged at two defocus values is depicted in fig. 7-24. As for an impurity image, the grain boundary image intensity maxima and minima invert with the change in defocus (left). Addition of gold (right) gives the expected type of contrast changes. At 200Å defocus, the 7-ring white spots increase

Silicon Σ9 Grain Boundary

Diffuse Simulated Images

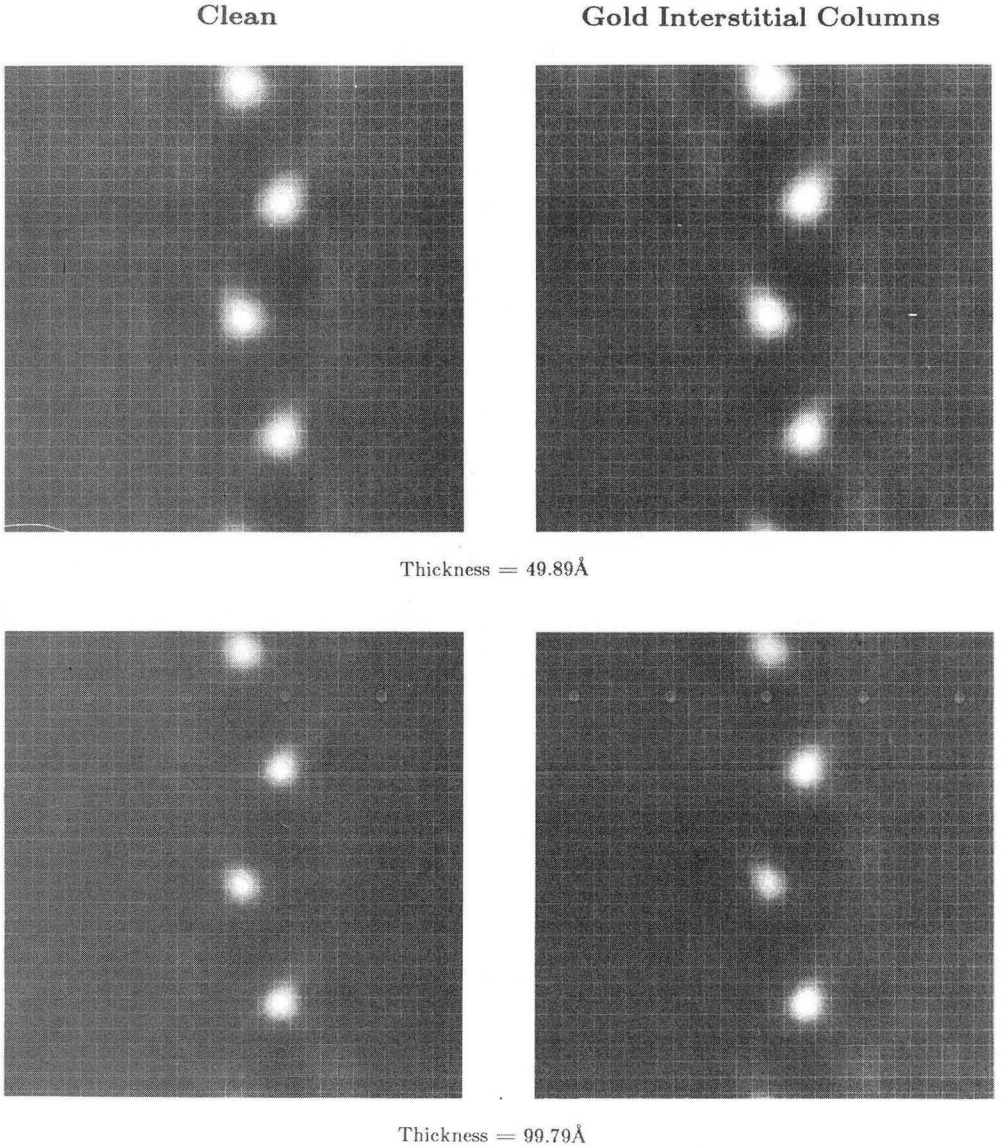

Fig. 7-23 Diffuse simulated images at two relatively small thicknesses of the Σ9 grain boundary model (left) and the model containing gold interstitials (right). Two grain boundary repeat units (vertical) appear in each image.

XBB 857-5494

Silicon Σ9 Grain Boundary

Diffuse Simulated Images

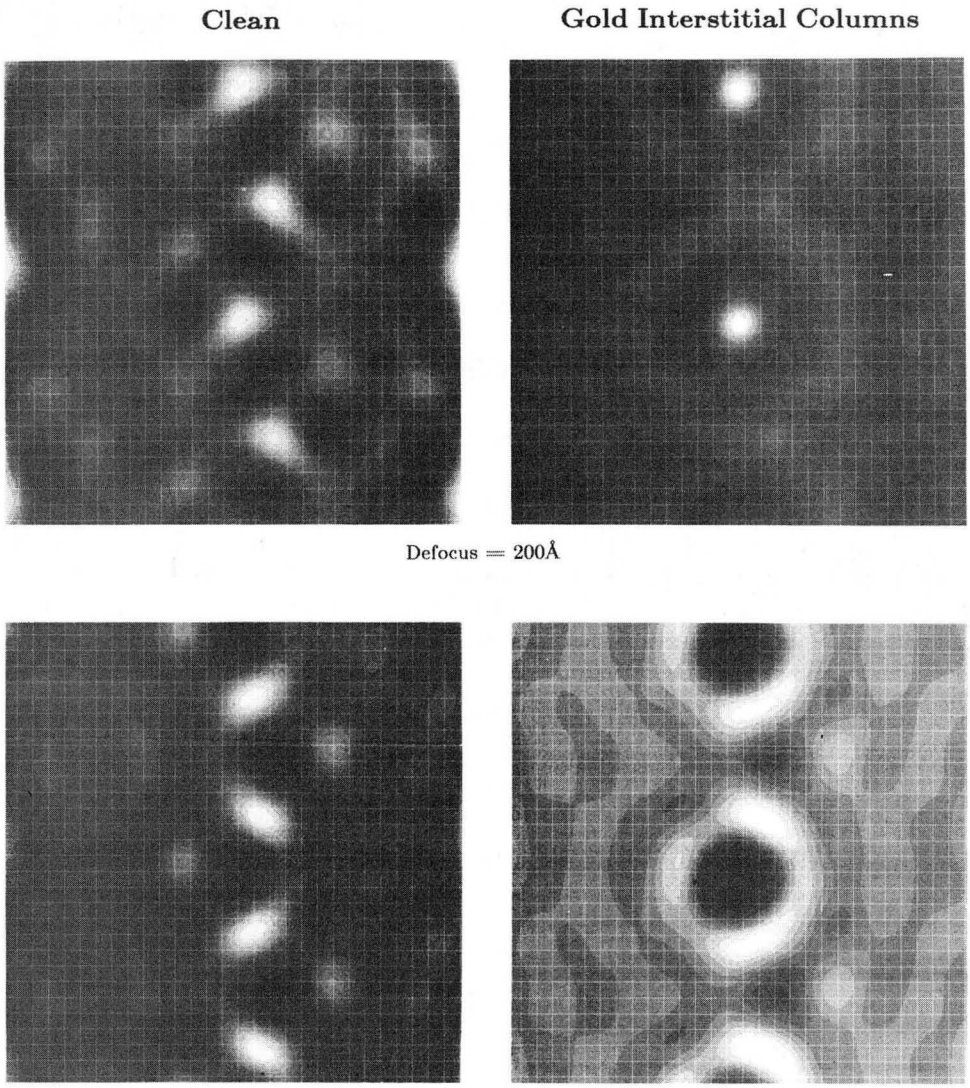

Fig. 7-24 Diffuse simulated images at optimum thickness (ξ) and defocus values for detection of impurities. In each image on the right, two cores (7-rings) contain 8 gold atoms (located at white spots in the top image and at the large dark spots in the bottom image) while the other two cores contain a single gold atom in the fifth slice.

XBB 857-5493

greatly in intensity. This is made particularly clear by comparing the 10% gold columns to the single gold atom sites. Since the greyscale has been reset to accomodate the much brighter 7-ring columns containing 10% gold, the other two 7-rings are now nearly lost in the background. At -660Å defocus, black 7-rings (left) become far "blacker" with 10% gold (right), replacing the white spots of the clean image as the visually dominant feature. Contrast values at this defocus are given in Table 7-4.

Two thicker samples at Scherzer defocus, serve to demonstrate the variety of contrast features which can occur (fig. 7-25). The 7-ring spots have switched back to white though addition of gold again reduces the intensity of these spots. At 333.9Å, this intensity reduction is so great that the 7-ring site is now represented by a black spot while two satellite white spots, roughly above and below, have appeared. This may be observed by comparing the central white spot in the image on the left to the same region of the right-hand image. At the thicker sample value of 383.8Å (100 slices), a less drastic reduction in spot intensity is found. The extrema values at the 7-membered rings are given in Table 7-5 for comparison.

Σ9 Contrast (Thickness=ξ)		
Clean	1 Au Atom	10% Au
33.9%	39.8%	117.5%

Table 7-4: Diffuse contrast values for optimum thickness (288Å) and defocus (Scherzer) of the Σ9 model, left, and with gold in interstitial, core sites, right. The single gold atom (second entry) is in slice five, while the 10% gold column has gold atoms in slices 5,15,25,...etc.

Silicon Σ9 Grain Boundary

Diffuse Simulated Images

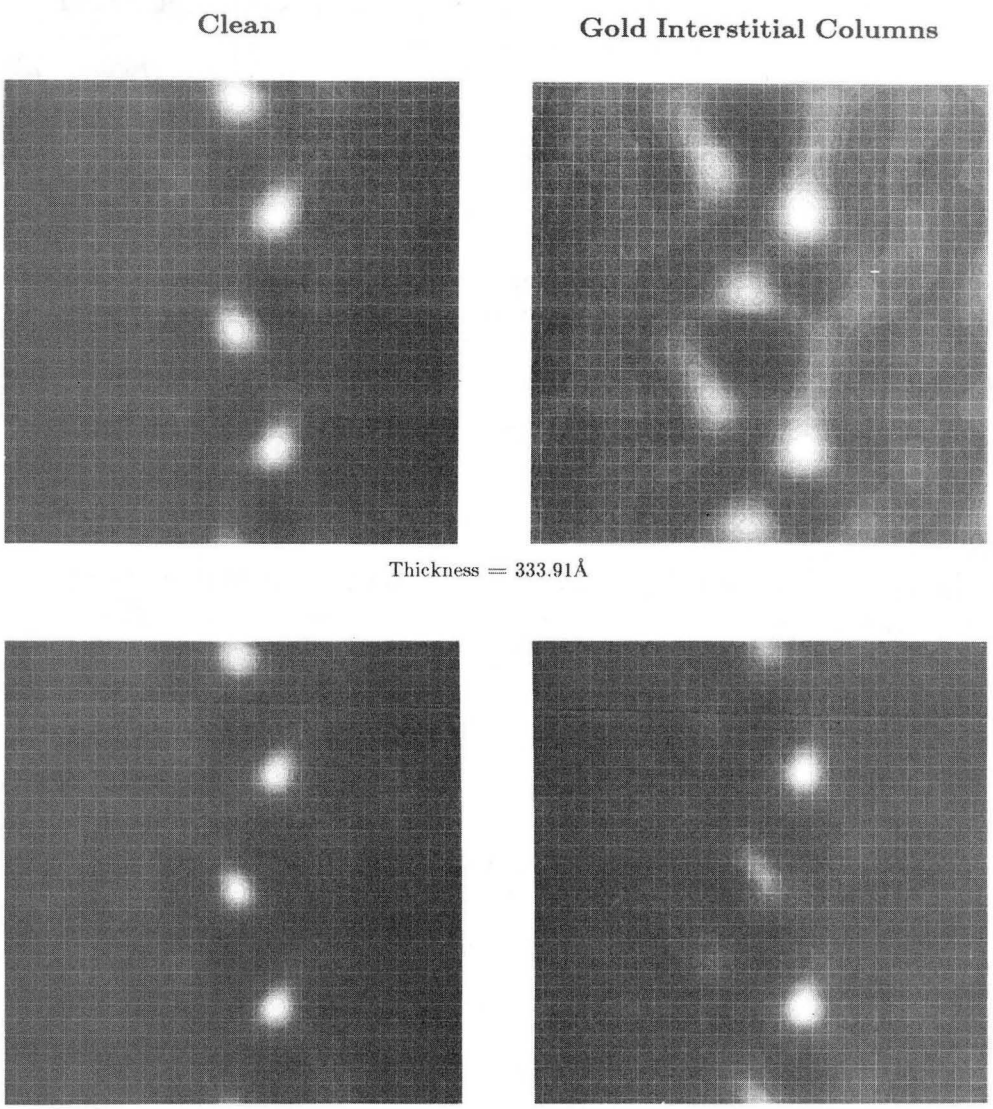

Fig. 7-25 Diffuse simulated images at two relatively large thicknesses of the Σ9 grain boundary model (left) and the model containing gold interstitials (right). Two grain boundary repeat units (vertical) appear in each image.

XBB 857-5492

Extrema Intensity Values at 7-Ring Site				
Thickness	Clean	1 Au Atom	10% Au	Background
287.9Å	.655	.615	.124	.790
333.9Å	.959	.923	.219	.648
383.8Å	.786	.784	.610	.256

Table 7-5: Extrema intensity values in neighborhood of Σ9 zigzag model 7-membered rings (i.e. segregation site). Objective aperture radius is .26Å^{-1} (JEOL 200CX). The background intensity is found from a defect free though otherwise identical simulation.

Discussion

Clearly, carefully controlled HRTEM lattice and diffuse imaging have the theoretical potential for obtaining chemical information from crystalline defects. Image contrast effects due to defect strain fields and due to impurity species are of similar magnitude, naturally depending on the atomic weights, concentrations, and strain fields present.

Impurity contrast effects in defect strain fields can be predicted on the basis of simulations of impurities in otherwise perfect crystalline material. However, strain field diffuse image contrast cannot be predicted simply on the basis of identification of regions of relatively high and low crystal projected potential (e.g. the Σ9 5-rings and 7-rings, respectively). Systematic comparison of experimental and calculated images is required for impurity information deconvolution.

In addition, optimum conditions for maximal effect of diffuse scattering in both lattice and diffuse images appears to hold significant potential for investigating the atomic configurations in defects, or at least distinguishing between potential model

structures. So far, this point has apparently been missed in HRTEM studies of defects where emphasis has been placed on obtaining weak-phase-object or projected-charge-density type images which possess one to one correspondence with specimen structure (given the resolution limits of the microscope). Balanced against this, though, is the very big if concerning proper specimen alignment in the electron microscope. The low-index crystallographic pole must be within a tenth of a degree or so of the optic axis for interpretable image formation. As specimen thickness increases, this criterion grows even more stringent (as does the requirement of beam alignment along the optic axis). Whether these conditions can be met will depend on the specimens in hand and the dexterity and patience of the microscopist.

7.3. Conclusions

In summary, impurity atoms with Z higher than the matrix give diffuse images analogous to those of isolated atoms while species of lower Z give inverted intensity features. Diffuse scattering contribution to image contrast is maximized (with observable image intensity) at Scherzer defocus and specimen thickness of ξ, though a fairly broad range of thickness is acceptable (about 200-400Å for $<110>$ orientation at 200KeV). This may be utilized to investigate details of defect core structure. Deconvolution of impurity scattering from defect strain field scattering generally requires careful image matching. For greatest confidence, results should be obtained from a variety of thicknesses and defocus values. Fullest implementation of this technique will likely require improvements in methods of specimen and beam tilt alignment.

Under optimim diffuse imaging conditions, the detection limit is roughly 2 or 3 atoms lying in a column parallel to the beam, for arsenic and boron in silicon. Lattice

images yield approximately half as much contrast, i.e. minimum detectability of ~5 arsenic atoms. A single antimony atom should yield measurable contrast. In any case, there is a practical substitutional column concentration lower limit of about 1% given the requirements of specimen thickness. If a specimen is prepared from a sample of much lower impurity concentration, it is unlikely that even a single impurity atom would be available for observation. In addition, real specimens exhibit image effects arising from surface roughness and contamination which may be confused with internal defect contrast. This particularly limits the ability to detect single impurity atoms.

More optimistically, it should be noted that the objective aperture was *not* optimized in the calculations. A radius of .26Å^{-1} was used (corresponding to a production JEOL 200CX) while the first order Bragg spots actually lie at .32Å^{-1}. Hence, for extensive studies, one should install an aperture of optimum radius or possibly an annular ring to include diffuse scattering beyond these Bragg beams. Also, as for isolated atom imaging, contrast may be enhanced by increasing Z *and* by increasing voltage.

Dark field techniques - either with tilted beam or a central beam-stop - also hold some promise for impurity imaging.[69],[70] However, these approaches are more likely to introduce anamolous image features and are much more difficult for calculations.

Questions of contrast optimization aside, the salient goal remains the observation of impurities at crystalline defects. Since increasing impurity contrast also generally increases strain field diffuse scattering contrast, experimental studies would require impurity concentrations of about 5 to 10% in the case of arsenic columns in a silicon defect. An impurity free sample (or one of differing concentration) should also be used

as a control.

Lastly, systematic application of impurity imaging will likely require a video pickup system attached to the microscope with direct digitization of the image and storage in an image processing computer system. Image intensity arrays may then be precisely evaluated and compared with calculated images. Additionally, simulations should utilize 256 X 256 arrays for accurate calculations of the widest possible variety of defects and impurity species.

CHAPTER 8

HRTEM of Silicon Σ9 and Σ13 GB's

The focus here shifts to the information HRTEM can provide on tilt grain boundary core structure at medium- and high-angle misorientations. Here, the dislocation cores are too close to be observed by strain contrast techniques. A limited number of studies have appeared.

Krivanek *et al.* made the first application of HRTEM to high-angle grain boundary core structural analysis in 1977.[72] A vapor-deposited germanium Σ9 boundary was found to be consistent with Hornstra's zigzag model by comparing an experimental image of a very thin specimen to an out-of-focus picture of a plastic model. In 1983, Vaudin *et al.*[34] evaluated the structure of a vapor-deposited silicon Σ27 boundary concluding that it contained structural elements from the Σ9 zigzag model (as hypothesized by Hornsta[30]). In 1981, in the field of metals, Ichinose and Ishida examined boundaries in gold samples produced by evaporation onto <110> oriented rock salt,[73] while in 1982, Penisson *et al.*[74] studied the dislocation content of a Σ41 boundary in molybdenum.

None of these studies utilized image simulation comparisons to aid in structural analysis. This limited the number of conclusions concerning core atomic configurations.

Recently, the first work involving systematic experimental image analysis supported by image simulation was reported by d'Anterroches and Bourret.[75] They

examined the Σ3 twin in silicon and the Σ9 <110> tilt boundary and the Σ25 and Σ41 <100> tilt boundaries in germanium. (Note that germanium is experimentally advantageous due to its slightly larger lattice parameter). However, image simulations were only possible for the Σ9 boundary due to the necessity of imaging the <100> tilt boundaries at higher passbands in the microscope employed in the study (a JEOL 200CX). These researchers feel that the available values for microscope parameters are too inaccurate for simulations at such defocus settings.

In the following, the core structures of the Σ9 and Σ13 grain boundaries in silicon are evaluated with experimental images and companion simulations.

8.1. Experimental Considerations

The bicrystals studied were grown by the Czochralski method at Crystal-Tec (Grenoble, France). The Σ9 bicrystal was 10 Ωcm phosphorus doped and the Σ13 was 1 Ωcm boron doped. Microscope specimens were prepared from 2.3 and 3.0mm discs cut normal to the tilt axes. The Σ9 specimens were observed in a JEOL 200CX microscope (2.4Å Scherzer resolution) operating at 200KeV while the Σ13 boundaries were imaged with the JEOL ARM-1000 at 800KeV (1.7Å resolution). The ARM has been adjusted for maximum brightness at this voltage while the small loss in resolution (compared to that at 1000KeV) is more than compensated for by a reduction in knock-on damage. All high resolution images were taken with axial illumination. The nature of the information extracted from the micrographs is outlined in the following.

Rigid body translations- High-resolution TEM provides a direct means of measuring the relative translation between the two crystals comprising a grain boundary. As discussed in Section 3-2, this information is essential for evaluation of bicry-

stal symmetry and aids in identification of possible core configurations. Rigid body translation measurement techniques are discussed in Appendix B. For the present work, the chosen method is a variation on that of d'Anterroches and Bourret.[75] A perfect crystal grid of scale identical to that in a grain boundary micrograph is prepared, aligned with the lattice image on one side of the boundary, and allowed to overlap the other side. The relative translation is measured in the overlap region with an accuracy of approximately $\pm.2$Å. A translation of $\frac{a}{4}<111>$ is sought (to see if the bicrystal is based on one of the two possible CSL's) plus any additional displacement is measured. Note that translations in the projection direction cannot be observed.

Dislocation Content- Burgers vectors may be directly determined from HRTEM images by drawing Burgers circuits around a dislocation core, assuming a suitable path is available. This is not possible for the high-angle $\Sigma 9$ boundary though it is for the medium-angle $\Sigma 13$ grain boundary. Of course, any Burgers vector component in the direction of the projection (the screw component) goes undetected.

Secondary dislocations change the length of the grain boundary repeat unit. For this reason, they may be detected by simply examining a grain boundary image for any such variations.

Core structure- The final, and highest, level of information to be gleaned from an image is the atomic configuration in the core. As previously discussed, this information content is derived from diffuse scattering. Interpretation is only possible in weak-phase-object type images (to the resolution limit) or by comparisons with calculated images (always desirable). The latter method is employed in the following. Thickness was estimated from thickness fringe contours. For this purpose, effective

extinction distances were calculated with the simulation programs by examining the beam intensities over a range of thicknesses for a perfect crystal (fig. 7-4 and fig. 8-1). Defocus values are determined from optical diffractograms taken from an amorphous edge or, when this is not possible, estimated with the minimum contrast condition as a reference.

The emphasis here is on core arrangement without concern for precise atomic coordinates. In principle, the latter can be a goal with HRTEM by adjusting atom positions used in image simulations until a best match is achieved. However, such applications remain speculative and require further investigation before their results may be deemed useful.

8.2. Σ9 Grain Boundary

Results

Figure 8-2 shows a large area HRTEM image of the Σ9 grain boundary. Its extreme regularity is striking for anyone familiar with metallic grain boundaries. This is a reflection of silicon's non-ductility at all experimentally encountered temperatures and the strong energetic preference for the {122} boundary plane. Since dislocation cores touch, Burgers vectors were not measured. Additionally, no secondary dislocations are observed since the misorientation is at the precise CSL value.

A higher magnification through focal series is given in fig. 8-3. A zigzagging structure is clearly apparent, its periodicity being that of the CSL (11.5Å, from geometrical considerations).

For reference, the two possible dichromatic patterns of the CSL are depicted in fig. 8-4. In the experimental images, a base rigid body translation of $\frac{a}{4}<100>_I$ is

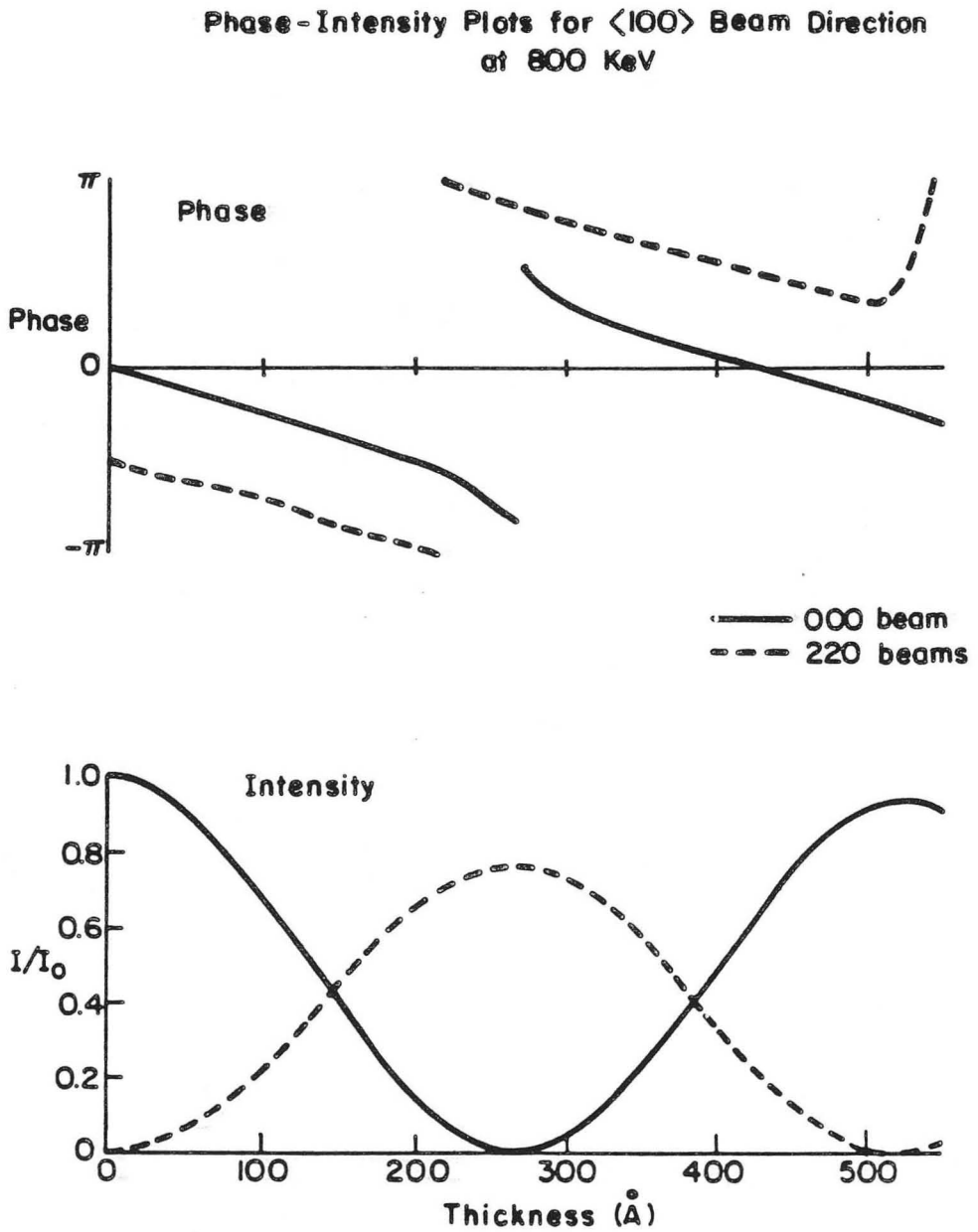

Fig. 8-1 Calculated phase intensity plots for image forming beams in <100> oriented silicon. The effective extinction distance is 512Å.

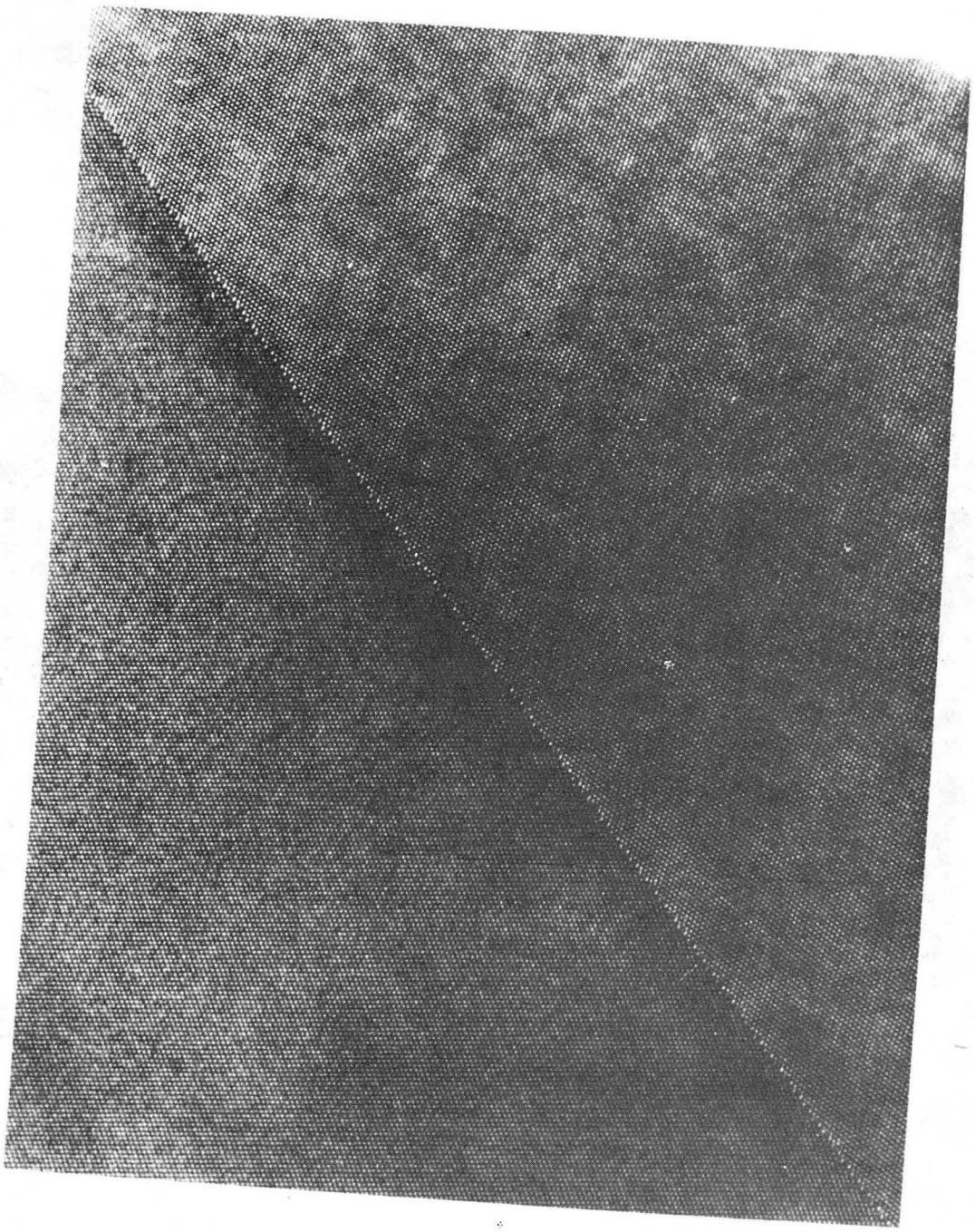

Fig. 8-2 This large area lattice image of a $\Sigma 9$ grain boundary demonstrates the strong energetic preference for a {122} boundary plane as reflected in the striking planarity of the defect.

XBB 858-6532

Σ9 Through Focus Experimental Images

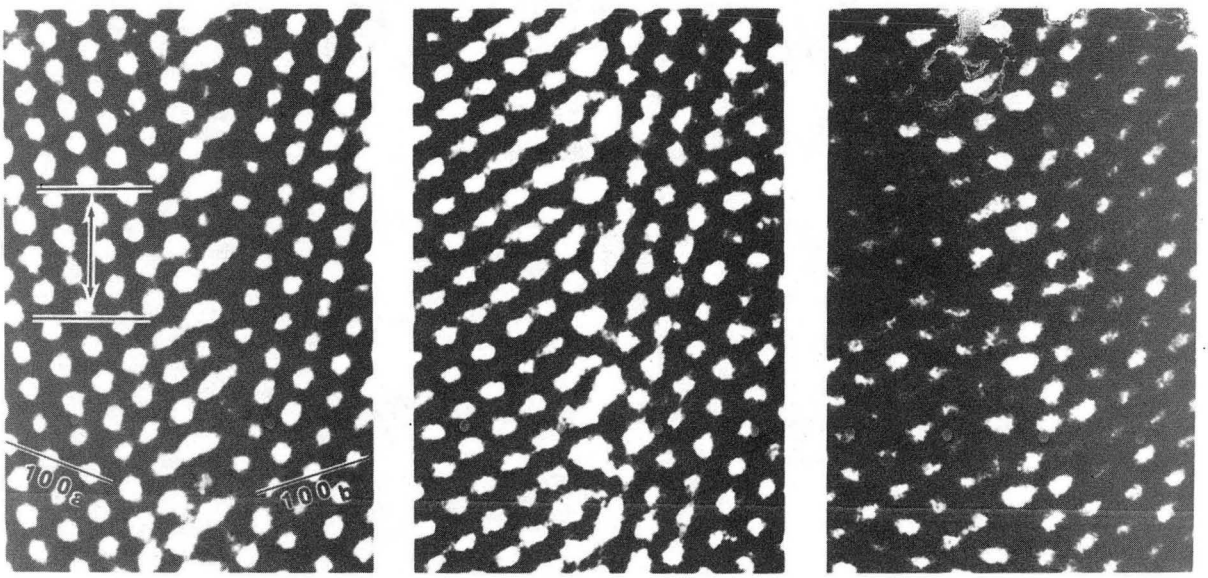

Fig. 8-3 Through-focus experimental images of a Σ9 grain boundary. The grain boundary period is marked in the image on the left (length $= \sqrt{4.5}a = 11.5$A). Alternating (zig-zag) pattern is evident at all defocus settings.

XBB 852-1564A

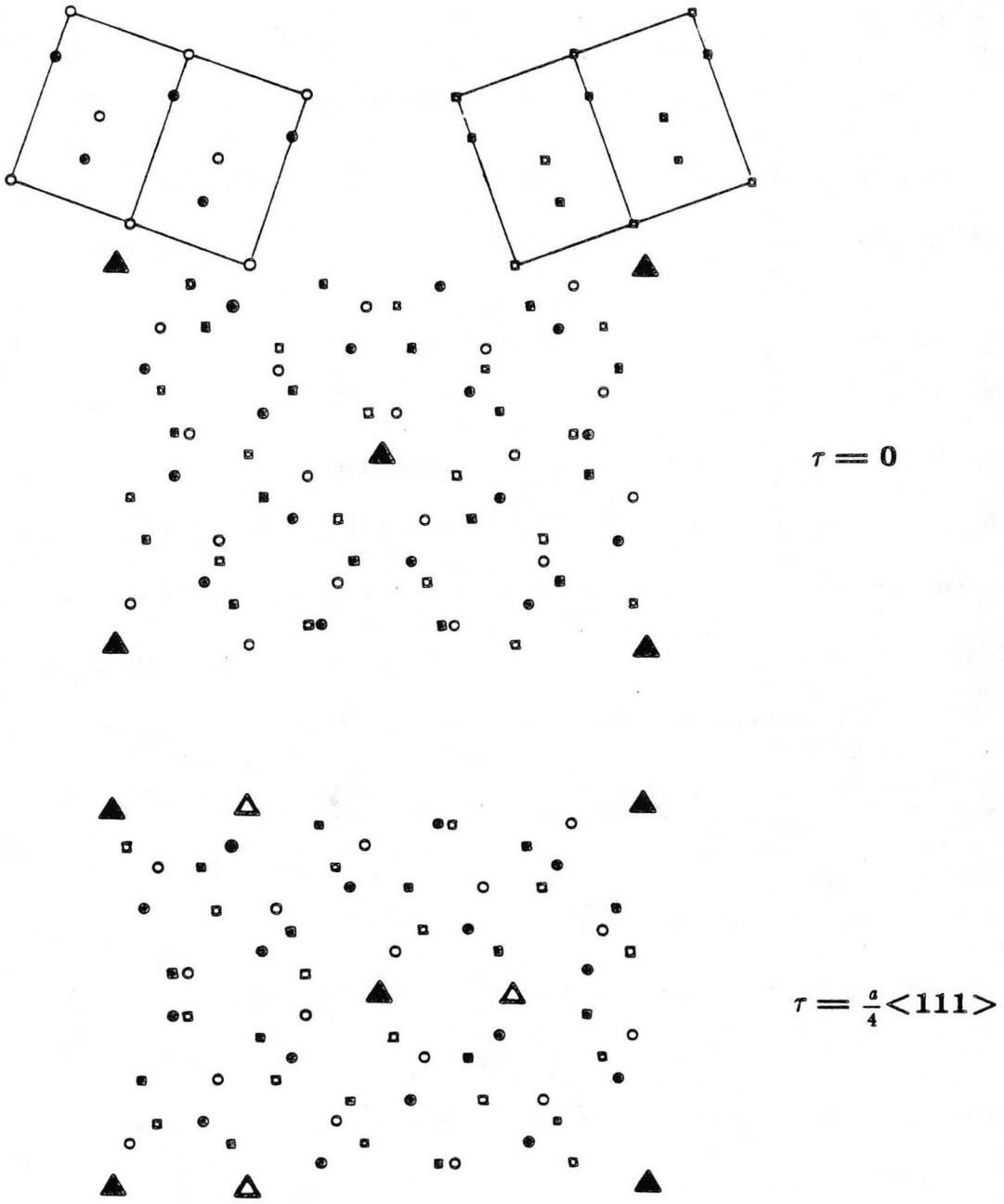

Fig. 8-4 Dichromatic patterns for the two diamond structure Σ9 CSL's. The <110> projected unit cells of the component grains are given contiguous to the upper figure. One grain has circular "atoms", the other square atoms. Filled markers are at different height from open markers. Triangles mark coincident atomic sites. The CSL with $\tau = \frac{a}{4}<111>$ has twice the expected number of coincident sites. However, these are additional coinciding *atomic* sites not *lattice* sites so the Σ value remains the same. This unusual occurence is an artifact of the diamond structure.

found plus an additional small dilation (normal to the boundary plane) of .4±.2Å. The former is the projection of an $\frac{a}{4}<111>$ displacement. This is simply the dumbell separation of the $<110>$ silicon projection (i.e. at CSL sites, white atoms of "upper" dumbell positions are coincident with black atoms in the "lower" position). Hence, the bicrystal is close to the $\tau = \frac{a}{4}<111>$ CSL.

This is the CSL of Hornstra's zigzag model. From visual inspection of the images, the bicrystal has a color-glide plane (equivalent to the above observation) which does not intersect lattice sites. This gives additional strong support to the zigzag model. In comparison, the $<100>$ Burgers vector (overlapping) dislocation model ($\tau = 0$, fig. 3-2), requires a color-mirror plane intersecting CSL sites in the grain boundary. So, prior to examination of core configuration, straightforward symmetry considerations eliminate the possibility of the latter structure while strongly suggesting the presence of the zigzag form.

For this reason, image simulations are limited to the zigzag model. The calculational unit cell is the same as that of fig. 7-19. This cell is repeated in fig. 8-5 (top) where dumbell atom pairs have been replaced with a single circle to help visualize the nature of the actual images by mimicking the resolution of the microscope. Companion experimental and simulated images at two defocus values are given in fig. 8-6. Good matching is achieved, though there are some noticeable differences. The alternating Lomer dislocation core units have different appearances, that is, "zig" units are different from "zag" units. From symmetry considerations, they should be identical. In particular, at -500Å defocus (black atoms, white tunnels), the simulation predicts white spots in the 5-ring tunnels (also see fig. 8-5, bottom). This feature is much

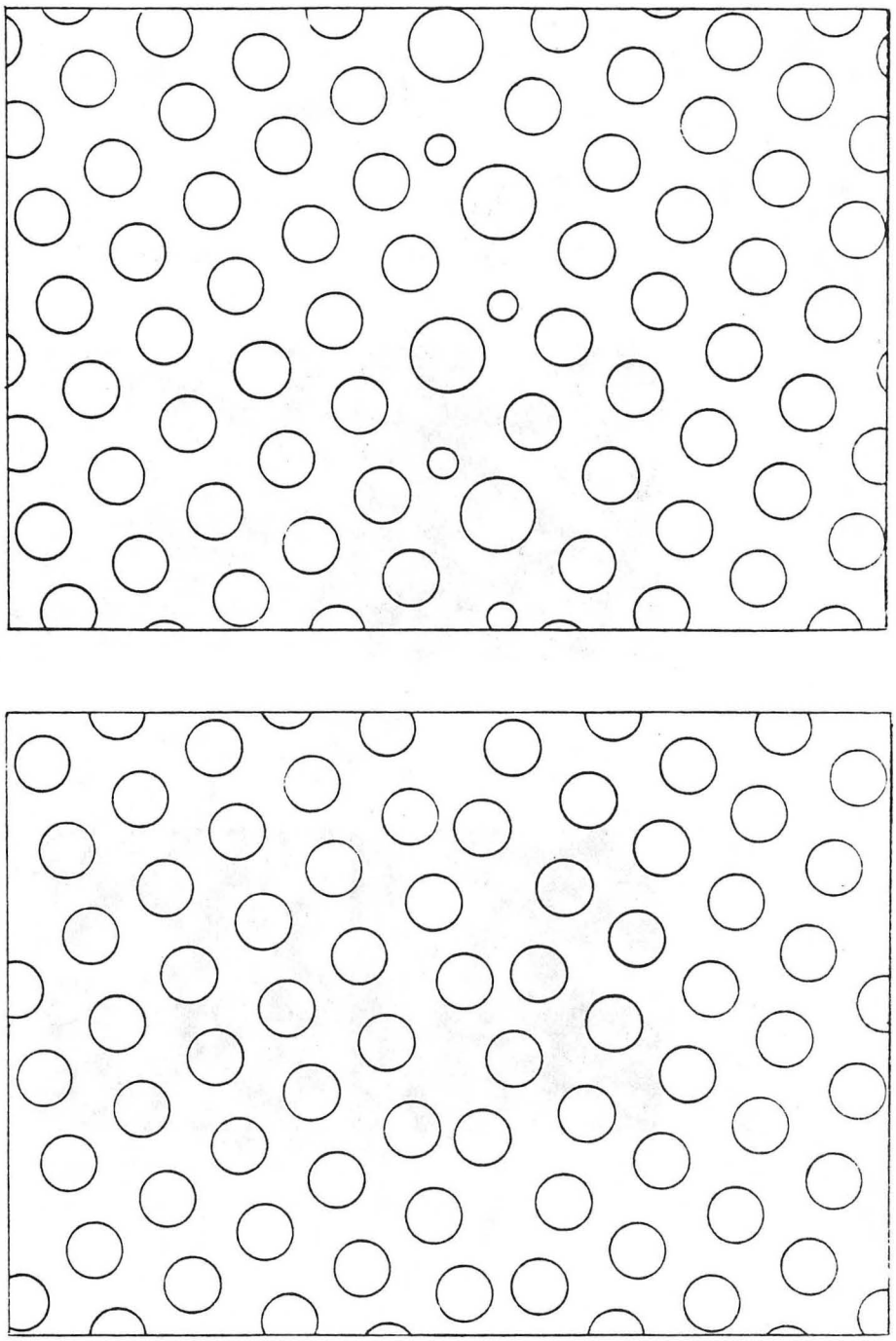

Fig. 8-5 $\Sigma 9$ calculational unit cell with atomic pairs replaced with circles (top) and with circles at tunnel sites (bottom). This is more suggestive of the images since the microscope cannot resolve the dumbell pairs. The top model may be taken as a first order guess for white atom image appearance while the bottom is best thought of as white tunnels - this is easier to visualize than black atoms.

Σ9 Images

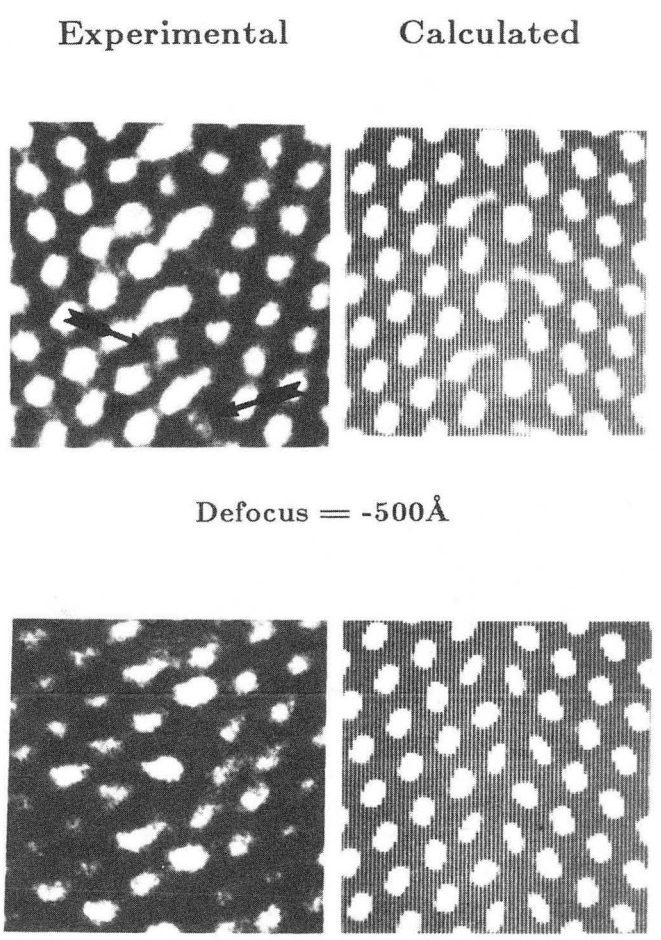

Fig. 8-6 Companion experimental and calculated images of a Σ9 grain boundary at two defocus values and 65Å thickness for the JEOL 200CX. Atom positions are black at top and white at bottom. Two repeat units are given in each image for clarity. Matching is fairly good, though "zig" units are not identical to "zag" units in the experimental images. In particular, at -500Å defocus, the simulated images predict a white spot in the 7-membered ring. This feature is clearly visible in only one of the above two units (indicated with arrows in the lower period of the experimental image).

XBB 858-6720

brighter in zig than in zag units (marked with arrows). Asymmetry might arise from a small beam or crystal tilt misalignment. However, introduction of typical amounts of residual beam and/or crystal tilt in simulated images failed to reproduce the experimental features. Other experimental effects can alter the appearance of the image. Varying etching rate at the boundary, impurities in the core, statistical fluctuations in the electron beam, and surface irregularities, contamination, and oxide layers[76] may perturb the image. The first two would have an equivalent effect on zig and zag units while the remainder produce random noise in the image. Some noise is apparent in the images, however, the features described above appear regularly over large lengths of grain boundary.

Discussion

The silicon Σ9 grain boundary is similar in structure to the Hornstra zigzag model with a small dilation normal to the boundary plane as expected from published observations on germanium grain boundaries. However, the precise location of atoms in the core remains an open question. In particular, the differing appearance of the zig and zag units is surprising. A similar variation is observed in the germanium Σ9 images of d'Anterroches and Bourret[75] though they do not comment on it. However, they point out that for their image simulations, atoms in the model core were moved about to best match the experimental images. Indeed, their simulated images have an asymmetry in the core unit appearance: apparently the adjustments to the zig units did not mirror those to the zag units. No physical basis is offered for this model. This apparent goal of obtaining a model with best simulated image matching may be justified on the assumption that a simple knowledge of atom positions will eventually

be of use in calculations of electronic structure. Unfortunately though, they do not give the atom positions used for the simulations.

Such attempts at modeling core structure are somewhat hollow if they are detached from the chemistry underlying the atomic configuration. It is likely one could match any experimental image given enough juggling of atoms in the defect core, but it is also important to know why this arrangement is preferred.

Additional features which they are unable to match are suggested to arise from impurities in the boundary. This is quite possible in light of the discussion of the previous chapter.

To illustrate the symmetry of this bicrystal, four unit cells of the CSL with core bonds included are depicted in fig. 8-7. Note that the core structural units are related by a color glide plane. The additional dilation experimentally found for the bicrystal preserves this symmetry.

8.3. Σ13 Grain Boundary

Results

For $<100>$ tilt boundaries, a translation of one grain by $\frac{a}{4}<111>$ produces no observable change, in projection. In effect, such a translation shifts the crystal up/down by half the unit cell dimension. The τ=0 state corresponds to Hornstra's edge dislocation pair model for $<100>$ tilt grain boundaries while $\tau=\frac{a}{4}<111>$ leads to the 45° dislocation model. Aside from this ambiguity, no additional τ was detected in the images.

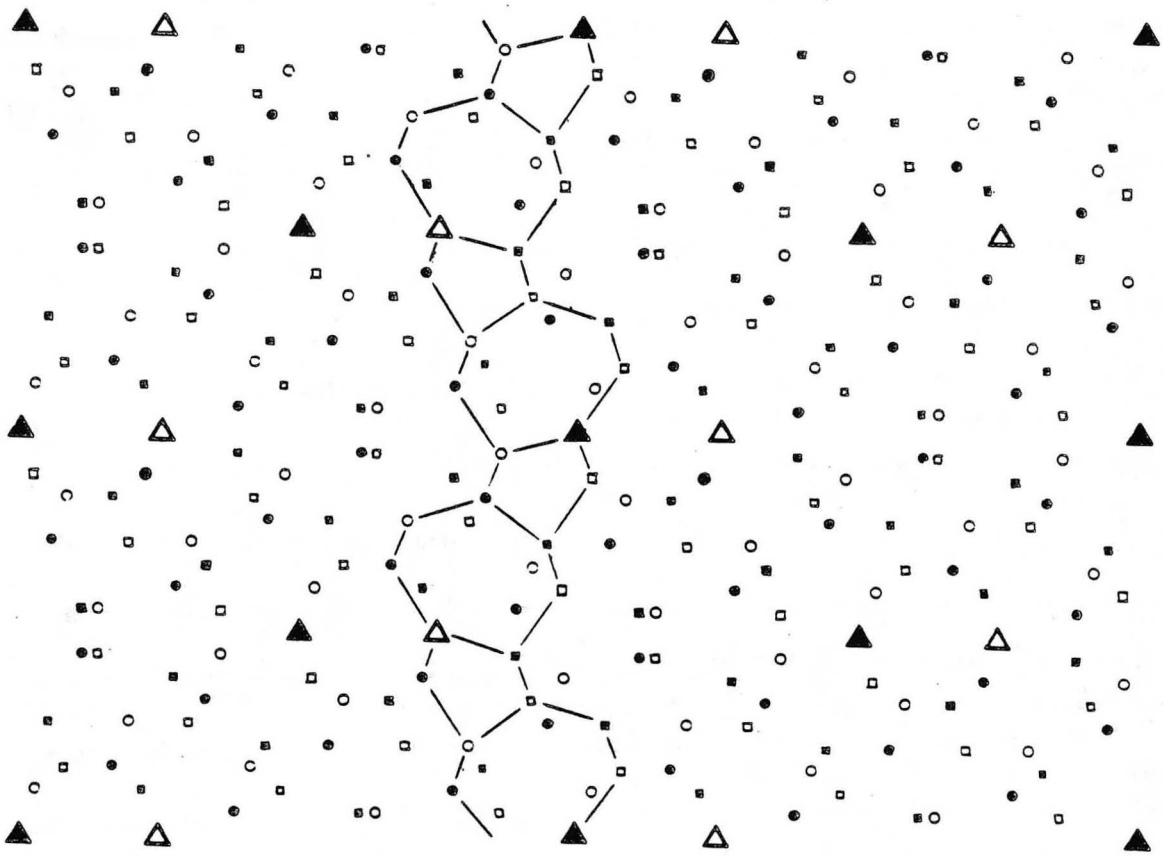

Fig. 8-7 Four unit cells of the $\Sigma 9$ $\tau = \frac{a}{4}<111>$ dichromatic pattern. This pattern leads directly to the zigzag model as indicated by the bonds represented with lines in the figure. Note that the grain boundary core samples both types of coincident atomic sites. This is a reflection of the boundary's color-glide symmetry.

In this medium-angle grain boundary, a Burgers circuit could be drawn for one period (fig. 8-8), giving the projected vector $a\,[010]_I$. The core structure of this defect is spread over the repeat distance ($\sqrt{6.5}\,a = 13.8$Å). Studies on low- and medium-angle grain boundaries in gold have revealed $a\,[010]$ edge dislocations,[77],[78] though the core spreading observed here was beyond their resolution limit. The grain boundary period may then be described as possessing a dislocation of Burgers vector $a\,[010]_I$. The simple $\mathbf{b}^2$ estimate of dislocation energy gives the same value for this dislocation as for the dislocation pairs mentioned above. Hence, without the availability of more fundamental calculations of core energy, both options are possible.

The two Hornsta models (fig. 3-5) include two identical (in projection) 45° dislocations or two mirror related edge dislocations per repeat unit, which lead to the same net Burgers vector. However, edge dislocations are inconsistent with features in the images. Since 45° dislocations are identical in projection, Hornsta's second model should give half the CSL period. This is not observed, though the images do suggest a pair of 45° dislocations associated with some additional defect. The features might also be accounted for by the dissociation of an $a\,[010]_I$ dislocation into two partial dislocations of $\frac{a}{2}[010]$ bounding a stacking fault.[79] However, this stacking fault has been demonstrated to lead to large distortions in the covalent bonds of the diamond structure.[80]

D'Anterroches and Bourret also observed $a\,[010]$ dislocations with spread cores in $\Sigma 25$ and $\Sigma 41$ boundaries in germanium. Though they could not discern details of the core configuration, geometrical considerations suggested the possibility of closely spaced pairs of 45° dislocations. Again, on energetic grounds, one would expect the

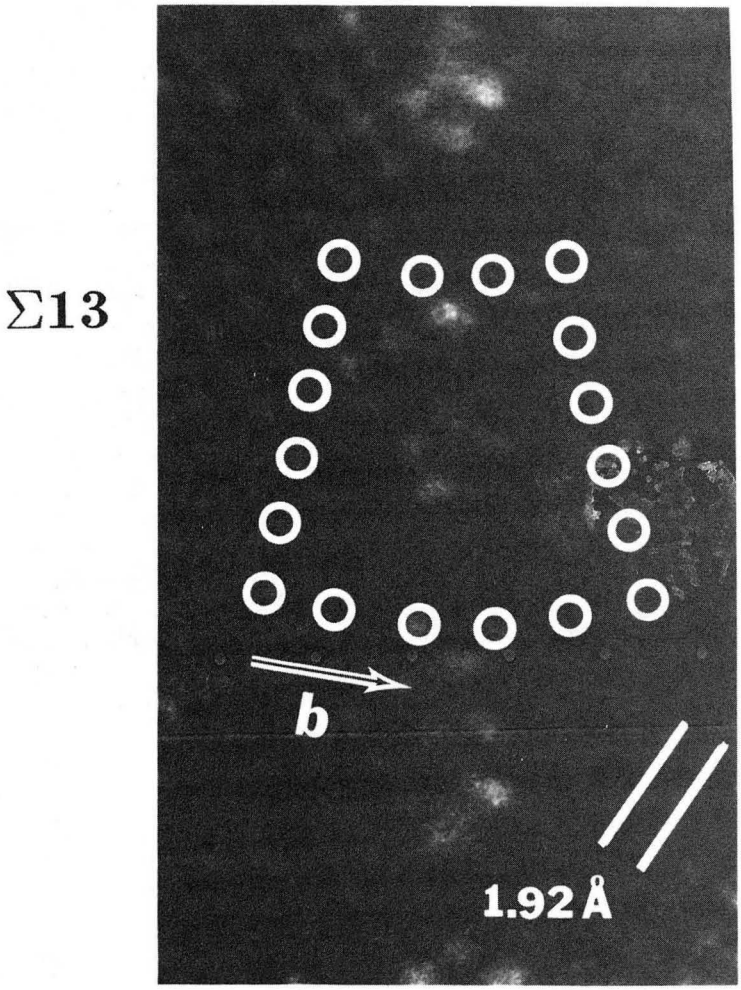

Fig. 8-8 Lattice image of a Σ13 grain boundary with Burgers circuit superimposed, giving a Burgers vector of $a <100>_I$. The circuit encloses one period of the grain boundary (length $= \sqrt{6.5}a = 13.8$Å). The {110} planar spacing is indicated.

XBB 858-6719

simple 45° dislocation model to have uniformly spaced dislocations. They suggest that a 45° dislocation dipole might be present in each period as a stabilizer. (A dislocation dipole is a parallel pair of dislocations with equal and opposite Burgers vectors.) This conceivably could reduce the strain energy arising from the screw components of the 45° dislocations in the simpler model.

Applying this suggestion to the Σ13 grain boundary, a model was constructed for simulations (fig. 8-9). For this grain boundary, the Hornstra model 45° dislocations are at minimum spacing without touching. The addition of the dipole in each period accounts for the observed periodicity, but does not affect the expected spacing of the "fundamental" dislocations.

Experimental and computed image comparisons are given in fig. 8-10. Fairly good matching is achieved. As an additional test, simulations were performed for the two Hornsta models. They offer very poor matching.

Discussion

For the Σ13 grain boundary, the earlier geometrical considerations fail to give a full accounting of the image observations. Further explanation of the defect structure requires accurate calculation of core energy, something not yet possible. Qualitatively, boundary planes which require two sets of dislocations (Burgers vectors not normal to the boundary) have residual shear strain energy which may be reduced by additional defects.

Secondary dislocations were not observed due to the precise orientation of the grain boundary. Such a defect would simply add (or subtract) a perfect lattice unit of length $|\frac{a}{2}<100>|$ to a Σ13 repeat unit (fig. 8-11). The location of a secondary

Σ13 45 ° pair/45 ° dipole Model
Calculational Unit Cell

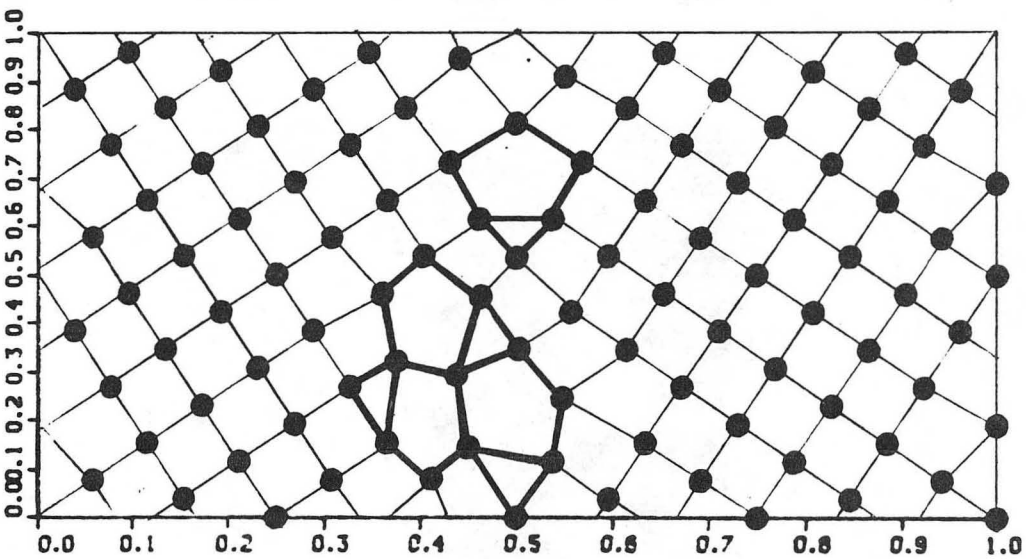

Fig. 8-9 Calculational unit cell of the Σ13/dipole model. One repeat unit contains two 45 ° dislocations associated with a 45 ° dislocation dipole.

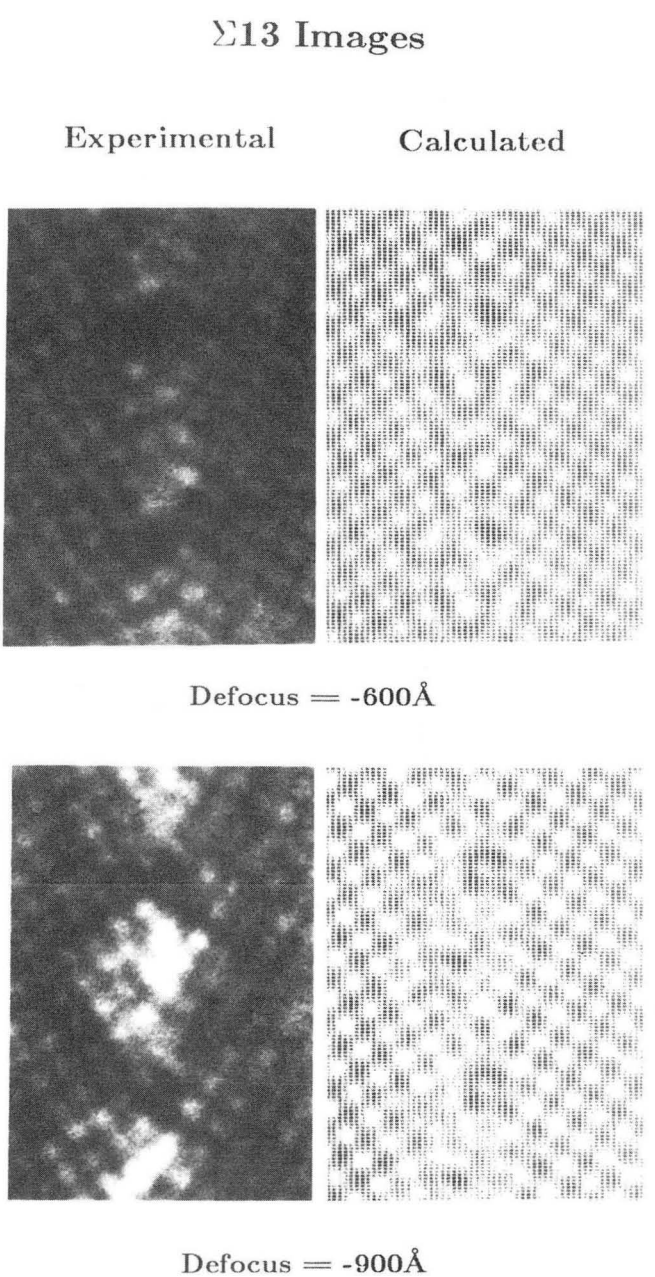

Fig. 8-10 Companion experimental and calculated images of a Σ13 grain boundary at two defocus values and 510Å thickness for the JEOL ARM-1000. Atom positions are black at top and white at bottom. Two repeat units are given in each image for clarity. Calculated images are based on the 45° dislocation pair/45° dislocation dipole model discussed in the text. Calculated images have the basic features of the experimental images though atom positions are not perfectly matched.

XBB 858-6721

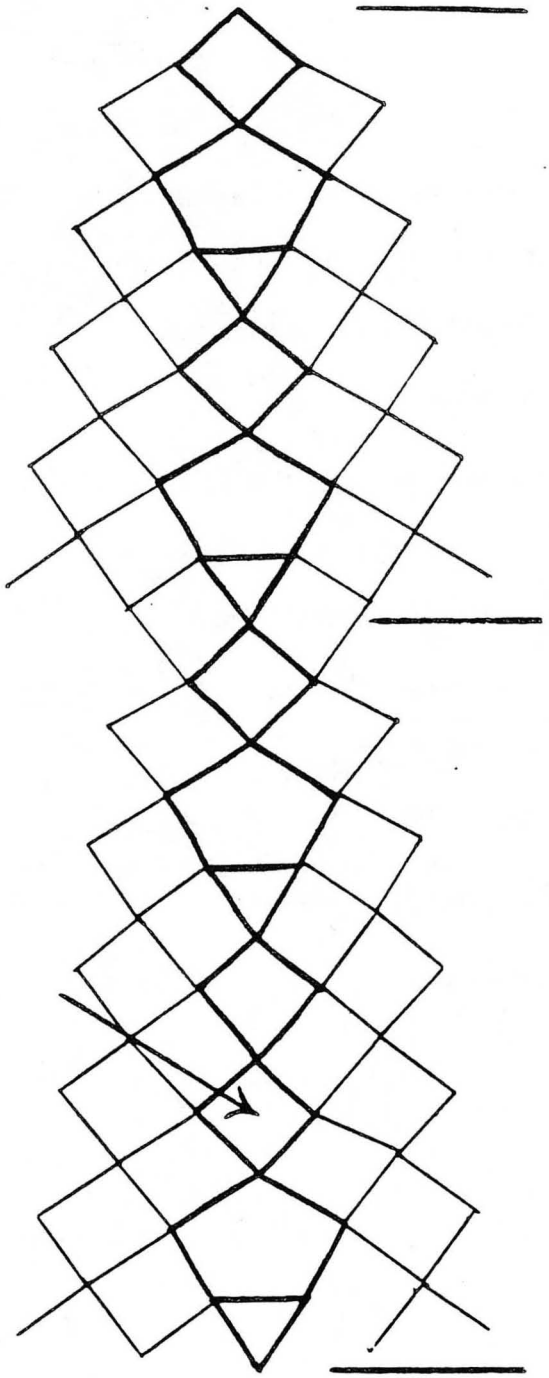

Fig. 8-11 Secondary dislocation model. The addition of an extra square perfect crystal unit (arrowed) to a Σ 13 repeat unit produces a Σ37 unit. From the O-lattice viewpoint, this foreign unit is a secondary dislocation. The local change in boundary plane produces a step in the Σ13 boundary, observable with strain-contrast TEM.

dislocation may then be thought of as spreading out over the entire repeat unit. In this case, the new unit is that of a $\Sigma 37$ {610} boundary. The boundary plane for $\Sigma 13$ is {510} so that, in effect, there is a local switch to a new boundary plane which introduces a small step in the grain boundary (too small to be observed by HRTEM). It is this step which produces the strain contrast in conventional microscopy images. However, since the dislocation cores are distinct in this angular range, the secondary dislocation introduces no truely new structural features.

As described in Chapter 3, over the whole misorientation range of $<100>$ tilt grain boundaries (0° - 90°) no overlap of dislocation cores is required. One may postulate that all $<100>$ tilt boundaries with a {100} median plane will consist of 45° dislocation pairs stabilized by a 45° dislocation dipole while {110} median planes will likely possess uniformly spaced identical edge dislocations. This suggests that there are no special $<100>$ tilt boundaries, that is, no cusps should appear in boundary energy versus misorientation angle. Such has been observed for NiO $<100>$ tilt boundaries while $<110>$ boundaries in the same material did exhibit energy cusps,[81] as expected.

8.4. Conclusions

To summarize, the $\Sigma 9$ {122} grain boundary is based on the CSL with $\tau = \frac{a}{4}<111>$, similar in configuration to the Hornstra zigzag model, though with some as yet unexplained loss in symmetry. An additional dilational translation of $.4 \pm .2$Å was found. The $\Sigma 13$ {150} boundary has no detectable translation and appears to be made up of 45° dislocation pairs stabilized by 45° dislocation dipoles. There is no theoretical substantiation for the existence of the dipole. This awaits energetic calcu-

lations.

Grain boundary periodicity is consistent with CSL predictions. Additionally, geometrical theories provide a good starting point for prediction of silicon grain boundary structure. Symmetry and bonding considerations serve to narrow the range of possibilities. More detailed predictions require continuing advances in the solid state physics of crystalline defects.

Semiconductor grain boundaries seem paticularly well suited to a description in terms of dislocation cores. This is particularly true in the case of <100> tilt boundaries, though the $\Sigma 5$ boundary (at which cores touch) should be investigated. The <110> tilt boundaries exhibit additional structural features not found in simple dislocations due to the necessity of overlapping cores at high angles of misorientation.

These grain boundaries may be described more elementally in terms of chair- and boat-shaped 6-membered rings and 5- and 7-membered rings. Introducing a step in the boundary plane would generally require a defect containing unpaired or reconstructed valence electrons. How applicable these notions are to more general grain boundaries remains a question for future research.

Experimentally, observation of silicon, or any semiconductor, is complicated while working at electron beam voltages much above 400KeV due to knock-on radiation damage. Observations of a given area at 800KeV are limited to two or three through-focal series (fig. 8-12). The standard high-resolution microscope of the future will likely have a video pickup system allowing work at reduced electron beam intensity and speedier microscope alignment. Direct linkage of this video system to a dedicated computer image processing/simulation system will permit more systematic studies, increase microscope efficiency, and permit extraction of more information from

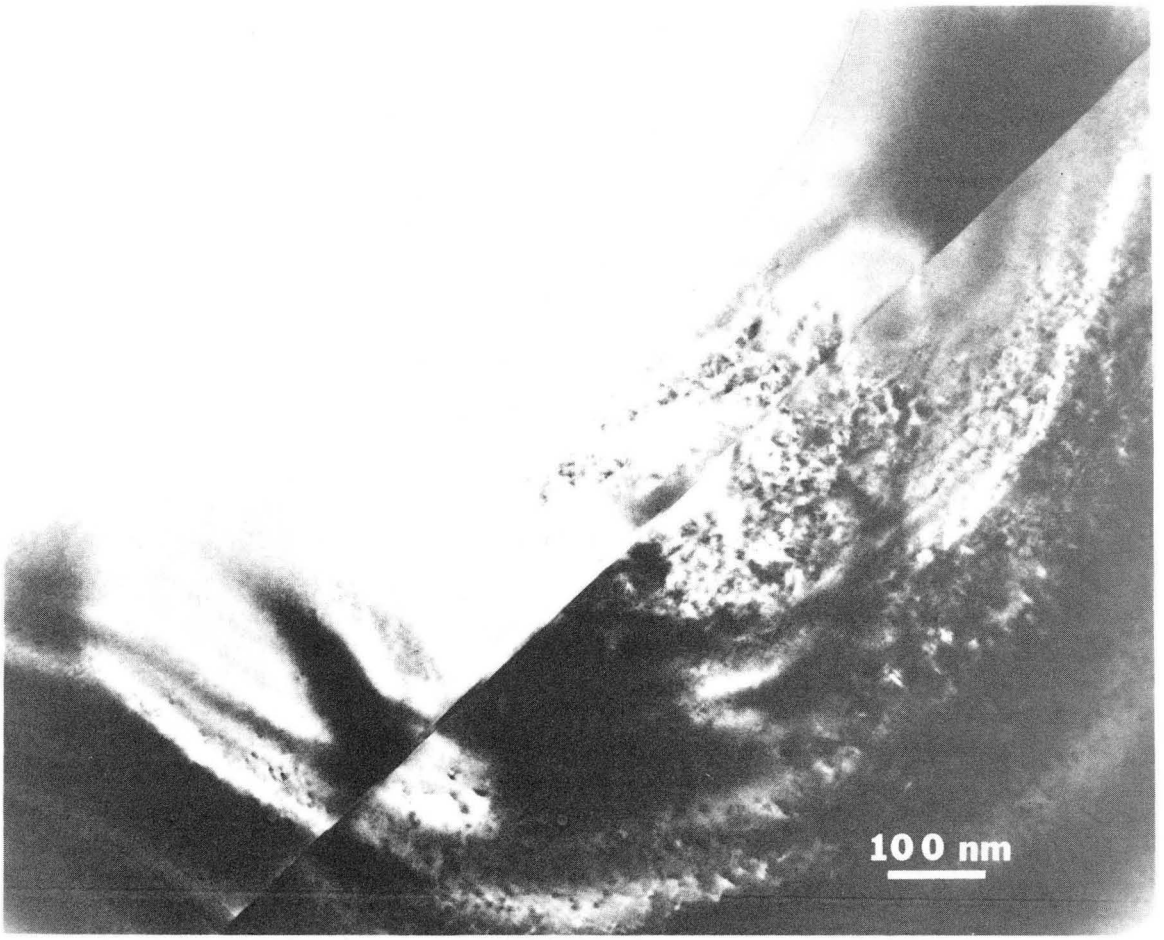

Fig. 8-12 This bright field view (180,000X) shows a Σ13 grain boundary which has been exposed to a focused 800KeV electron beam during three through focal series. Note the large area sustaining radiation damage. The knock-on damage threshold for silicon is approximately 400KeV.

XBB 858-6531

experimental images. Specifically, this will allow accurate measurements of rigid body translations using digitized images, processing of experimental images to reduce noise effects, rapid comparisons of experimental images with simulations side by side on a video monitor with quick adjustments to model atomic positions, and eventually programs which will search and compare files of simulated images with experimental ones, objectively selecting those of best fit. In short, the large quantity of information encountered is ideally suited for computer applications.

Appendix A

Bond Reconstruction in Silicon Crystalline Defects

The covalent bonds in semiconductors consist of σ-type bonding between electrons in sp^3 hybrid orbitals. Stress due to a defect induces significant strain in the neighboring material by bending and slightly altering the length of the covalent bonds. So long as the resulting energy increase of a bond is insufficient to destroy it, it may still be described as a covalent bond arising from sp^3 orbitals.

In some defects, notably the dissociated screw and 60° dislocations, some atoms in the defect core have broken bonds from the simple, geometrical point of view (see Ch.2). However, in a real material these unpaired electrons will likely undergo an energy reducing transformation from that of an unpaired sp^3 state.

Understanding possible energy reducing mechanisms requires a brief review of what organic chemistry tells us about covalent bonding. In silicon, as in carbon, the outermost potentially bonding state contains four electrons. In an isolated ground-state atom, two electrons occupy s orbitals (one spin-up the other spin-down) while two reside in p orbitals. (The three p orbitals require six electrons for saturation.) Alternate orbitals may be constructed by taking any linear sum of the s and p orbitals. Such combinations, called hybridized orbitals, exhibit high electron-density lobes in symmetric orientations (fig. A-1).[82] For example, the s plus a p orbital, designated sp, has two lobes extending in opposite directions, sp^2 has three coplanar lobes, while sp^3 has four lobes forming a tetrahedron.

Common Bonding Geometries

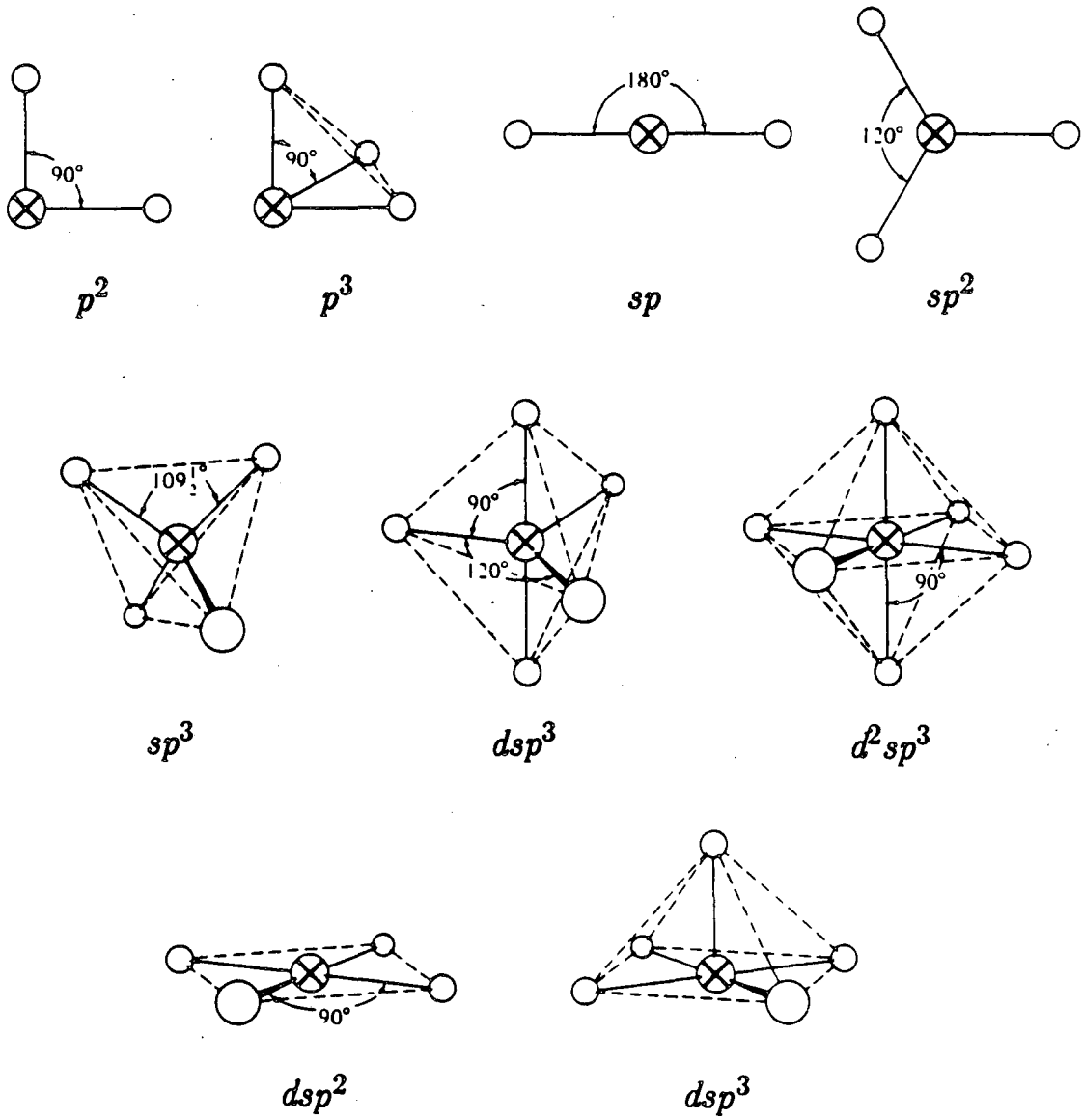

Fig. A-1 Bonding configurations arising from common hybrid and non-hybrid orbitals. Solid lines are bonds originating in the central atom. Dashed lines are for perspective (after Huheey.[82])

Depending on the structure of the particular material, any of the above orbitals may participate in bonding. The sp^3 hybrid appears in the diamond structure with its four nearest neighbor coordination, the shared pairs of bonding electrons also serving to fill the eight s and p derived states. Layered structures such as graphite possess Sp^2 bonds. With sp^2 bonding, the remaining p orbital lies perpendicular to the plane of the sp^2 orbitals. In sp bonding, the two remaining p orbitals and the sp bonding direction similarly are mutually perpendicular.

All the above are strong σ-type bonds. In addition, an extra p orbital may participate in a π-bond with a p orbital of a neighboring atom. The π-bond direction is perpendicular to the lobes of the original p orbitals and may therefore be parallel to a σ-bond, forming the double bonds common to organic molecules. Note that π-bonds are weak by comparison to the strong σ-bonds.

Bond resonance refers to a situation where equivalent positions are available for π-bonding to occur so that the bond location (i.e. participating electrons) may be said to "resonate" between the available sites. A paradigm for such is provided by benzene, schematically depicted below.

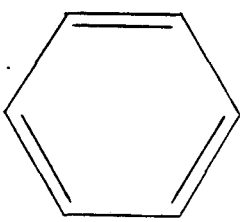

The three double bonds have six possible locations leading to two equivalent symmetric configurations. Barring the presence of side groups, the π-bonding electrons are expected to spend equal time in these two configurations. Quantum mechanically, the electron probability density is identical for all six bonds, so in reality it is best to

think of the six π-bonding electrons as smeared around the entire ring. Addition of a side group to one of the carbon atoms would shift the distribution of the probability density.

Returning to silicon dislocations and grain boundaries, one notes that Hornstra[7] and Hirth and Lothe[8] mention the expected reduction of dislocation core energy due to bond resonance, giving possible resonance locations. It is unclear what they have in mind since they suggest that an unpaired electron will participate in bond resonance with neighboring electrons. Perhaps they are suggesting that the location of the unpaired electron will shift, thus being "shared" by two or more locations. Our model considerations indicate that this requires large enough strains to prohibit such a "resonance".

On the other hand, bond *reconstruction* is often expected to reduce core energy, if geometrically permissible. Here, neighboring unpaired electrons form covalent bonds which involve small shifting of atomic position, changes in bond direction, and possibly the appearence of non-sp^3 hybrids. Alexander[83] has called these *substituting* bonds: they are known to exist in radiation defects.

There are two additional, though more hypothetical, mechanisms which may lead to energy reductions. First, coupling due to overlap of unpaired orbitals may occur. These however are not bonds, simply coupled unpaired spins. Another unproven possibility for dislocation core unpaired electrons is the formation of a half filled one-dimensional band, i.e. electrons spread along the core. The final option is that the unpaired electrons remain in strongly localized states.

Weber and Alexander[84],[85] have used electron paramagnetic resonance (EPR) to look for the above features in silicon dislocations. They ascribed their observations to 30° dislocation cores. Most unpaired electrons (~98%) appear to participate in substituting bonds. Those that remain seem either to be well localized or to couple, perhaps by overlap of p orbitals directed parallel to the dislocation line. In this last situation, the remaining three valence electrons of the core atom would then assume an sp^2 configuration. With annealing above 750° C, all core electrons appear to be in substituting bonds.

Appendix B

Rigid Body Translation Measurement Techniques

As discussed in Sec. 3-1, a knowledge of the rigid body translation of a bicrystal from the exact coincident position is necessary for evaluation of its symmetry and potential core configuration. A number of translation measurement techniques are available, their applicability depending on the bicrystal type and experimental conditions. Consideration here is limited to methods of subangstrom accuracy.

In principle, the most precise measurements are provided by the α-fringe technique.[86] This approach requires a common reciprocal lattice (**g**) vector for the formation of a two-beam bright-field image. Any rigid body translation component in the direction of **g** (normal to the scattering planes) produces stacking fault-like fringes in the image of an inclined grain boundary. A densitometer trace of these fringes is matched with a calculated fringe profile which, having form dependent on displacement, gives a value for one component of the translation. Hence, three non-coplanar common **g**'s are required for a full measure of the rigid body translation. Being based on an interference effect, the technique is potentially accurate to hundredths of an angstrom, though small **g** values are necessary for visible fringe intensity. In practice, inaccuracy in extinction distances used in the calculations and perturbation of the fringes due to inelastic scattering limits accuracy to $\sim$5% of the lattice parameter,[87] .26Å for silicon.

Other approaches rely on direct image measurements. If a reference crystal of suitable lattice parameter can be deposited on the bicrystal, the resulting Moire fringes

can provide precision to a tenth the planar spacing (again, an interference phenomenon). Unfortunately, no practical means of accomplishing this has been demonstrated to date. Barrel distortion of the projection lens obviates the option of placing a reference "lattice" on an actual lattice image.

D'Anterroches and Bourret[75] have obtained satisfactory results with direct measurements by a very simple approach. They trace the lattices on both sides of a grain boundary lattice image, allowing the tracings to overlap while remaining aligned with their respective grains. The displacement of the overlapping tracings is then measured. Based on many trials, an accuracy of about one tenth the point-to-point resolution is claimed.

In any event, measurements must not be taken too close to the boundary plane where strain fields are substantial, or too far, where specimen thickness and orientation may vary sufficiently to produce anomolous results. In addition, HRTEM provides no information about the translation component in the projection direction of the image.

Appendix C

Computer Programs for Defect Model Atom Postions

Dislocation atom positions are calculated with linear elastic theory. For grain boundaries, programs generate a rigidly rotated and translated bicrystal. Core atom positions must then be adjusted "by hand". Control cards are specific to the Control Data Corporation 7600. Graphics calls refer to IDDS graphics software.

Grain Boundary Program

```
GB,7,500.xxxxxx,xxx
MNF4.
FETCHPS,IDDS,ULIB,ULIBX.
FETCHPS,GPACBN7,VAR,VABN.
LINK,F=LGO,F=VAR,P=ULIB,X.
LIBRITE,SIGMA13,GBOUT,GBOUT,177.
FETCHPS,PLOTTER,GRAPHIC,GRAPHIC.
GRAPHIC,FN=FILM,FT=VA.
EXIT.
DUMP,0.
GRUMP.
FIN.
      PROGRAM BICRYST(OUTPUT,TAPE6=OUTPUT,FILM,GBOUT,TAPE1=GBOUT)
C     CREATES ATOM POSITIONS (UNSTRAINED) FOR TILT GB OF ANGLE THETA.
C
      DIMENSION X1(200),Y1(200),X2(200),Y2(200)
      DATA TATOM /4HSI  /
      DATA NATOM,NZ,OCC,Z,TISO,NANI,NIND /1,14,1.,0.,.3,0,0/
C
      COMMON /IGSZZZ/ ZMODE(200)
C
      EXTERNAL FONT2
C
      CALL MODESG (ZMODE,6,0)
      CALL SUBJEG (ZMODE,0.,0.,1.,1.)
      CALL OBJCTG (ZMODE,20.,30.,80.,60.)
C     FOR DOUBLE THE DEFAULT FRAME LENGTH USE@
C     CALL RSETMG (ZMODE,0.,0.,2.,1.)
C     CALL OBJCTG (ZMODE,10.,5.,190.,99.206)
C
      CALL VECIG (ZMODE,FONT2,0)
      CALL SETSMG (ZMODE,51,1.)
      ENCODE(3,1000,ICHAR)
      CALL SETSMG(ZMODE,84,ICHAR)
```

```
C
      S = SQRT(2.)
C     Following for Σ9, Σ13, and Σ25 respectively.
C     THETA = ATAN2(S,4.)
      THETA = ATAN2(1.,5.)
C     THETA = ATAN2(1.,7.)
      L = 0
      M = 0
      COSX = COS(THETA)
      SINX = SIN(THETA)
C
C     MASK SIZE, BB SHOULD BE A MULTIPLE OF THE GB PERIOD.
C     Use following for Σ9.
C     AA = 12
C     BB = SQRT(4.5)
C     FOR SMALLER UNIT CELL *2 MAY BE DROPPED IN THE FOLLOWING
C     Use following for Σ13.
      AA = SQRT(6.5)*2
      BB = SQRT(6.5)
C     Use following for Σ25.
C     AA = SQRT(12.5)*2
C     BB = SQRT(12.5)/2
C
C     SCALE FOR DO LOOPS
C     Use following for Σ9.
C     A = S/4.
C     B = .25
C     FOR SIGMA 13 AND 25 USE THE FOLLOWING
      A = .25
      B = .125
C
C     GENERATE FACE CENTERED POINTS
      DO 500 I=1,40,2
      DO 500 J=1,80,4
      DO 500 K=1,2
C
C     TWO ATOM BASIS
C     ELIMINATE DO STATEMENT IF SINGLE ATOM BASIS AND +IB-1 TERM
      X = (I-21+K-1)*A
      Y = (J-21+2*K-2)*B
C
C     ROTATE -THETA LEFT GRAIN (1), +THETA RIGHT GRAIN (2).
      XL = X*COSX + Y*SINX
      YL = -X*SINX + Y*COSX
      XR = X*COSX - Y*SINX
      YR = X*SINX + Y*COSX
C
C     SAVE POINTS IN MASK.
```

```
      IF (XL.LT. -AA/2 .OR. XL.GE. 0.) GO TO 300
      IF (YL.LT. 0. .OR. YL.GE.BB) GO TO 300
      L = L+1
      X1(L) = (XL+AA/2)/AA
      Y1(L) = YL/BB
C     SECOND WRITE FOR REAL SPACE PROGRAM, TWO BELOW
      WRITE (1,1010) TATOM,NZ,OCC,X1(L),Y1(L),Z,TISO,NANI,NIND
C     WRITE (1,1020) NATOM,NZ,X1(L),Y1(L),Z,TISO
  300 CONTINUE
      IF (XR.LT. 0. .OR. XR.GE. AA/2) GO TO 500
      IF (YR.LT. 0. .OR. YR.GE.BB) GO TO 500
      M = M+1
      X2(M) = (XR+AA/2)/AA
      Y2(M) = YR/BB
      WRITE (1,1010) TATOM,NZ,OCC,X2(M),Y2(M),Z,TISO,NANI,NIND
C     WRITE (1,1020) NATOM,NZ,X2(M),Y2(M),Z,TISO
  500 CONTINUE
 1010 FORMAT (A4,2X,I2,2X,5F10.7,10X,2I5)
 1020 FORMAT (I1,2X,I2,2X,4(F10.8,2X))
C
      CALL GRIDG (ZMODE,0.,0.,0.,0.)
      CALL POINTG (ZMODE,L,X1,Y1)
      CALL POINTG (ZMODE,M,X2,Y2)
      CALL EXITG (ZMODE)
      CALL EXIT
 1000 FORMAT(*$S0*)
C
      END
```

The following program calculates the atom positions for a split 60° dislocation (27Å separation), then masks an area around the 30° partial for image simulation input.

```
SI,7,500.xxxxxx,xxxxx
MNF4.
FETCHPS,IDDS,ULIB,ULIBX.
FETCHPS,GPACBN7,VAR,VABN.
LINK,F=LGO,F=VAR,P=ULIB,X.
LIBRITE,JR,SIOUT,SIOUT,177.
FETCHPS,PLOTTER,GRAPHIC,GRAPHIC.
GRAPHIC,FN=FILM,FT=VA.
EXIT.
DUMP,0.
GRUMP.
FIN.
```

```
      PROGRAM SI30(OUTPUT,TAPE6=OUTPUT,FILM,SIOUT,TAPE1=SIOUT)
C
      DATA A,B,C,NZ,OCC /3.838,5.428,3.838,14,1./
      DATA Z,TISO,NANI,NIND,EPS /0.,0.3,0,0,1.357/
      DATA TATOM /4HSI  /
C
      COMMON /IGSZZZ/ ZMODE(200)
      DIMENSION XX(500),YY(500)
C
      EXTERNAL FONT2
C
      AA = 23.707
      BB = 36.0
      L=0
      CALL MODESG (ZMODE,6,0)
      CALL SUBJEG (ZMODE,0.,0.,1.,1.)
      CALL OBJCTG (ZMODE,20.,20.,85.2,90.)
C
      CALL VECIG (ZMODE,FONT2,0)
      CALL SETSMG (ZMODE,51,1.)
      ENCODE(3,1000,ICHAR)
      CALL SETSMG(ZMODE,84,ICHAR)
C
C     3 SETS OF X/Y VALUES
   10 DO 900 M=1,3
      GO TO(20,30,40),M
   20 NX0 = 2
      NY0 = 2
      GO TO 100
   30 NX0 = 1
      NY0 = 6
      GO TO 100
   40 NX0 = 3
      NY0 = 10
C
C     X VALUES
  100 DO 800 ID=NX0,57,3
      IYC2 = 0
      NY = NY0
C
C     Y VALUES
  150 DO 700 JD=NY,49,12
      J = JD-2
      I = ID-2
C
C     SET D1, D2, AND SF VALUES
  200 IF (I-15) 270,205,210
  205 IF (J-24) 700,260,260
```

```
  210 IF (I-40) 220,215,290
  215 IF (J-24) 230,290,290
  220 IF (J-24) 230,280,280
  230 I = I-2
      IF (I-16) 700,280,280
  260 D1 =.0001
      D2 = .5
      GO TO 299
  270 D1 = .25
      D2 = .5
      GO TO 295
  280 D1 = -.25
      D2 = .5
      GO TO 295
  290 D1 = -.25
      D2 = -.5
  295 IF (I-39) 297,296,297
  296 D2 = .4999
      GO TO 299
  297 IF (I-40) 299,298,299
  298 D2 = -.4999
  299 CONTINUE
C
C FOR SHUFFLE CHANGE SITE B1 AND IN 205 24 TO 27
C
      X = I-15+D1
      Y = (J-23.5)/1.4142
C B is Burgers vector (1 for 30°, 2 for 90°)
      B = 1
C FOR SHUFFLE 23.5 TO 25.5
      DO 400 N=1,2
      UX = B*.15915*(ATAN(Y/X) + .63939*X*Y/(X*X+Y*Y))
      UY = -B*.05088*(.564*ALOG(X*X+Y*Y) + (X*X-Y*Y)/(X*X+Y*Y))
      GO TO(380,390),N
  380 UX1 = UX
      UY1 = UY
      X = I-39.5+D2
      Y = (J-23.5)/1.4142
      B = 2.0
      GO TO 400
  390 UX2 = UX
      UY2 = UY
  400 CONTINUE
      IF (I-15) 405,402,405
  402 X = (UX2+D2+I)
      GO TO 406
C
  405 X = (UX1+UX2+D1+D2+I)
```

```
 406 Y = ((UY1+UY2)*1.4142 + J)
C       PRINT IF >=0 AND <1
     IF (X-3.833)700,420,410
 410 IF (X-27.54)420,700,700
 420 IF (Y-4.8)700,500,430
 430 IF (Y-40.8)500,700,700
 500 X = (X-3.833)/AA
     Y = (Y-4.8)/BB
     WRITE(1,510) TATOM,NZ,OCC,X,Y,Z,TISO,NANI,NIND
 510 FORMAT(A4,2X,I2,2X,5F10.7,10X,2I5)
C
     L = L+1
     XX(L) = X
     YY(L) = Y
C
 700 CONTINUE
C       Y CYCLE TWICE/ SAME X VALUE
     IYC2 = IYC2 + 1
     NY = NY0 + 3
     GO TO(150,800),IYC2
 800 CONTINUE
 900 CONTINUE
C
     CALL GRID (ZMODE,0)
     CALL POINTG (ZMODE,L,XX,YY)
     CALL EXITG (ZMODE)
     CALL EXIT
1000 FORMAT(*$S0*)
C
     END
```

Appendix D

Calculational Unit Cell Atom Positions

Atom coordinates are given in terms of the A and B dimensions of the calculational cell. The origin of the cell is at the lower left corner.

Silicon Σ9 Zigzag Model (with interstitial sites)

A=32.56920Å B=11.51495Å C=3.838000Å
73 Atoms

.4950000	.8500000	(interstitial)	.4935842	.4486732
.5680286	.3500000	(interstitial)	.4519175	.6153399
.0352508	.7820065		.4658064	.7264510
.0491397	.8931177		.5127500	.0850000
.0074730	.0597843		.5277500	.1950000
.0213619	.1708954		.6805556	.0555556
.0908064	.2264510		.6111111	.1111111
.1046953	.3375621		.5972222	.2222222
.0630286	.5042288		.6388889	.3888889
.0769175	.6153399		.6250000	.5000000
.1463619	.6708954		.5502786	.5850000
.1602508	.7820065		.5352786	.6950000
.1185842	.9486732		.5833333	.8333333
.1324730	.0597843		.5694444	.9444444
.2019175	.1153399		.8055556	.0555556
.2158064	.2264510		.7916667	.1666667
.1741397	.3931177		.7222222	.2222222
.1880286	.5042288		.7083333	.3333333
.2574730	.5597843		.7500000	.5000000
.2713619	.6708954		.7361111	.6111111
.2296953	.8375621		.6666667	.6666667
.2435842	.9486732		.6527778	.7777778
.3130286	.0042288		.6944444	.9444444
.3269175	.1153399		.9166667	.1666667
.2852508	.2820065		.9027778	.2777778
.2991397	.3931177		.8333333	.3333333
.3685842	.4486732		.8194444	.4444444
.3824730	.5597843		.8611111	.6111111
.3408064	.7264510		.8472222	.7222222
.3546953	.8375621		.7777778	.7777778
.4241397	.8931177		.7638889	.8888889
.4380286	.0042288		.9861111	.1111111
.3963619	.1708954		.9444444	.4444444
.4102508	.2820065		.9305556	.5555556
.4796953	.3375621		.9722222	.7222222

.9583333 .8333333
.8888889 .8888889
.8750000 1.0000000

Silicon Σ13 45 ° Dislocation Model

A=27.67850Å B=13.83925Å C=5.428200Å
100 Atoms

0. .5000000
.5000000 .5000000
0. .6923077
.0384615 .8846154
0. .0000000
.0576923 .0769231
0. .1923077
.0769231 .2692308
.0384615 .3846154
.0961538 .4615385
.0576923 .5769231
.1153846 .6538462
.0769231 .7692308
.1346154 .8461538
.0961538 .9615385
.1538462 .0384615
.1153846 .1538462
.1730769 .2307692
.1346154 .3461538
.1923077 .4230769
.1538462 .5384615
.2115385 .6153846
.1730769 .7307692
.2307692 .8076923
.1923077 .9230769
.2500000 .0000000
.2115385 .1153846
.2692308 .1923077
.2307692 .3076923
.2884615 .3846154
.2500000 .5000000
.3076923 .5769231
.2692308 .6923077
.3269231 .7692308
.2884615 .8846154
.3461538 .9615385
.3076923 .0769231
.3653846 .1538462
.3269231 .2692308
.3846154 .3461538
.3461538 .4615385
.4038462 .5384615
.3653846 .6538462
.4310000 .7330000
.3846154 .8461538
.4490000 .9120000
.4038462 .0384615
.4615385 .1153846
.4310000 .2330000
.5000000 .3140000
.4490000 .4120000
.4615385 .6153846
.5000000 .8140000
.5000000 0.
.5384615 .1153846
.5961538 .0384615
.6346154 .1538462
.5690000 .2330000
.6153846 .3461538
.5510000 .4120000
.5961538 .5384615
.5384615 .6153846
.5690000 .7330000
.5510000 .9120000
.7500000 .0000000
.6923077 .0769231
.7307692 .1923077
.6730769 .2692308
.7115385 .3846154
.6538462 .4615385
.6923077 .5769231
.6346154 .6538462
.6730769 .7692308
.6153846 .8461538

.6538462 .9615385
.8461538 .0384615
.7884615 .1153846
.8269231 .2307692
.7692308 .3076923
.8076923 .4230769
.7500000 .5000000
.7884615 .6153846
.7307692 .6923077
.7692308 .8076923
.7115385 .8846154
.9423077 .0769231
.8846154 .1538462
.9230769 .2692308
.8653846 .3461538
.9038462 .4615385
.8461538 .5384615
.8846154 .6538462
.8269231 .7307692
.8653846 .8461538
.8076923 .9230769
.9615385 .3846154
.9423077 .5769231
.9230769 .7692308
.9615385 .8846154
.9038462 .9615385

Silicon Σ13 Edge Dislocation Model Grain Boundary

A=27.67850Å B=13.83925Å C=5.428200Å
102 Atoms

0. .5000000
.5125 .4675
0. .6923077
.0384615 .8846154
0. .0000000
.0576923 .0769231
0. .1923077
.0769231 .2692308
.0384615 .3846154
.0961538 .4615385
.0576923 .5769231
.1153846 .6538462
.0769231 .7692308
.1346154 .8461538
.0961538 .9615385
.1538462 .0384615
.1153846 .1538462
.1730769 .2307692
.1346154 .3461538
.1923077 .4230769
.1538462 .5384615
.2115385 .6153846
.1730769 .7307692
.2307692 .8076923
.1923077 .9230769
.2500000 .0000000
.2115385 .1153846
.2692308 .1923077

.2307692 .3076923
.2884615 .3846154
.2500000 .5000000
.3076923 .5769231
.2692308 .6923077
.3269231 .7692308
.2884615 .8846154
.3461538 .9615385
.3076923 .0769231
.3653846 .1538462
.3269231 .2692308
.3846154 .3461538
.3461538 .4615385
.4175 .54
.3653846 .6538462
.4230769 .7307692
.3846154 .8461538
.438 .932
.4038462 .0384615
.465 .093
.419 .231
.478 .288
.4423077 .4230769
.4765 .6535
.4695 .865
.4875000 .9675
.5235 .1535
.5305 .365
.5825 .04
.6346154 .1538462
.5769231 .2307692
.6153846 .3461538
.5620000 .4320000
.5961538 .5384615
.535 .593
.581 .731
.522 .788
.5576923 .9230769
.7500000 .0000000
.6923077 .0769231
.7307692 .1923077
.6730769 .2692308
.7115385 .3846154
.6538462 .4615385
.6923077 .5769231
.6346154 .6538462
.6730769 .7692308
.6153846 .8461538
.6538462 .9615385
.8461538 .0384615
.7884615 .1153846
.8269231 .2307692
.7692308 .3076923
.8076923 .4230769
.7500000 .5000000
.7884615 .6153846
.7307692 .6923077
.7692308 .8076923
.7115385 .8846154
.9423077 .0769231
.8846154 .1538462
.9230769 .2692308
.8653846 .3461538
.9038462 .4615385
.8461538 .5384615
.8846154 .6538462
.8269231 .7307692
.8653846 .8461538
.8076923 .9230769
.9615385 .3846154
.9423077 .5769231
.9230769 .7692308
.9615385 .8846154
.9038462 .961538

Silicon Σ13 45° Dislocation/Dipole Model

A=27.67850Å B=13.83925Å C=5.428200Å
102 Atoms

0. .5000000
.500 .535
0. .6923077
.0384615 .8846154
0. .0000000
.0576923 .0769231
0. .1923077
.0769231 .2692308
.0384615 .3846154
.0961538 .4615385
.0576923 .5769231
.1153846 .6538462
.0769231 .7692308
.1346154 .8461538
.0961538 .9615385
.1538462 .0384615
.1153846 .1538462
.1730769 .2307692
.1346154 .3461538
.1923077 .4230769
.1538462 .5384615
.2115385 .6153846
.1730769 .7307692
.2307692 .8076923
.1923077 .9230769
.2500000 .0000000
.2115385 .1153846
.2692308 .1923077
.2307692 .3076923
.2884615 .3846154
.2500000 .5000000
.3076923 .5769231
.2692308 .6923077
.3269231 .7692308
.2884615 .8846154
.3461538 .9615385
.3076923 .0769231
.3653846 .1538462
.3269231 .2692308
.3846154 .3461538
.3461538 .4615385
.4038462 .5384615
.3653846 .6538462
.4310000 .7330000
.3846154 .8461538
.4490000 .9120000
.4038462 .0384615
.4615385 .1153846
.452 .246
.497 .347
.443 .423
.4615385 .6153846
.5000000 .8140000
.5000000 0.
.550 .145
.588 .080
.6346154 .1538462
.562 .293
.625 .321
.537 .455
.5961538 .5384615
.5384615 .6153846
.5690000 .7330000
.559 .949
.7500000 .0000000
.6923077 .0769231
.7307692 .1923077
.6730769 .2692308
.7115385 .3846154
.640 .460
.6923077 .5769231
.6346154 .6538462
.6730769 .7692308
.6153846 .8461538
.6538462 .9615385
.8461538 .0384615
.7884615 .1153846
.8269231 .2307692
.7692308 .3076923
.8076923 .4230769
.7500000 .5000000
.7884615 .6153846
.7307692 .6923077
.7692308 .8076923
.7115385 .8846154
.9423077 .0769231

.8846154 .1538462
.9230769 .2692308
.8653846 .3461538
.9038462 .4615385
.8461538 .5384615
.8846154 .6538462
.8269231 .7307692
.8653846 .8461538
.8076923 .9230769
.9615385 .3846154
.9423077 .5769231
.9230769 .7692308
.9615385 .8846154
.9038462 .9615385

30° Dislocation Glide/Segregation Model
(from 60° split dislocation)

A=26.26800Å B=25.18393Å C=3.838000Å
128 Atoms

.5641332	.4826095	(donor seg. site)	.5207099	.1412834
.0073993	.1342300		.6091634	.5127415
.0050290	.2271068		.6094519	.8879738
.1354493	.1358014		.5190621	.2350483
.1223638	.5074882		.6126134	.6073632
.1099321	.8826133		.6080608	.9813064
.1330199	.2286346		.6492178	.1411955
.1184239	.6010859		.7349205	.5116181
.1080554	.9763174		.7337876	.8877457
.2637471	.1377220		.6478721	.2342905
.2486541	.5090367		.7359718	.6055410
.2347792	.8844767		.7325881	.9814709
.2614624	.2306753		.7781878	.1408197
.2434929	.6028857		.8611480	.5114729
.2330513	.9780035		.8577707	.8877260
.3920903	.1397538		.7771042	.2334277
.3744442	.5114716		.8606227	.6052014
.3596098	.8863785		.8567757	.9817104
.3901837	.2332068		.9074197	.1409008
.3670723	.6060596		.9874501	.5118551
.3580564	.9796102		.9815359	.8882868
.4918089	.5216716		.9063348	.2333319
.4846113	.8876237		.9855976	.6055756
.4898775	.6101574		.9807352	.9823468
.4831374	.9807326		.0893930	.2590163

.0754291	.6318615
.0862953	.3518615
.0723314	.7256829
.2176648	.2608481
.2005489	.6335253
.2142653	.3535253
.1971494	.7275147
.3464716	.2633815
.3246283	.6361672
.3432757	.3561672
.3214324	.7300481
.4752433	.2658986
.4477723	.6401585
.4732215	.3601585
.4457505	.7325653
.5717882	.6397637
.5705019	.7328283
.6044041	.2657489
.6948166	.6373506
.6035392	.3587659
.6943932	.7315108
.7337112	.2645005
.8188862	.6365810
.7332867	.3569539
.8182089	.7307885
.8629226	.2640806
.9434803	.6367253
.8620516	.3565492
.9421624	.7309350
.9920729	.2644940
.9905159	.3569244
.0526867	.0108331
.0426899	.3824129
.0297143	.7564601
.0507652	.1037554
.0392646	.4755582
.0273103	.8502715
.1807243	.0124241
.1702408	.3838296
.1546681	.7581375
.1788873	.1054279
.1659701	.4768404
.1522575	.8519603
.3088267	.0141223
.2986243	.3859320
.2791771	.7603778
.3071611	.1073552
.2928552	.4785849
.2770026	.8539712
.4368950	.0156120
.4288360	.3899612
.4035860	.7628708
.4353819	.1091275
.4207860	.4817654
.4017948	.8558775
.5284766	.7639373
.5268288	.8568389
.5654326	.0167383
.5599720	.3908273
.6527564	.7631794
.5639993	.1101864
.6514107	.8567510
.6938709	.0169861
.6903511	.3881281
.7766141	.7623165
.6926007	.1100523
.6920889	.4807218
.7755305	.8563753
.8226705	.0171529
.8190792	.3874415
.9004733	.7622208
.8216105	.1099006
.8190256	.4803433
.8993884	.8564564
.9517378	.0176358
.9472312	.3876060
.9508691	.1102477
.9458223	.4805642

30° Dislocation Shuffle Model

A=26.26800Å B=25.18393Å C=3.838000Å
127 Atoms

.0080076	.1344143	.9808657	.8880883
.0058360	.2273251	.9055227	.2335716
.1359846	.1359558	.9843269	.6054660
.1241306	.5075294	.9802360	.9821943
.1105434	.8824295	.0903024	.2592720
.1338174	.2288768	.0768552	.6316600
.1200759	.6008979	.0875244	.3521190
.1084680	.9762174	.0734523	.7254161
.2641131	.1377386	.2185114	.2611049
.2513197	.5091297	.2023902	.6331682
.2352152	.8844221	.2156625	.3539019
.2620964	.2308300	.1983395	.7271668
.2457899	.6025055	.3469889	.2633826
.2333160	.9780429	.3268567	.6355384
.3922358	.1395013	.3444878	.3565076
.3797578	.5118242	.3223295	.7298485
.3597858	.8866281	.4753182	.2653438
.3904572	.2329858	.4483271	.6410547
.3702136	.6052099	.4734134	.3593846
.3581605	.9798575	.4458834	.7332547
.4846113	.8880640	.5702587	.6395428
.4898775	.6122969	.5701319	.7331949
.4831374	.9810813	.6040503	.2655631
.5206762	.1408917	.6926644	.6368127
.6038497	.5130940	.6026067	.3588893
.6092759	.8882235	.6933280	.7311976
.5190028	.2345449	.7329388	.2647169
.6094721	.6065135	.8171989	.6362892
.6079568	.9815537	.7318779	.3573633
.6490015	.1410394	.8170227	.7304627
.7322550	.5117111	.8620144	.2643481
.7333516	.8876910	.9421616	.6365549
.6474675	.2342297	.8607576	.3568436
.7336748	.6051608	.9410861	.7306966
.7323234	.9815102	.9911926	.2647162
.7777547	.1408988	.9894150	.3571222
.8593812	.5115142	.0530719	.0109372
.8571595	.8875422	.0439359	.3826156
.7763916	.2336349	.0307012	.7562172
.8589707	.6050133	.0512974	.1039175
.8563632	.9816104	.0406843	.4756390
.9068504	.1410734	.0280446	.8500544
.9861304	.5118782	.1810074	.0124427

.1717648 .3841549
.1556983 .7578350
.1793117 .1055207
.1679048 .4769912
.1529163 .8517647
.3089816 .0139926
.3003505 .3864284
.2800134 .7601595
.3074065 .1072674
.2958336 .4789481
.2774313 .8539590
.4369415 .0153358
.4297120 .3898375
.4038510 .7632631
.4354533 .1088072
.4260671 .4830136
.4019183 .8562479
.5283789 .7645535
.5267806 .8572990
.5653860 .0164621
.5590960 .3907037
.6520818 .7630929
.5639279 .1098660
.5588521 .4838578
.6510880 .8568559
.6937160 .0168564
.6886248 .3886245
.7756085 .7620110
.6923554 .1099645
.6891105 .4810850
.7749294 .8562153
.8223874 .0171716
.8175551 .3877668
.8994602 .7619552
.8211860 .1099934
.8170908 .4804941
.8986658 .8562371
.9513527 .0177400
.9459852 .3878087
.9503369 .1104098
.9444026 .4806448

Silicon Split (27Å) 60° Dislocation Model

A=59.83400Å B=37.60800Å C=3.838000Å
414 Atoms

.0181353 .2292148
.0136855 .4785641
.0093408 .7293035
.0204485 .0424730
.0171565 .2914590
.0124796 .5411384
.0085068 .7920677
.0742299 .2300647
.0692042 .4792200
.0643465 .7301639
.0765505 .0433274
.0731893 .2922591
.0677901 .5418286
.0635001 .7929421
.1304462 .2311171
.1247014 .4800144
.1192437 .7312142
.1326900 .0442631
.1293797 .2932821
.1229718 .5426915
.1184198 .7939626
.1867713 .2324031
.1801453 .4810514
.1740539 .7324621
.1888475 .0452263
.1857683 .2946186
.1778794 .5438967
.1732953 .7950916
.2431164 .2337637
.2353694 .4826819
.2288568 .7337356
.2450081 .0461129
.2422794 .2963438
.2321330 .5460221
.2281749 .7961675
.2868947 .4895122
.2837348 .7345695
.2860468 .5487661
.2830878 .7969191
.2995828 .2347880
.3384155 .4835323
.3385421 .7348039
.3013664 .0470047
.2988594 .2975770
.3399301 .5468950
.3379314 .7973034
.3560001 .2347291
.3936252 .4827800
.3931278 .7346511
.3576288 .0474568
.3554093 .2970696
.3940867 .5456747
.3926012 .7974135
.4126204 .2344775
.4490414 .4826828
.4475587 .7346379
.4139934 .0477983
.4121446 .2964918
.4488108 .5454474
.4471219 .7975739
.4693555 .2345318
.5044904 .4829387
.5018939 .7350134
.4704508 .0481758
.4688792 .2964276
.5036771 .5456979
.5015424 .7980001
.5261745 .2350492
.5599217 .4835293
.5561468 .7358563
.5269579 .0486809
.5256566 .2969015
.5584373 .5463783
.5559158 .7987597
.5830927 .2360872
.6152687 .4845953
.6103593 .7371418
.5834530 .0493015
.5826095 .2979817
.6127722 .5477267
.6103194 .7997668
.6400564 .2375966
.6702490 .4867191
.6646852 .7385173
.6398707 .0498978
.6398191 .2998322
.6659518 .5507402
.6648629 .8006800
.6968537 .2390197
.7176523 .4996595
.7192406 .7390283
.6961737 .0502165
.6970310 .3021014
.7180755 .5556013
.7195658 .8009089
.7537832 .2385917

.7656302	.4877315
.7741494	.7384031
.7526748	.0497181
.7543398	.3017035
.7714288	.5521766
.7745567	.8003958
.8104877	.2366346
.8201831	.4843446
.8286497	.7366410
.8089032	.0487869
.8114693	.2989387
.8240524	.5476471
.8292554	.7990630
.8672802	.2345417
.8754787	.4825796
.8830490	.7346621
.8651936	.0475473
.8685225	.2965473
.8781965	.5454524
.8838561	.7974083
.9239349	.2328323
.9309137	.4813504
.9375391	.7329786
.9215165	.0462432
.9252230	.2948415
.9330007	.5440615
.9384636	.7958487
.9803841	.2315051
.9863991	.4803969
.9922014	.7316410
.9778224	.0450217
.9816156	.2935914
.9880964	.5430324
.9931615	.7945212
.0015416	.0629661
.0008368	.1252238
.0576312	.0637929
.0541244	.3127138
.0489350	.5624765
.0449217	.8135543
.0569301	.1260543
.0529169	.3749765
.0477275	.6252138
.0442206	.8762929
.1137689	.0647192
.1102267	.3136270
.1040962	.5633002
.0998708	.8145172
.1130922	.1270172
.1088667	.3758002
.1027363	.6261270
.0991940	.8772192
.1699354	.0657082
.1665403	.3148536
.1590262	.5644143
.1547722	.8155908
.1693018	.1280908
.1650479	.3769143
.1575337	.6273536
.1541387	.8782082
.2261077	.0666648
.2230889	.3165501
.2134993	.5661834
.2096654	.8166635
.2255198	.1291635
.2216859	.3786834
.2120962	.6290501
.2090775	.8791648
.2822845	.0674499
.2796221	.3182357
.2675618	.5688561
.2645691	.8175176
.2817272	.1300176
.2787345	.3813561
.2666742	.6307357
.2640118	.8799499
.3220071	.5685917
.3194773	.8180389
.3214424	.6309118
.3189412	.8805139
.3387061	.0681539
.3363261	.3181354
.3760188	.5669759
.3742214	.8182673
.3381842	.1306398
.3359464	.3804236
.3758329	.6300296
.3737400	.8808802
.3950566	.0684797
.3930943	.3172994
.4304877	.5664605
.4288174	.8184372
.3946014	.1308163
.3929079	.3792103
.4301903	.6295459
.4284243	.8811854

.4515180	.0688031
.4498205	.3170182
.4851868	.5665571
.4833006	.8187856
.4511597	.1310255
.4494381	.3789392
.4846082	.6296440
.4830186	.8815882
.5080539	.0692599
.5065198	.3172951
.5398459	.5671137
.5377257	.8194176
.5078134	.1314634
.5058363	.3791904
.5389500	.6302853
.5375761	.8821604
.5646050	.0698839
.5633551	.3181366
.5941863	.5682734
.5921628	.8202962
.5645046	.1321898
.5623581	.3799167
.5930324	.6316017
.5921655	.8828503
.6210999	.0705764
.6205050	.3197401
.6477473	.5706526
.6467073	.8211835
.6211540	.1331101
.6193249	.3813767
.6467611	.6338530
.6468554	.8834593
.6774782	.0710910
.6779464	.3222698
.7004593	.5749773
.7014195	.8216112
.6776661	.1339038
.6772496	.3844421
.7005783	.6362517
.7016704	.8836762
.7340331	.0708807
.7355528	.3235193
.7545042	.5747590
.7564083	.8213277
.7343325	.1338277
.7362365	.3872590
.7551880	.6360193
.7567077	.8833807
.7902700	.0700632
.7927903	.3206457
.8072540	.5699895
.8111871	.8203211
.7906648	.1328211
.7945978	.3824895
.8090615	.6331457
.8115819	.8825632
.8465742	.0688251
.8500517	.3178861
.8608975	.5671389
.8658658	.8188194
.8470972	.1313194
.8520654	.3796389
.8629113	.6303861
.8663888	.8813251
.9029261	.0674620
.9068754	.3159954
.9153822	.5654555
.9205047	.8172668
.9035693	.1297668
.9086919	.3779555
.9171987	.6284954
.9211480	.8799620
.9592690	.0661691
.9633203	.3146589
.9702835	.5642778
.9751925	.8158825
.9599927	.1283825
.9649017	.3767778
.9718649	.6271589
.9759162	.8786691
.0379681	.1465101
.0338886	.3955210
.0289951	.6458734
.0256708	.8969140
.0371271	.2087386
.0326215	.4579375
.0279939	.7086459
.0250762	.9596208
.0941119	.1474328
.0897231	.3962587
.0840266	.6467367
.0806656	.8977986
.0932684	.2096576
.0882194	.4586328
.0829712	.7095568
.0800934	.9604708

.1503228	.1484983
.1457203	.3972073
.1388837	.6478599
.1356288	.8987520
.1495163	.2107776
.1438454	.4594914
.1378253	.7106877
.1350887	.9613625
.2065621	.1496354
.2020831	.3986152
.1935454	.6493602
.1905807	.8997032
.2058309	.2120682
.1995503	.4606596
.1925907	.7120343
.1900743	.9622368
.2627865	.1506330
.2592484	.4013133
.2481632	.6510296
.2455291	.9005368
.2621222	.2132550
.2557143	.4627894
.2473768	.7133109
.2450508	.9630145
.3029925	.6517437
.3004854	.9011713
.3022691	.7139546
.3000304	.9636500
.3192169	.1513872
.3168196	.4018933
.3575536	.6512362
.3553341	.9016235
.3185876	.2139641
.3186464	.4633546
.3569628	.7138958
.3549225	.9641582
.3756036	.1515532
.3740584	.4000858
.4119295	.6506584
.4100807	.9019650
.3750460	.2138743
.3748213	.4620904
.4114537	.7136442
.4097401	.9645759
.4321491	.1516649
.4305724	.3996260
.4663060	.6505943
.4647344	.9023424
.4316837	.2137727
.4305489	.4618371
.4658297	.7136985
.4644915	.9649929
.4888120	.1519883
.4868335	.3997362
.5206397	.6510682
.5193384	.9028476
.4884306	.2140052
.4862150	.4619849
.5201218	.7142159
.5192119	.9654633
.5455406	.1526375
.5431223	.4002632
.5747979	.6521484
.5739544	.9034681
.5452625	.2146884
.5418839	.4624573
.5743147	.7152539
.5739510	.9659656
.6022696	.1535847
.5997050	.4013359
.6286994	.6539989
.6286479	.9040645
.6021584	.2158413
.5976076	.4633349
.6284621	.7167633
.6287558	.9663892
.6588952	.1545870
.6571302	.4035820
.6825986	.6562681
.6834559	.9043832
.6590046	.2172634
.6535415	.4649710
.6827759	.7181864
.6836466	.9665602
.7153370	.1551100
.7161160	.4087455
.7372633	.6567930
.7385125	.9042136
.7156210	.2181897
.7114459	.4698537
.7376235	.7183576
.7387439	.9663523
.7720111	.1541912
.7760626	.4044022
.7914620	.6550045
.7934035	.9036253

.7724764	.2170674
.7812163	.4653940
.7921556	.7171920
.7936933	.9658306
.8284638	.1526867
.8339410	.4009371
.8454057	.6522240
.8482656	.9025612
.8291426	.2151326
.8373392	.4628323
.8465033	.7150753
.8486317	.9649305
.8849846	.1510332
.8906200	.3990982
.8995745	.6500800
.9030703	.9012769
.8858414	.2132270
.8930886	.4612953
.9008503	.7130910
.9035251	.9638174
.9414643	.1495458
.9468051	.3978555
.9540982	.6485514
.9578590	.8999893
.9424082	.2116640
.9487430	.4601755
.9553742	.7115191
.9583943	.9626536
.9978390	.1482978
.9987983	.2104261

References

(1) J. H. Rose and R. Gronsky, *Appl. Phys. Lett.*, **41**, 993 (1982).

(2) V. Volterra, *Ann. Ecole Norm. Super.*, **24**, 400 (1907).

(3) M. P. Puls in *Dislocation Modeling of Physical Systems*, M. F. Ashby, R. Bullough, C. S. Hartley, and J. P. Hirth Eds., Pergamon, New York, 1981.

(4) M.L. Cohen in *Surfaces and Interfaces in Ceramic and Ceramic-Metal Systems*, Materials Science Research Vol. 14, Ed. J. Pask and A. Evans, Plenum Press, New York, 1981, pgs. 1-12.

(5) R.E. Thomson and D.J. Chadi, *Phys. Rev.*, **29**, 889 (1984).

(6) S. Marklund, *Phys. Stat. Sol.*, **85**, 673 (1978).

(7) J. Hornstra, *J. Phys. Chem. Solids*, **5**, 129 (1958).

(8) John Price Hirth and Jens Lothe, *Theory of Dislocations* (2^{nd} Edition), John Wiley and Sons, New York, 1982, pg.376.

(9) M.H. Brodsky, S Kirkpatrick, and D. Waire in *Tetrahedrally Bonded Amorphous Semiconductors*, A.I.P. Conf. Proceedings No. 20 (1974).

(10) W. Shockley, *Phys. Rev.*, **91**, 228 (1953).

(11) K. Wessel and H. Alexander, *Phil. Mag.*, **35**, 1523 (1977).

(12) J. M. Burgers, *Proc. Phys. Soc.*, **23**, 23 (1940).

(13) G. Friedel, *Lecons de Cristallographie*, Berger Levrault, Paris, 1926.

(14) H. Mykura in *Grain-Boundary Structure and Kinetics*, 1979 ASM Materials Science Seminar, American Society for Metals, Metals Park, Ohio, 1980, pg.445.

(15) W. Bollmann, *Crystal Defects and Crystalline Interfaces*, Springer Verlag, New York, 1970.

(16) W. T. Read and W. Shockley, *Phys. Rev.*, **78**, 275 (1950).

(17) R.C. Pond and W. Bollmann, *Phil. Trans. R. Soc.* A., **292**, 449.

(18) A.V. Shubnikov, and V.A. Koptsik, *Symmetry in Science and Art*, Plenum Press, New York, 1979.

(19) D. Gratias, R. Portier, M. Fayard, and M. Guymont, *Acta. crystallogr.* A, **35** 885 (1979).

(20) V. Vitek, A.P. Sutton, D.A. Smith, and R.C. Pond in ref. 14, pg. 115.

(21) V. Vitek, A. P. Sutton, Gui Jin Wang, and D.Schwartz, *Scripta Met.*, **17**, 183 (1983).

(22) A. Bourret and J. Desseaux, *Phil. Mag.*, **39**, 405 (1979).

(23) H. Foll and D. Ast, *Phil. Mag.*, **40**, 589 (1979).

(24) C. B. Carter, J .H. Rose, and D. Ast, *Inst. Phys. Conf. Ser.*, **60**, 153 (1981).

(25) R. Schindler, J. H. Rose, and D. Ast, *J. of Metals*, **31**, F-42 (1979).

(26) J.-J. Bacmann, G. Silvestre, M. Petit, and W. Bollmann, *Phil. Mag.* A, **43**, 189 (1981).

(27) J.-J. Bacmann, J.P. Millier, M. Petit, G. Silvestre, *Mater. Res. Bull.*, **15**, 261 (1980).

(28) W. Bollmann, G. Silvestre, and J.-J. Bacmann, *Phil. Mag.* A, **43**, 201 (1981).

(29) J. A. Kohn, *Am. Mineral.*, **43**, 263 (1958).

(30) J. Hornstra, *Physica*, **25**, 409 (1959).

(31) J. Hornstra, *Physica*, **26**, 198 (1960).

(32) J. A. Kohn, *Am. Mineral.*, **41**, 778 (1956).

(33) A. Bourret, J. Desseaux, and A. Renault, *Phil. Mag.*, **45**, 1 (1982).

(34) M. D. Vaudin, B. Cunningham, and D. G. Ast, *Scripta Met.*, **17**, 191 (1983).

(35) Anne-Marie Papon, Maurice Petit, and Jean-Jacques Bacmann, *Phil. Mag.*, **49**, 573 (1984).

(36) C. Fontaine and D. A. Smith, *Appl. Phys. Lett.*, **40**, 153 (1982).

(37) J.-J. Bacmann, A. M. Papon, and M. Petit, *J. Phys., Paris,* **43**, C1-15 (1982).

(38) J. Budai, W. Gaudig, and S. Sass, *Phil. Mag.*, **40A**, 757 (1979).

(39) R. W. Balluffi in *Interfacial Segregation*, W.C. Johnson and J.M. Blakely (eds.), ASM Seminar on Interfacial Segregation, Chicago, 1977.

(40) P.R Howell, D.E. Fleet, A. Hildon, and B. Ralph, *J. Micros.*, **107**, 155 (1976).

(41) W.E. Spear and P.G. LeComber, *Phil. Mag.*, **33**, 935 (1976).

(42) N.F. Mott, *Phil. Mag.*, **19**, 835 (1969).

(43) T.I. Kamins, *J. Electrochem. Soc.*, **127**, 636 (1980).

(44) M.M. Mandurah, K.C. Saraswat, C.R. Helms, and T.I. Kamins, *J. Appl. Phys.*, **51**, 5755 (1980).

(45) B. Swaminathan, E. Demoulin, T.W. Sigmon, R.W. Dutton, and R.J. Reif, *J. Electrochem. Soc.*, **127**, 2227 (1980).

(46) Materials Research Society, vol. 2, 309.

(47) J.M. Cowley and A.F. Moodie, *Acta Cryst.*, **10**, 609 (1957).

(48) J.M. Cowley and A.F. Moodie, *Acta Cryst.*, **12**, 353 (1959).

(49) J.M. Cowley, *Diffraction Physics*, North-Holland, Amsterdam, 1975.

(50) J.G. Allpress, E.A. Hewat, A.F. Moodie, and J.V. Sanders, *Acta Cryst.*, **A28**, 528 (1972).

(51) M.A. O'Keefe and J.V. Sanders, *Acta Cryst.*, **A31**, 307 (1975).

(52) P.G. Self, M.A. O'Keefe, P.R. Buseck, and A.E.C. Spargo, *Ultramicroscopy*, **11**, 35 (1983).

(53) M.A. O'Keefe in *Electron Optical Systems*, SEM Inc., AMF O'Hare (Chicago), 1985, pg.209.

(54) J. Frank, *Optik*, **38**, 519 (1973).

(55) P. Fejes, *Acta Cryst.*, **A33**, 109 (1977).

(56) M.A. O'Keefe and P.R. Buseck, *Trans. A. C. A.*, **15**, 27 (1979).

(57) P.L. Fejes, Ph.D Thesis, Arizona State University (1973).

(58) M.A. O'Keefe, Ph.D. Thesis, University of Melbourne, Australia (1975).

(59) A.J. Skarnulis, Ph.D. Thesis, Arizona State University (1976).

(60) S. Iijima, *Optik*, **48**, 193 (1977).

(61) R.W. Glaisheer and A.E.C. Spargo, *Inst. Phys. Conf. Ser. No. 68*, 185 (1983).

(62) O. Scherzer, *J. Appl. Phys.*, **20** 20 (1949).

(63) *opcit.*

(64) H. Formanek, M. Muller, M.H. Hahn, and T. Koller, *Naturwissenschaften*, **58** 339 (1971).

(65) J.C.H. Spence, in *Electron Microscopy and Analysis* (ed. J.A. Venables) pg. 257 (1975).

(66) John C. H. Spence, *Experimental High-Resolution Electron Microscopy*, Clarendon Press, Oxford, pg. 199 (1981).

(67) L.A. Bursill and Shen Guang Jun, *Optik*, **66**, 251 (1984).

(68) *opcit.*

(69) A. Olsen and J.C.H. Spence, *Phil. Mag.*, **43**, 945 (1981).

(70) *opcit.*

(71) Hisamitsu Endo, Hatsujiro Hashimoto, and Yoshizo Takai, *Trans. Japan Inst. Metals*, **24**, 307 (1983).

(72) O.L. Krivanek, S. Isoda, and K. Kobayashi, *Phil. Mag.*, **36**, 331 (1979).

(73) H. Ichinose and Y. Ishida, *Phil. Mag.*, **43**, 1253 (1981).

(74) J.M. Penisson, R. Gronsky, and J.B. Brosse, *Scripta Met.*, **16** 1239 (1982).

(75) C. d'Anterroches and A. Bourret, *Phil. Mag*, **49**, 783 (1984).

(76) R. Kilaas and R. Gronsky, *Ultramicros.*, **16**, 193 (1985).

(77) T. Schober and R.W. Balluffi, *Phys. Stat. Sol.* (b), **44**, 103 (1971).

(78) F. Cosandey and C.L. Bauer, *Phil. Mag.*, **44**, 391 (1981).

(79) D.A. Smith, V. Vitek, and R.C. Pond, *Acta met.*, **25**, 475 (1977).

(80) C.M. d'Anterroches, Ph.D. Thesis, Grenoble, 1982.

(81) G. Dhalenne, M. Dechamps, and A. Revcolevschi, *MRS Symposia Proceedings* Vol. 5, 1981, pg. 13.

(82) James E. Huheey, *Inorganic Chemistry: Principles of Structure and Reactivity,* 2nd Edition, Harper and Row, New York, 1978, pg. 193.

(83) H. Alexander, *J. Physique Colloq.*, **40**, C6-1 (1979).

(84) E.R. Weber and H. Alexander, *J. Physique Colloq.*, **40**, C6-101 (1979).

(85) E.R. Weber and H. Alexander, *J. Physique Colloq.*, **44**, C4-319 (1983).

(86) R.C. Pond, *J. Micros.*, **116**, 105 (1979).

(87) R.C. Ecob and W.M. Stobbs, *J. Micros.*, **129**, 275 (1983).

This report was done with support from the Department of Energy. Any conclusions or opinions expressed in this report represent solely those of the author(s) and not necessarily those of The Regents of the University of California, the Lawrence Berkeley Laboratory or the Department of Energy.

Reference to a company or product name does not imply approval or recommendation of the product by the University of California or the U.S. Department of Energy to the exclusion of others that may be suitable.

LAWRENCE BERKELEY LABORATORY
TECHNICAL INFORMATION DEPARTMENT
UNIVERSITY OF CALIFORNIA
BERKELEY, CALIFORNIA 94720